Design and Development of High-Temperature Latent Heat Thermal Energy Storage for Power Generation

THESIS

Submitted in partial fulfilment of the requirements for the degree of

DOCTOR OF PHILOSOPHY

by

VIVEK TIWARI

Under the supervision of

Prof. SRINIVASAN PERIASWAMY

and co-supervision of

Dr. AAKASH CHAND RAI

BITS Pilani

Pilani | Dubai | Goa | Hyderabad | Mumbai

BIRLA INSTITUTE OF TECHNOLOGY & SCIENCE

PILANI – 333031 (RAJASTHAN) INDIA

2023

Dedicated to my father and my beloved family

Birla Institute of Technology & Science, Pilani
Pilani Campus

CERTIFICATE

This is to certify that the thesis entitled **"Design and Development of High-Temperature Latent Heat Thermal Energy Storage for Power Generation"** submitted by **Vivek Tiwari** ID No **2016PHXF0414P** for the award of Ph.D. of the Institute embodies original work done by him under my supervision.

Signature (Supervisor):_____

Prof. Srinivasan Periaswamy

Professor, Department of Mechanical Engineering,

BITS Pilani, Pilani Campus

Date: 30/12/2022

Signature (Co-supervisor):_____

Dr. Aakash Chand Rai

Assistant Professor, Department of Sustainable Energy Engineering,

IIT Kanpur

Date: 30/12/2022

Acknowledgment

Undertaking this Ph.D. has been a life-changing experience for me and would not have been possible without the support and guidance I received from many people. First and foremost, I thank almighty God for showering his divine blessings and giving me inner strength and patience during this journey.

I pay obeisance unto the lotus feet of my supervisors, **Prof. Srinivasan Periaswamy** and **Dr. Aakash Chand Rai,** for their valuable guidance, excellent direction, everlasting encouragement, and inspiration given to me, without which the present work would not have been possible. I feel indebted to him for teaching me every aspect of the art of doing research and other important aspects of life. Without their trust and constant support, the achievement of this work would have remained a dream.

I am grateful to **Prof. Souvik Bhattacharyya,** Vice-Chancellor, and **Prof. Sudhir Kumar Barai,** Director, BITS Pilani, Pilani Campus, for giving me the opportunity to pursue my research work at the institute. I sincerely thank **Prof. M. B. Srinivas**, Dean, Academic – Graduate Studies & Research (AGSR), and **Prof. Shamik Chakraborty**, Associate Dean, AGSR, for their official support and encouragement.

I am highly indebted to my Doctoral Advisory Committee (DAC) members, **Prof. M. S. Dasgupta,** Professor, Department of Mechanical Engineering, Pilani Campus, and **Dr. Shyam Sunder Yadav,** Assistant Professor, Department of Mechanical Engineering, Pilani Campus, for their insightful comments and encouragement. I would also like to acknowledge **Prof. Arun Kumar Jalan**, Convener, Departmental Research Committee, Associate Professor, Mechanical Engineering Department, Pilani Campus, who has provided valuable comments during the departmental seminars.

I want to express my gratitude and thanks to **Prof. Bijay K. Rout, Prof. Rajesh P. Mishra, Prof. Manoj Soni, Prof. Sharad Srivastava, Prof. Jitendra S. Rathore, Dr. Amol Marathe, Dr. Sachin U. Belgamwar, Dr. Murali Palla Dr. Aneesh A. M., Dr. A. R. Harikrishnan and Dr. Saket Verma** for their valuable suggestion and help, without which, the dream of developing the experimental set-up would not have come true.

I thank **Prof. Srikanta Routroy** (Head of Department) and the entire faculty and staff of the Department of Mechanical Engineering, BITS-Pilani, Pilani Campus, for their kind, moral support, and assistance.

My gratitude knows no bounds to **Dr. Kiran Raj K and Mrs. Sethulakshmi** for their unstinting guidance, many valuable suggestions, and kind help at various stages of the work. I also wish to thank their daughter **Ms. Lakshya Kiran** for her love and affection. I cherish all the moments spent with my friends and highly talented research scholars, **Dr. Shreekant Varshney, Mr. Siddhartha D, Mr. Chetan Jalendra, Mr. Ashish Kumar Srivastava, Mr. Amresh Kumar, and Dr. Neha Choudhary**. I have learned a lot from everyone. I thank them for always being there for me and making my time memorable in BITS Pilani. I wish them a very bright future.

I would also like to thank the graduate student, **Mr. Shyam Sunder P.I.**, who helped me set up the simulation. I also thank the non-teaching staff, **Mr. Dhanna Ram Saini, Mr. Niranjan Saini, Mr. Harish Saini, and Late. Mr. Parvat Ram** for their valuable help at each stage of the experimental work. My sincere thanks to all those I miss to acknowledge, who had directly or indirectly helped me accomplish this task.

Last but not least, I would like to thank my family, my father, **Mr. R. S. Tiwari,** and my mother, **Mrs. Sudha Tiwari**. I also thank my brother **Mr. Vinay Tiwari** and sister-in-law, **Mrs. Suman Gautam**. I am deeply indebted to all the pains taken by them to make my dream come true. Thank you for giving me the confidence and courage to make my choices. I would also thank my uncles and aunts. Their constant love and care empowered me to accomplish my thesis and also ignited me to take on more challenges in my life.

Vivek Tiwari
Dec 2022

Abstract

Increased demands for renewable energy have been catalyzed by climate change. However, the majority of renewable energy sources are not demand-driven which hampers their ability to replace fossil fuel-based power generation. In order to increase the share of renewable energy in the global energy mix, an affordable energy storage solution is the need of the hour. Concentrated solar power, combined with inexpensive thermal energy storage, is an attractive renewable technology due to its low levelized cost of electricity and high annual capacity factor. As a result, these plants are extensively researched for their potential role in replacing conventional power plants.

High-temperature latent heat thermal energy storage (LHTES) systems are currently being considered for integration into the next-generation high-efficiency CSP plants due to their high energy density, low storage cost, and energy delivery at isothermal temperatures. However, the challenging task is to properly design the LHTES system under real-world operating conditions and select compatible structural materials. Thus, the present work has conducted numerical and material investigations to develop the LHTES system. In the numerical investigation, parametrical analysis and multi-objective design optimization are conducted using realistic operating conditions, whereas, in the material investigation, a compatibility test is performed to find suitable structural materials and corrosion-protective ceramic coatings.

The numerical investigation has been done to study the effects of the LHTES system's design parameters (length L, shell radius R, tube radius r_o, and heat transfer fluid's velocity u_m) on its performance under periodic steady-state conditions with charging and discharging 'cutoff' temperatures to mimic its real-world operation. The term "periodic steady-state" refers to a state in which the charging and discharging process of the LHTES system reaches a stable and repetitive pattern over time. In other words, it describes a condition where the thermal state of the system on the n^{th} day is equal to the thermal state of the previous $(n-1)^{th}$ day. The results show that with the incorporation of cutoff temperatures, the system's specific energy and storage effectiveness decreased by 74% and 68%, respectively, due to lower useful

charging and discharging times. Furthermore, the study demonstrates that the system's useful charging and discharging time could be augmented by increasing the R or L of the system, or by decreasing the system's r_o or u_m that flows through the system. The system's geometrical parameters (R, L, and r_o) and u_m also substantially influenced its performance, but in a different manner than their influence on charging-discharging times. For example, increasing R deteriorated the system's performance substantially.

After the parametric analysis, a multi-objective optimization is carried out for two use-case scenarios, i.e., for the TES systems integrated with hybrid PV-CSP and baseload CSP plants. The result shows that the optimized design of the TES system combined with the peak load CSP plant has t_d, SE, and Q of 12.3 h, 33%, and 3034 MWh, respectively. Similarly, the optimized design for the TES system integrated with a hybrid PV-CSP plant has t_d, SE, and Q of 11.8 h, 33%, and 3053.1 MWh, respectively. Compared to the initial design, optimized LHTES design performance improved by 1% and 12.66% for hybrid PV-CSP and baseload CSP plants, respectively. Thus, the optimized LHTES design configurations accomplished their respective objectives required for hybrid PV-CSP and baseload CSP plants.

The LHTES integrated with the CSP plant used the Aluminum Silicon eutectic (AlSi12) alloy as a promising phase change material to generate dispatchable power at an affordable cost. Despite AlSi12's favorable thermophysical properties, it is found to react with steel at higher temperatures, posing a challenge for LHTES's structure. As a solution to this problem, ceramic materials can be used as a protective coating over steel due to their corrosion-resistant properties. Thus, this study examines the compatibility of steel structural materials (SS316, SS202, and P91) and suitable ceramic-coated over steel (alumina – Al_2O_3 and yttria-stabilized zirconia – YSZ) with molten AlSi12. The results indicate that P91 steel and YSZ-coated steel have better corrosion resistance when measured over 120 hours.

Numerical and material investigations in the thesis contribute to the advancement of latent heat storage technology for concentrating solar power. The study provides a better understanding of the parametric analysis and design optimization of the LHTES system for both CSP plant configurations. The

study also suggested that compatible structural material and its ceramic coating enhance the corrosion resistance property. As a whole, this thesis provides inspiration for future work that will bring the LHTES systems to the commercial production level for CSP plants, which could contribute to significant growth in the production of clean electricity around the globe.

Table of contents

	Page no
CERTIFICATE	*i*
Acknowledgment	*ii*
Abstract	*iv*
Table of contents	*vii*
List of tables	*x*
List of figures	*xi*
Nomenclature	*xiv*
List of abbreviations	*xvi*
Chapter 1: Introduction	*1*
1.1 Motivation	*1*
1.2 Objectives of the thesis	*4*
1.3 Organization of the thesis	*4*
Chapter 2: Literature review and research gaps	*6*
2.1 Literature review on latent heat thermal energy storage (LHTES) systems	*6*
2.1.1 PCM material selection	*7*
2.1.2 Geometrical design	*8*
2.1.3 HTF's velocity and boundary conditions	*9*
2.1.4 Compatibility issue between PCM and steel structural materials	*11*
2.2 Research gap	*12*
Chapter 3: Mathematical model and design optimization of the TES system	*14*
3.1 Thermal energy storage system description	*14*
3.2 Mathematical formulation	*16*
3.2.1 Governing equations for the PCM	*16*
3.2.2 Governing equations for the tube and HTF	*18*
3.2.3 LHTES system operation and boundary conditions	*19*
3.2.4 Model validation	*21*
3.2.5 Performance metrics	*23*
3.2.6 Grid and time independence tests	*23*

3.2.7 Effect of operational strategy (realistic boundary conditions) 25
3.3 Design optimization procedure using RSM. 29
3.4 Summary 31

Chapter 4: Parametric analysis of a latent heat thermal energy storage for a CSP plant under realistic operating conditions 33
4.1 System description and methodology 33
4.2 Results and discussion 34
4.2.1 Effect of HTF's velocity (***um***) 34
4.2.2 Effect of shell radius (***R***) 36
4.2.3 Effect of tube radius (r_o) 38
4.2.4 Effect of length (***L***) 39
4.2.5 Design optimization 41
4.3 Summary 42

Chapter 5: A multi-objective design optimization of a latent heat thermal energy storage (LHTES) system for CSP plants under realistic operating conditions 43
5.1 System description 43
5.2 Methodology 45
5.2.1 An iterative method to find $\dot{m}$ 46
5.2.2 Design optimization 48
5.3 Results and Discussion 51
5.3.1 Hybrid PV-CSP plant 51
5.3.2 Baseload CSP plant 54
5.4 Summary 57

Chapter 6: Compatibility of structural materials with AlSi12 alloys-based phase change material and enhance the corrosion resistance property by ceramic coatings 58
6.1 Experimental description 58
6.1.1 Materials 58
6.1.1.1 Synthesis of AlSi12 alloy (PCM) 58
6.1.1.2 Steels and ceramic-coated steels structural materials coupons 60
6.1.2 Corrosion test 61
6.2 Results and discussion 62
6.2.1 Microstructure and crystalline phase observation of AlSi12 (PCM) 62
6.2.2 Interaction of steel structural materials with AlSi12 alloy 64

6.2.3 Corrosion test analysis between coated steel structural materials and AlSi12 (PCM) *64*
6.3 Summary *67*

Chapter 7: Conclusion and future scope of the work *68*
7.1 Parametric analysis *68*
7.2 Multi-objective design optimization *69*
7.3 Compatibility between AlSi12 and structural materials *70*
7.4 Future scope of work *72*

Appendix A: Design optimization *74*
Appendix B: Preliminary design using an analytical solution ‘e-NTU’ *79*

References *82*

List of publications and awards *92*
List of conferences and courses attended *93*
Brief biography of supervisors and candidate *94*

List of tables

S No.	Title of the Tables	Page No.
Table 2.1	Literature on shell-and-tube-based LHTES system	*10*
Table 3.1	Thermophysical properties of the PCM and HTF	*15*
Table 3.2	The thermal boundary conditions	*20*
Table 3.3	Investigated grid sizes	*24*
Table 4.1	The top five design choices were obtained using the response surface methodology (RSM)	*42*
Table 5.1	Example to find the mass flow rate of HTF in a unit cell	*48*
Table 5.2	The performance of the optimized design for the peak load plant (obtained using response RSM) compared with the baseline design	*53*
Table 5.3	Effect of length on optimized LHTES system's for the peak load power plant model	*54*
Table 5.4	The performance of the optimized design of LHTES for baseload CSP plant obtained using response surface methodology (RSM) compared with the baseline design	*56*
Table 5.5	Performance of optimized design of LHTES for baseload CSP plants with discharging time of 6 to 9 h	*57*
Table A- 1	The design variables for the first design cycle	*75*
Table A- 2	The design variables for the second design cycle	*76*
Table A- 3	The design variables for the third design cycle	*76*
Table B- 1	Iterative CFD simulations for confirming the preliminary design	*80*

List of figures

S No.	Title of the figures	Page No.
Fig. 1.1	Global weighted average LCOE and capacity factors for CSP and PV between the year 2010-2021 [2]	*1*
Fig. 1.2	Impact of increasing penetration of solar energy on California state's electrical load [3]	*2*
Fig. 2.1	Developing an LHTES system: an overview [128]	*6*
Fig. 2.2	Classification of PCMs	*7*
Fig. 3.1	Schematic of a thermal energy storage system integrated into a 167 MWe concentrated solar power plant.	*15*
Fig. 3.2	a) The complete LHTES system, b) a unit cell of the LHTES system, and c) the 2D axisymmetric geometry used for the CFD modeling of the LHTES system.	*16*
Fig. 3.3	Validation of CFD model using experimental results by Longeon et al. a) experimental setup and b) comparative graph between temperature profile from CFD model with corresponding thermocouples placed at three different locations reported by Longeon et al. [66]	*22*
Fig. 3.4	CFD results of energy stored and dispatched from the LHTES system, as obtained with a) different grid sizes and b) different time-steps	*25*
Fig. 3.5	Effect of cut-off temperatures on the temporal variation of the a) average HTF temperature and b) average PCM liquid-fraction under periodic steady-state conditions	*26*
Fig. 3.6	Effect of initial condition on the temporal variation of the a) average HTF temperature and b) average PCM liquid-fraction	*28*
Fig. 3.7	Steps for response surface methodology	*30*
Fig. 4.1	The design parameters investigated for the LHTES system	*33*
Fig. 4.2	Effect of HTF's velocity on the temporal variation of the a) average HTF temperature and b) average PCM liquid-fraction	*35*
Fig. 4.3	Effect of HTF's velocity on the LHTES system's performance	*35*
Fig. 4.4	Effect of shell radius on the temporal variation of the a) average HTF temperature and b) average PCM liquid-fraction	*37*

Fig. 4.5	Effect of shell radius on the LHTES system's performance	*37*
Fig. 4.6	Effect of tube radius on the temporal variation of the a) average HTF temperature and b) average PCM liquid-fraction	*38*
Fig. 4.7	Effect of tube radius on the LHTES system's performance	*39*
Fig. 4.8	Effect of length on the temporal variation of the a) average HTF temperature and b) average PCM liquid-fraction	*40*
Fig. 4.9	Effect of length on the LHTES system's performance	*40*
Fig. 5.1	Thermal energy storage integrated into a 167 MWe concentrated solar power plant a) baseload CSP plant (inside the dotted box) and b) Hybrid CSP-PV plant (inside the solid box)	*44*
Fig. 5.2	Flow chart to find a unit cell's mass flow rate ($\dot{m}$)	*48*
Fig. 5.3	Schematic of the central composite design (CCD) used to build the model	*49*
Fig. 5.4	RSM prediction model diagnosis for hybrid CSP-PV plant	*52*
Fig. 5.5	(a) The 2-dimensional contour and (b) the 3-dimensional response surface plots showing the effects of tube radius (ro) and shell radius (R) on the LHTES system's desirability ($\bar{D}$)	*53*
Fig. 5.6	(a) The 2-dimensional contour and (b) the 3-dimensional response surface plots showing the effects of tube radius (ro) and shell radius (R) on the LHTES system's desirability ($\bar{D}$)	*54*
Fig. 5.7	a) The contour plot, and b) The response surface plot of shell radius (R) and tube radius (ro) with its effects on the response output ($\bar{D}$)	*55*
Fig. 6.2	Maximum composition of chromium (Cr) and nickel (Ni) in the structural materials (ASME specification, in wt.%) [32]	*60*
Fig. 6.3	Experimental facility a) front view, b) side view of the high-temperature vacuum furnace, and c) vacuum system	*61*
Fig. 6.1	Corrosion test (upper) and Thermal cycle (lower)	*59*
Fig. 6.4	Microstructure of synthesized AlSi12 alloy	*63*
Fig. 6.5	X-ray diffraction (XRD) spectra of synthesized AlSi12 alloy	*63*
Fig. 6.6	SEM micrograph and EDX mapping of interface between SS316, SS202, and P91 with molten AlSi12 after 120 hours of isothermal (900 °C) corrosion test	*65*

Fig. 6.7	SEM micrograph and EDX mapping of interface between SS316, SS202, and P91 with molten AlSi12 after 120 hours of isothermal (900 °C) corrosion test	*66*
Fig. A- 1	Response (D) obtained from CFD simulations conducted along the path of steepest ascent in the first design cycle	*74*
Fig. A- 2	Response (D) obtained from CFD simulations conducted along the canonical path in the second design cycle	*75*
Fig. A- 3	Actual and model-predicted value of D	*77*
Fig. A- 4	Response (D) obtained from CFD simulations conducted along the canonical path in the third design cycle	*78*
Fig. A- 5	The temporal variation of the a) average HTF temperature and b) average PCM liquid-fraction in the previous best design and design choice # 1 obtained from the response surface methodology	*78*
Fig. B- 1	Effect of variation of the ratio of R to the ro from 1.3 to 6 and length from 1 to 100 on the Average effectiveness	*79*
Fig. B- 2	Temporal temperature profile for Iterative CFD simulations cases for confirming the preliminary design	*81*

Nomenclature

C_p	Specific heat	[J.kg^{-1}.°C^{-1}]
$\boldsymbol{\beta}$	Liquid-fraction of PCM	[-]
H	Specific enthalpy of the PCM	[J.kg^{-1}]
k	Thermal conductivity	[W.m^{-1}.K^{-1}]
L	Length of the tank	[m]
L	Latent heat of fusion	[J.kg^{-1}]
Q	Energy stored in PCM	[J]
$\dot{Q}_{PCM}$	Heat transfer rate	[J.s^{-1}]
r	Radial coordinate	[-]
r_o	Tube radius	[m]
R	Shell radius	[m]
Re	Reynolds number	[-]
SE	Storage effectiveness	[-]
t	Time	[s]
t_c	Useful charging hours	[h]
t_d	Useful discharging hours	[h]
T	Temperature	[°C]
u	Velocity	[m.s^{-1}]
z	Axial coordinate	[-]

Subscripts

HTF	Heat transfer fluid
h	Highest
l	Lowest
m	Mean
MP	Melting point
PCM	Phase change material
r	Reference
z	Axial direction

Greek letters

α	Thermal diffusivity	[$m^2.s^{-1}$]
ρ	Density	[$kg.m^{-3}$]
ε	Specific energy	[$J.kg^{-1}$]

List of abbreviations

CCD	Central composite design
CFD	Computational fluid dynamics
CSP	Concentrated solar power
HTF	Heat transfer fluid
LCOE	Levelized cost of electricity
LDES	Long-duration energy storage
LHTES	Latent heat thermal energy storage
PCM	Phase change material
PV	Photovoltaics
RSM	Response surface methodology
SHTES	Sensible heat thermal energy storage
SPT	Solar power tower
TES	Thermal energy storage

Chapter 1 Introduction

1.1 Motivation

The global temperature is expected to rise above the 1.5 °C limits in the Paris agreement unless immediate action is taken [1]. Efforts must be made across all sectors to reduce emissions in order to achieve the agreement's commitments. Net-zero emissions from the power sector are expected to be necessary by 2040 for global decarbonization, as it accounts for about one-third of total greenhouse gas emissions. Thus, innovative solutions are needed to transition power generation from fossil fuel to renewable energy and to meet the increasing demand for electricity at an affordable cost. It has been observed that during the time period of 2010 – 2021, the global weighted average LCOE (levelized cost of electricity) from renewable energy technologies like solar photovoltaics (PV) and concentrated solar power (CSP) declined by 88% and 66%, respectively, as shown in *Fig. 1.1* [2]. This reduction in the LCOE of renewable energy makes it an attractive alternative to traditional fossil fuel-based power generation.

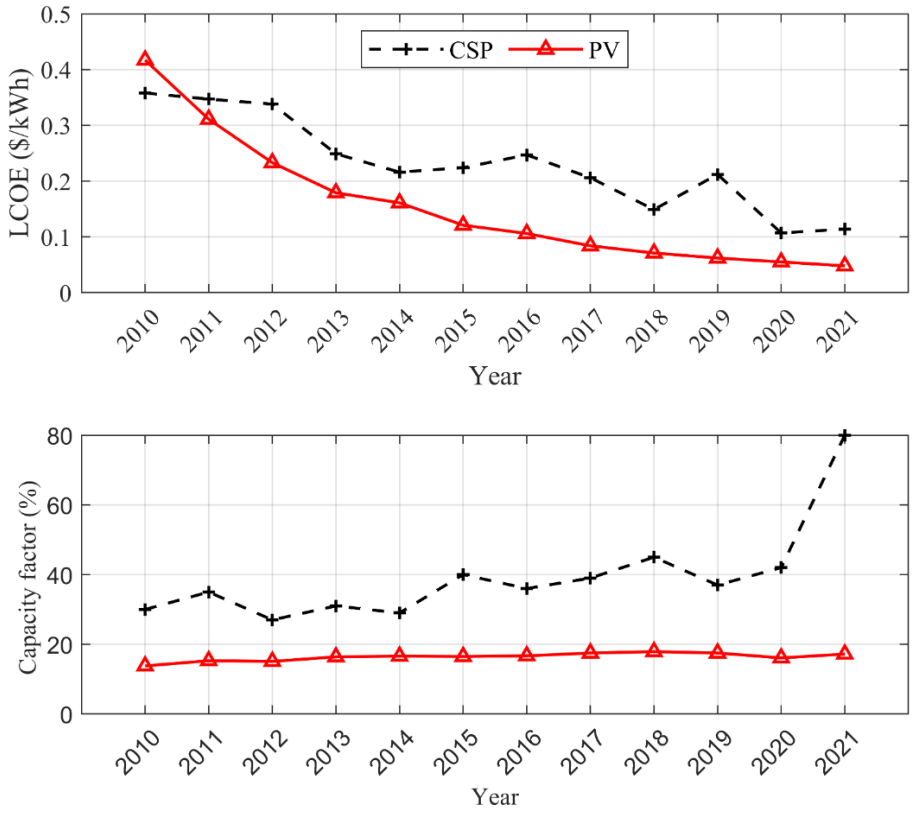

Fig. 1.1 Global weighted average LCOE and capacity factors for CSP and PV between the year 2010-2021 [2]

Despite the economic advantage, the intermittent nature of renewable energy resources hampers their ability to replace fossil fuel-based power generation (for example, solar energy generation is only possible during sunny hours). Besides the unavailability of solar power after sunset, the imbalance between solar energy production and electricity demand has created unexpected volatility in the energy supply. The "duck chart" (termed coined by California independent system operator – CASIO, due to the chart's resemblance to a duck) shows the "net load" for 31st March (see *Fig. 1.2*), which is calculated from the difference between the total electricity demand and the available solar energy during the time period of 2012 – 2020 [3]. Traditionally, conventional power generation technologies are used to meet this net load. However, from 2012 to 2020, the net load decreased dramatically in the middle of the day (~ 1 – 2 p.m., duck's belly) due to the increased penetration of solar and wind energy in the energy mix over the years. Due to the nature of electricity demand, there are morning (~ 8 a.m.) and evening (~ 9 p.m.) ramps in the chart. Due to the steep ramps (especially a surge of ~ 13,000 MW in three hours in the evening), conventional technologies cannot generate power in just limited hours since it requires a long startup time. This issue can be resolved by deploying *affordable energy storage* technologies to deliver electricity according to demand.

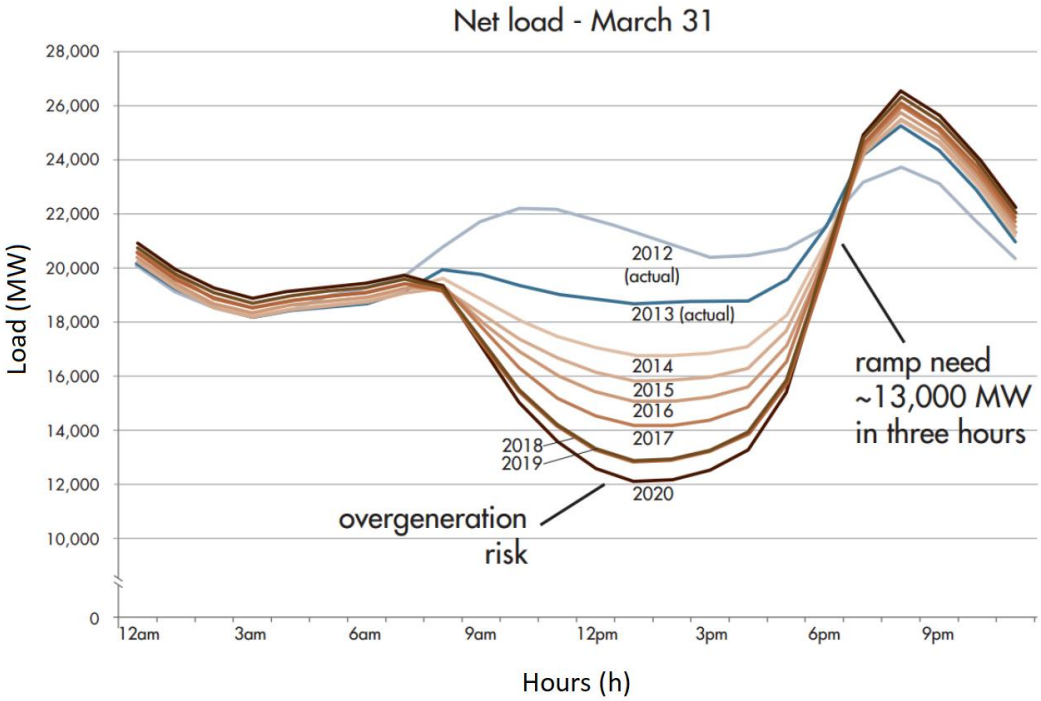

Fig. 1.2 Impact of increasing penetration of solar energy on California state's electrical load [3]

Electrochemical energy storage technologies are available for utility-scale power plants (including lead-acid and lithium-ion batteries). However, these technologies have a limited storage capacity of fewer than 3 hours, and their high storage cost makes them non-reliable for long-duration energy storage (LDES) [4]. Due to the limited electrochemical energy storage options, the global weighted average capacity factor[1] of solar photovoltaics technology is currently only 17.2% (see *Fig. 1.1*). However, CSP technologies have achieved an 80% capacity factor due to the integration of low-cost and affordable thermal energy storage (TES) systems which allows it to generate power with intraday and interday flexibility [5].

Concentrated solar power (CSP), where solar energy is concentrated over a small area (called the receiver) to generate heat, which is then used to produce electricity by running a steam Rankine cycle [6–10]. Presently, 17.64 TWh of CSP is installed worldwide, which is expected to reach 183.8 TWh by 2030 [11]. Most of the current generation of CSP plants can produce steam temperatures up to 390 °C [12]. Such plants are only suitable for operating a sub-critical Rankine cycle for which the thermal efficiency is limited to about 42% [13]. Such plants typically have a higher LCOE than traditional power plants and can only generate electricity during the daytime when solar radiation is available [14]. To improve the CSP plant's performance and make it cost-competitive with traditional power generation, higher steam temperatures (630 °C) could be achieved in such a way that the plant can run the ultra-supercritical Rankine cycle, with cycle efficiencies as high as 49.6% [15].

Furthermore, the intermittency in power generation can be addressed by integrating thermal energy storage (TES) systems in CSP plants [13,16,17], increasing the plant's capacity factor. A TES system uses a storage material to store excess heat from the solar receiver during the day when solar energy is abundant, which can then be used during periods of low or no solar radiation for continuous power generation. TES systems can be classified as (a) sensible-heat TES (SHTES) and (b) latent-heat

[1] Capacity factor of a plant represents the ratio of actual energy produced to maximum energy that can be produced during a particular period.

TES (LHTES) systems. In the former, energy is stored as sensible heat in the storage material, whereas the latter utilizes its latent heat by undergoing a phase transition. Most current CSP plants are integrated TES systems using two-tank molten salt SHTES systems [17–22]. Such SHTES systems are easy to design and operate. However, two-tank molten salt TES system cannot be deployed for high-temperature next-generation power cycles as the molten salt corrode stainless steel structural materials and the nitride salt (a constituent of molten salt) degrades at a temperature over 600 °C [23–25]. Thus, this study considers the design and development of LHTES systems for the next generation of CSP plants since these systems can operate at a higher temperature, require relatively lesser volume, and have lower capital investment [26–30].

1.2 Objectives of the thesis

A detailed literature review provides a better understanding of the state-of-art technologies and offers existing research gaps in designing and developing a high-temperature LHTES system. Therefore, the present study concentrates on designing LHTES systems for CSP plants, and subsequent objectives are framed as follows:

- To develop a mathematical model for simulating the charging and discharging behavior of an LHTES system
- To analyze the geometrical and operational parameters of an LHTES system and study their effect on the system's performance
- To perform multi-objective design optimization of an LHTES system for different CSP plant configurations
- To investigate the compatibility of steel structural materials with molten AlSi12 (PCM) for the LHTES system

1.3 Organization of the thesis

This thesis is organized in the following way:

Chapter 1 This chapter provides the motivation and rationale of the thesis along with research objectives.

Chapter 2: This chapter summarizes the current state-of-the-art of high-temperature LHTES systems for CSP plants. In addition, it also highlights the research gaps.

Chapter 3: This chapter discusses the mathematical model and design optimization procedure for LHTES systems.

Chapter 4: This chapter analyzed and discussed the parametric analysis of the LHTES system for a CSP plant under realistic operating conditions.

Chapter 5: This chapter provides a multi-objective design optimization methodology for designing an LHTES system for hybrid PV-CSP and baseload CSP plant configuration.

Chapter 6: This chapter investigates the compatibility of steel structural materials with AlSi12 alloys-based phase change material. This study also includes an analysis to enhance its corrosion resistance properties by using different ceramic coatings on steel.

Chapter 7: The chapter summarizes the thesis work with an emphasis on the major contributions and future recommendations.

Chapter 2 Literature review and research gaps

2.1 Literature review on latent heat thermal energy storage (LHTES) systems

An LHTES system is essentially a regenerative type of heat exchanger that transfers energy from a heat transfer fluid (HTF), heated in the solar receiver, to a phase change material (PCM), which undergoes a solid-to-liquid phase change during the charging process [31,32]. The stored energy can be retrieved by discharging the LHTES system, during which the PCM undergoes a liquid-to-solid phase change and transfers energy back to the HTF. The present study is focused on designing and developing the LHTES system for CSP applications.

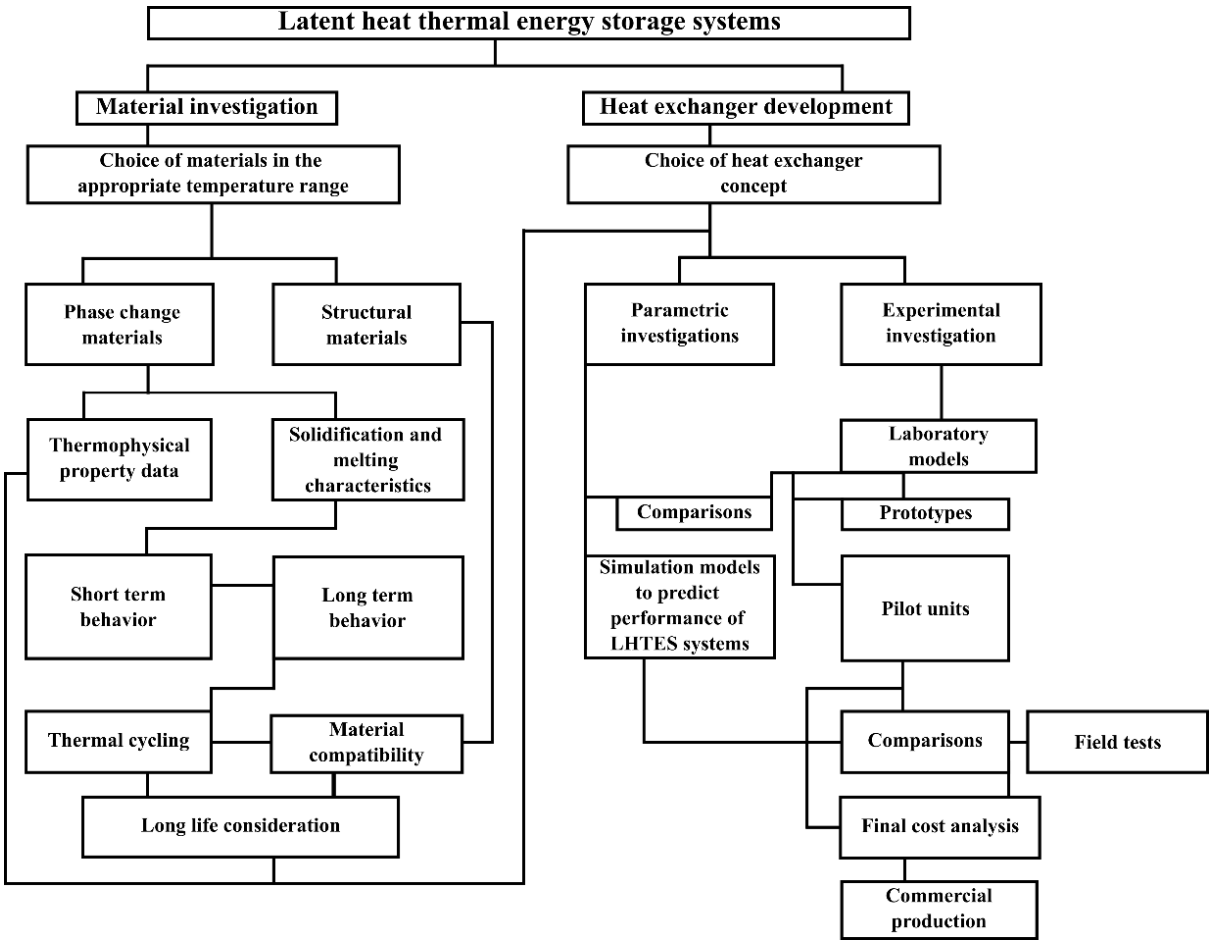

Fig. 2.1 Developing an LHTES system: an overview [128]

As Abhat [33] mentioned, the development of an LHTES system involves two study areas (*Fig. 2.1*): a) PCM and structural materials investigation and b) heat exchanger design. An ideal PCM candidate should have superior thermophysical properties (high thermal conductivity and latent heat) and a suitable melting temperature for the CSP application. It should be thermally stable after multiple solidification/melting cycles. Similarly, for long-life consideration, PCM should be compatible with the structural material of the LHTES system. Simultaneously, the LHTES system should be numerically and experimentally investigated before finalizing the production of the commercial design (see *Fig. 2.1*). Thus, PCM material selection, geometrical design, HTF's velocity, boundary conditions, and compatibility issues between PCM and HTF are discussed in following subsections for developing LHTES system.

2.1.1 PCM material selection

Various kinds of PCMs (e.g., organic, inorganic, and eutectic) can be used in an LHTES system, depending on the application [16,33,34], as shown in *Fig. 2.2*. Metallic PCMs and their alloys are ideal candidates for high-temperature LHTES (HT-LHTES) systems for the next generation of CSP plants due to their high melting point temperatures, high thermal conductivities, linear melting interfaces, and small expansion volumes [35–37].

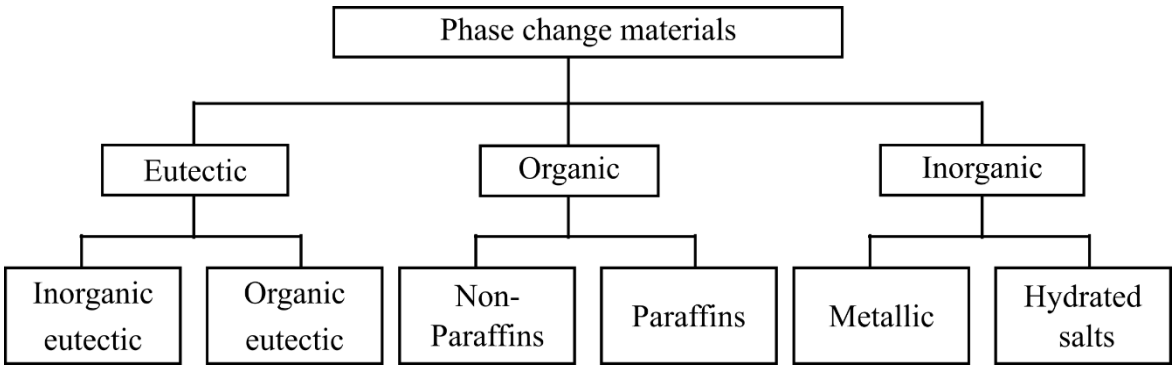

Fig. 2.2 Classification of PCMs

Thus, several metallic PCMs (and their alloys) have been studied for HT-LHTES systems. For example, Risueno et al. [38–41] investigated magnesium and zinc-rich eutectic metal alloys PCMs. Their results have suggested study found that PCMs have superior thermophysical properties compared

with molten salt, and there is no degradation in thermophysical properties after multiple charging-discharging cycles. Similarly, other researchers [42–45] have investigated different metals and their PCM as alloys (like, Al25Cu6Si, Al34Mg6Zn, Mg25Cu15Zn, Mg84Cu16, and Mg59Cu41; at Wt %); however, they are not suitable as PCM at higher temperatures due to low melting temperature (< 550 °C) and latent heat (< 550 kJ/kg). To find a suitable PCM for a higher temperature, the thesis author illustrated different metallic PCMs based on the thermophysical properties between the temperatures of 400 and 700 °C. The investigation concluded that AlSi12, a eutectic aluminum alloy containing 12% silicon by weight, is the most suitable PCM candidate for the ultra-supercritical Rankine cycle due to its melting temperature (576 °C), thermal conductivity (160 W/m K), and latent heat (560 kJ/kg). Note that the subsequent work is purposefully not included in this thesis.

Likewise, Kotze et al. [46] presented a concept of integrating an HT-LHTES system in a CSP plant with AlSi12 as the PCM. They found that the AlSi12-based HT-LHTES system had higher charging and discharging rates and lower capital investment than a conventional SHTES system. Rea et al. [48] performed experiments on an LHTES system prototype with AlSi12 as the PCM in another study. They reported that the system could receive and uniformly distribute heat throughout the PCM, despite the small temperature gradients (< 5 °C) present in the PCM due to its high thermal conductivity. A few other researchers [47,48] have also investigated the thermal reliability of AlSi12 and found that nearly all its thermophysical properties remain unchanged, even after multiple charging and discharging cycles. Due to AlSi12's promising nature, researchers measured the thermophysical properties as a function of temperature [49,50] and thermal stability [47,48]. These studies concluded that there is no significant change in thermophysical properties even after 1000 charging and discharging cycles. Thus, it concludes that AlSi12 is a promising PCM material for the HT-LHTES systems in CSP plants.

2.1.2 Geometrical design

In addition to proper PCM selection, it is important to correctly design and operate the LHTES system for effective heat transfer between the PCM and the HTF. To achieve this, the geometry of the LHTES system, which is essentially a heat exchanger, should be optimized. Typically, LHTES systems have a

shell-and-tube type geometry (the HTF flows through the tubes, and the PCM occupies the annulus region between the shell and the tubes, as shown in *Fig. 3.2a*) due to its relatively simple construction and high performance [51]. Several investigations [26,52–55] have conducted geometrical optimization for LHTES systems by varying parameters such as its length (L), the ratio of its length to the tube radius (L/r_o), and the ratio of shell to the tube radius (R/r_o), as shown in *Table 2.1*. For example, Bellecci and Canti [54,55] conducted numerical simulations of LHTES systems. They recommended R/r_o < 4 and L/r_o > 20 for ensuring effective heat transfer between the HTF and PCM and for the proper utilization of the latent heat capacity of the PCM. Tehrani et al. [26] concluded that increasing L/r_o increases the total power delivery from the LHTES system to the power block as well as the capital cost of the LHTES system; thus, they recommended L/r_o between 80–120 as the optimum values.

2.1.3 HTF's velocity and boundary conditions

Apart from the geometrical optimization of the LHTES system, it is also essential to carefully select the Reynolds number (Re) of the HTF flow since an increase in the Reynolds number increases the heat transfer between the HTF and the PCM, and thereby, reduces the charging and discharging time of the system [56]. The increase in heat transfer at a higher Reynolds number is primarily due to the increased temperature difference between the HTF & PCM and the heat transfer coefficient varies along the length of the tube, with a higher coefficient observed during the developing flow regime whereas the heat transfer coefficient is not significantly affected by the Reynolds number in the laminar region. Thus, Kalapala et al. [57] have recommended maintaining a laminar flow of HTF in the LHTES system.

Table 2.1 Literature on shell-and-tube-based LHTES system

T_m (°C)	Charging/ Discharging	Convection in PCM zone neglected	Method	L (m)	R/r_o (-)	L/r_o (-)	Re	Ref.
26	Char.	No	2D Num	-	1.2-5	50-300	1043-4107	[58]
26	Char./Dis.	No	2D Num	1	2	156	151.5-1515	[59]
26	Char.	No	2D Num	1	1.8	166	-	[60]
26	Dis.	Yes	2D Num/Exp.	1	3.7	60	300-2000	[61,62]
26	Char.	No	2D Num	1	1.6	156	20-2000	[63]
26	Char./Dis.	No	2D Num	1	1.6	156	-	[64,65]
35	Char./Dis.	No	CFD/ Exp.	0.4	2.9	52	150	[66]
36	Char.	No	2D Num	0.2	8.4	20	-	[67,68]
36	Char.	No	Exp.	0.17	6	10	-	[69]
29-46	Char.	Yes	2D Num	3.2	1.09-1.2	40-96	2000	[70]
20-80	Char.	Yes	2D Num	2	2	200	-	[71]
51	Char./Dis.	No	CFD	1	3.9	24	150	[72]
58	Char./Dis.	No	CFD	1	4	60	-	[73]
60	Char./Dis.	No	2D Num/CFD/Exp.	0.75	-	21.4	200	[74,75]
75	Char./Dis.	No	Exp.	0.5	3.3	34	1000	[76]
118	Char./Dis.	No	Exp.	1	2.8	38	-	[77]
121	Char./Dis.	No	Exp.	0.9	2.4	40	400	[78]
169	Char./Dis.	Yes	2D Num	1.4	1.25	174	1500	[79]
215	Char.	No	2D Num	1	-	-	-	[80]
230	Char./Dis.	No	CFD	0.5	5	70	157	[81]
306	Char./Dis.	No	CFD	0.6	3.15	58	1500	[82]
306	Char./Dis.	No	CFD	0.9	5.41	310	600	[83]
325-525	Char./Dis.	Yes	2D Num	1-5	1.3-3	20-200	-	[26]
325-525	Char./Dis.	No	CFD	0.5-2	1.5-3	30-120	2000	[84]
325-525	Char./Dis.	No	2D Num	2-20	2.3	40-1000	2200	[84]
400-600	Char.	Yes	2D Num	1	2	80	-	[85]
400-700	Char.	Yes	2D Num	1.2	2	240	150	[86]
550	Dis.	Yes	2D Num	10-150	1-3	20-300	700	[87]
734	Char.	Yes	2D Num	-	2.6-5	24-300	-	[54,55]
766	Char.	Yes	2D Num	1.5	2	120	1200	[52,88]

Note that the HTF temperature at the LHTES system's outlet would increase during the charging process, leading to higher HTF temperatures at the inlet of the receiver, thus adversely

affecting the receiver's performance [89]. In contrast, during the discharging process, the HTF temperature at the LHTES system's outlet would reduce as the Reynolds number is increased, leading to a lower HTF temperature at the inlet of the steam generator. This low HTF temperature would result in a decline in the quality of the steam produced by the generator, which would not only decrease the efficiency of the power cycle but also can damage the turbine blades [90]. Consequently, it is crucial to keep the exit temperatures of the HTF within suitable limits during the charging and discharging processes, so as not to adversely affect the efficiencies of the CSP plant's central receiver and steam turbine. Those limits are called the charging and discharging 'cutoff' temperatures [89]. Thus, to limit the HTF's exit temperatures during the charging and discharging processes below their respective cutoff values and to ensure reasonable charging and discharging time, the Reynolds number should neither be too high nor too low.

2.1.4 Compatibility issue between PCM and steel structural materials

The high-temperature LHTES systems with AlSi12 as PCM can be integrated into next-generation power cycles for higher efficiencies [15]. However, few studies [91,92] reported that the structural material degrades due to high-temperature corrosion between structural material and molten PCM. One of the reasons behind the AlSi12 reacting with structural materials is due to the dissolution of elements like chromium (Cr) and nickel (Ni) in the molten Al [93]. To increase the compatibility between structural material and AlSi12, researchers investigated ceramic material with molten AlSi12; for example, Zhao et al. [48] investigated Al_2O_3, AlN, SiC, Si_3N_4, BN, and ZrO_2. They have concluded that AlN and Al_2O_3 show excellent corrosion resistance properties, whereas other ceramics materials, like Si_3N_4, BN, and ZrO_2, react with molten AlSi12 and form products AlN and Al_2O_3, which are corrosion resistant. Fukahori et al. [50] investigated AlN, Al_2O_3, SiC, Si_3N_4, and SiO_2 with AlSi12, and their study concluded that AlN, Al_2O_3, and Si_3N_4 have superior corrosion resistance. As ceramics are expensive, they can be used as a coating over steel. Dindi et al. [94] investigated BN-based ceramic coating over steel. Their results suggested that the ceramic coating has excellent corrosion-resistant properties. Rea et al. [92] performed a similar investigation with MgO-ZrO_2 ceramic coating over steel and revealed

that structural material starts to dissolve in the molten AlSi12 within hours. However, ceramics are inert in the molten AlSi12 environment [48,50,94]; still, molten AlSi12 can penetrate under the ceramic coats and interact with structural materials due to the presence of pores, pinholes, and micro cracks on the coated ceramic layer after the plasma-spay method [92].

2.2 Research gaps and novelty of the present study

The investigations mentioned above confirm that for the effective operation of an LHTES system integrated into a CSP plant, it is essential to have a well-designed geometry. However, the following knowledge gaps remain in the literature that motivates the aim of the thesis:

- Almost all the existing studies have overlooked the role of cutoff temperatures on the performance of LHTES systems designed for CSP plants. However, the present investigation demonstrates the crucial role of cutoff temperatures in determining the LHTES system's performance in terms of useful charging and discharging hours and energy storage capacity.

- In addition, most previous investigations have studied the performance of LHTES systems for a single cycle of charging and discharging, which would be significantly affected by the system's initial state. However, the present study examines the LHTES system's performance under multiple charging and discharging cycles until attaining the periodic steady-state conditions, which makes the performance assessment independent of the system's initial conditions.

- Several previous parametric studies provide design recommendations for the geometrical and operational parameters of LHTES systems. However, all of them are plagued by the two aforementioned issues, which means that their results might not be applicable for LHTES systems integrated into CSP plants under realistic operating conditions. Thus, to the best of the author's knowledge, the present work reports the first comprehensive assessment of various geometrical and operational parameters of the LHTES system to identify their effects on the system's performance under conditions that closely mimic its real-world operation.

Furthermore, an optimization study is also conducted to propose an LHTES system design that can achieve a high-performance level.

- Despite the extensive research that proves AlSi12 as a good PCM for high-temperature TES, there is no study on compatible steel structure material and suitable ceramic coating. Thus, the present study aims to solve both the research gaps and test the compatibility of structural materials: Steel - SS316, SS202, and P91 steel, as well as investigate the corrosion resistance protection of ceramic coating over the steel. The novelty of the current study allows plant designers to make informed choices regarding the selection of suitable structural materials and ceramic coating.

Chapter 3 Mathematical model and design optimization of the TES system

This chapter outlines the LHTES system's description, mathematical model (governing equations, boundary conditions, model validation, grid, and time independence test), and design optimization methodology for performing the parametrical analysis (will be discussed in *Chapter 4*) and design optimization (*Chapter 5*) of the LHTES system.

3.1 Thermal energy storage system description

This study investigated an LHTES system's performance that was assumed to be integrated into a 167 MWe solar power tower (SPT) type CSP plant, as shown in *Fig. 3.1*. A brief description of the CSP plant operation relevant for the design of the LHTES system is presented here, whereas additional plant details are given in the investigation done by Kolb [15]. The studied CSP plant was a future-generation plant, in which HTF at 650 °C temperature powers an ultra-supercritical steam-Rankine cycle. As shown in *Fig. 3.1*, in the CSP plant, steam (at 630 °C and 330.9 bar) produced in a steam generator runs a 167 MWe turbine. The steam generator receives thermal energy from the HTF (at 650 °C) heated in the plant's central receiver. After delivering thermal energy to the steam generator, the cold HTF (at 336 °C) leaves the generator and enters the central receiver for continuous plant operation. Thus, the HTF inlet temperatures to the LHTES system during the charging and discharging processes will operate between 650 °C and 336 °C, respectively.

Aluminum silicon eutectic alloy (AlSi12) was selected as the PCM for the LHTES system due to its excellent thermophysical properties, as already mentioned in the literature, and Halotechnics SaltStream-700 (SS700) was selected as the HTF since it is stable at the high operating temperatures encountered in the system [95,96]. The data corresponding to the thermophysical properties of the PCM and HTF are adopted from Kotze et al. [46] and Vignarooban et al. [97], respectively. Note that since the PCM (AlSi12) used in this research is a eutectic alloy of aluminum and silicon, its melting and freezing occur at the same temperature, i.e., the eutectic point temperature (refer to *Table 3.1*). Here, the PCM and HTF are separated by stainless steel (SS316) tubes, which act as a wall between them [98]. The thermophysical properties of AlSi12, SS700, and SS316 are shown in *Table 3.1*.

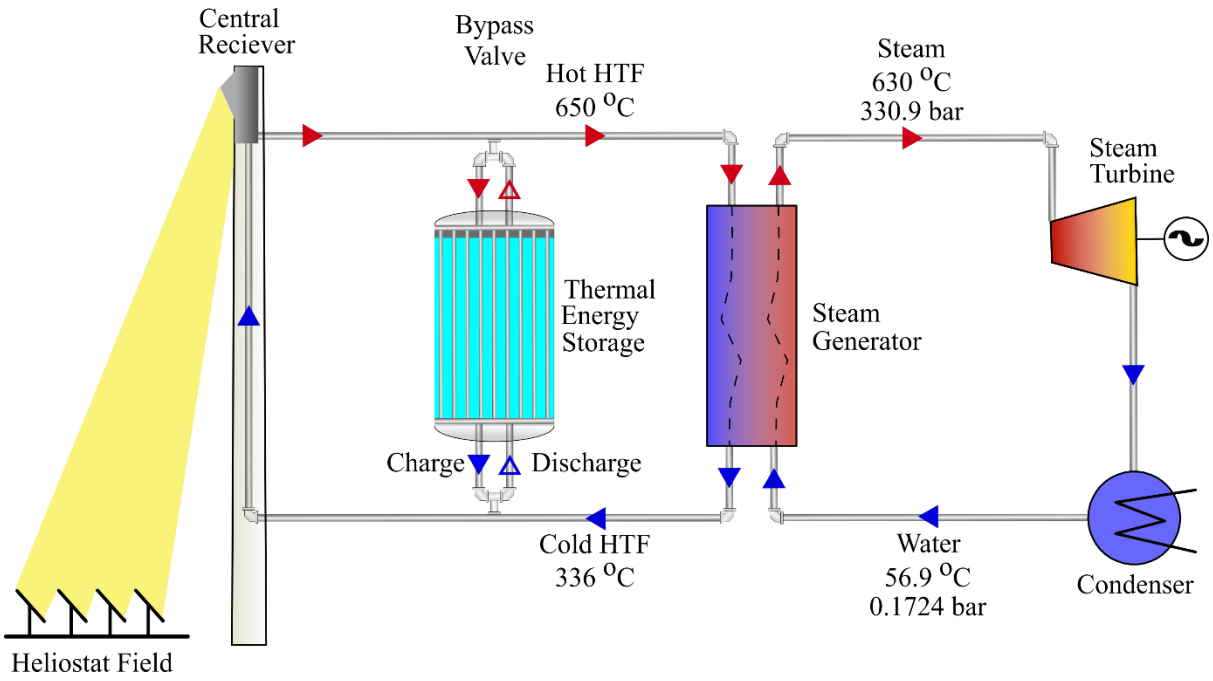

Fig. 3.1 Schematic of a thermal energy storage system integrated into a 167 MWe concentrated solar power plant.

Table 3.1 Thermophysical properties of the PCM and HTF

	Density (kg/m^3)	Specific heat (J/kg-°C)	Thermal conductivity (W/m-°C)	Latent heat (J/kg)	Eutectic point (°C)	Viscosity (kg/m-s)
PCM (AlSi12)	2700	1500	160	560000	567	0.0013
Tube (SS316)	8000	400	15	-	-	-
HTF (SS700, Fluid phase)	2205	790	0.34	-	253	0.004

This investigation studied a vertically oriented shell-and-tube type LHTES system, which comprised an outer shell containing multiple tubes (with shell radius R, outer tube radius r_o, and length L) inside it, as shown in *Fig. 3.2a*. The tubes were uniformly spread across the system with a center-to-center distance of $2R$ between them. The HTF flowed through the tubes for charging and discharging the PCM, which is stored in the region between the shell and the tubes. During the charging process, the HTF flowed from the top (Z/L = 1) to the bottom (Z/L = 0), whereas the flow direction was reversed during the discharging process as recommended by Longeon et al. [66], for effective charging and discharging the system. The performance of the LHTES system was determined from that of a unit cell consisting of a single tube and the annular region (of radius R, containing the PCM) surrounding it by

assuming that the system behaves as a composite of multiple identical unit cells (see *Fig. 3.2b*) [26,81,98–101]. Note that this assumption essentially means that the PCM occupying the region between the unit cells does not contribute to energy storage, which seems reasonable considering that the PCM present in this region will be at the largest radial distance from the HTF flowing through the system.

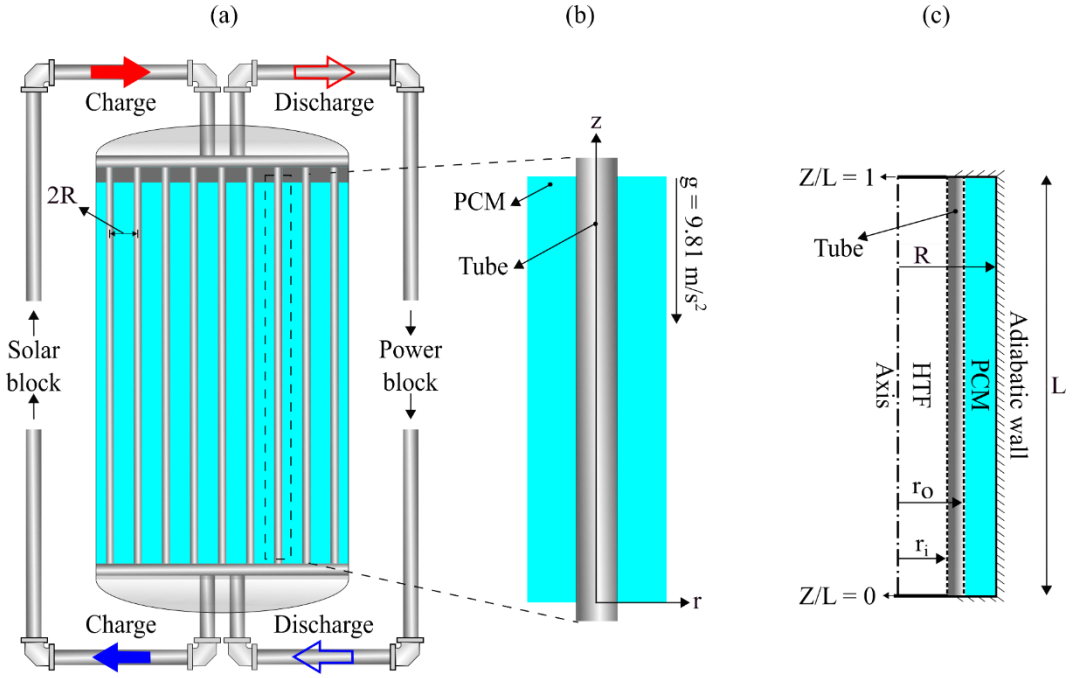

Fig. 3.2 a) The complete LHTES system, b) a unit cell of the LHTES system, and c) the 2D axisymmetric geometry used for the CFD modeling of the LHTES system.

3.2 Mathematical formulation

The unit cell was assumed to be axisymmetric since the LHTES system was in the vertical orientation; thus, a 2-dimensional (2D) domain could represent the unit cell [102,103], as shown in *Fig. 3.2c*. Therefore, 2D-axisymmetric CFD simulations were conducted to study the unit cell's thermal performance using commercial CFD software (ANSYS Fluent 18.1).

3.2.1 Governing equations for the PCM

The CFD simulations used a technique developed by Prakash et al. [104] to model the heat transfer and phase change phenomena in the PCM. In this technique, the liquid-fraction of the PCM (fraction of the

cell volume that is in the liquid form) is computed at each time step, based on an enthalpy balance given by:

$$\rho_{PCM}\frac{\partial H_{PCM}}{\partial t} = k_{PCM}\left(\frac{1}{r}\frac{\partial}{\partial r}\left(r\frac{\partial T_{PCM}}{\partial r}\right)+\frac{\partial^2 T_{PCM}}{\partial z^2}\right) \qquad \textit{Eq. 3.1}$$

where, H_{PCM} is the specific enthalpy of the PCM; T_{PCM} its temperature, and k_{PCM} its thermal conductivity; t is the time, and z and r are the coordinates in the axial and radial directions, respectively.

Note that the above equation neglects heat transfer due to natural convection in the PCM, which was reasonable since all the investigated LHTES system geometries satisfied the condition ($\frac{R^2-{r_o}^2}{2r_oL} \leq 0.005$) recommended by Tehrani et al. [105] for neglecting natural convection effects in a shell-and-tube type LHTES system. The primary reason for neglecting natural convection effects was to save on computational time since each simulation had to be run for a very long duration (ten days) to achieve periodic steady-state conditions.

The specific enthalpy of PCM was computed as the sum of its sensible and latent enthalpy by using:

$$H_{PCM} = h_r + \int_{T_r}^{T_{PCM}} C_p dT + \beta L \qquad \textit{Eq. 3.2}$$

where, h_r is the reference specific enthalpy, T_r the reference temperature, C_p the specific heat capacity of the PCM, L its latent heat capacity, and β its liquid-fraction (mass of liquid divided by the total mass). Note that the PCM (AlSi12) under investigation was a eutectic alloy, which melts and solidifies without developing a 'mushy zone' and has a fixed melting point temperature. Thus, PCM's liquid-fraction can be calculated by using the following equations:

$$\begin{cases} \beta = 0 & if \;\; T_{PCM} < T_{MP} \\ 0 < \beta < 1 & if \;\; T_{PCM} = T_{MP} \\ \beta = 1 & if \;\; T_{PCM} > T_{MP} \end{cases} \qquad \textit{Eq. 3.3}$$

where, T_{MP} is the melting point temperature of the PCM. Since there is no 'mushy zone' formation for AlSi12 (as the solidus temperature and liquidus temperature coincide at a point known as the eutectic point), a method based on specific heat was used for solving *Eq. 3.2* and *Eq. 3.3* [104,106,107].

3.2.2 Governing equations for the tube and HTF

For modeling the heat transfer in the tube and HTF, the following equations were used:

$$\frac{\partial \mathrm{T_{tube}}}{\partial \mathrm{t}} = \alpha_{\mathrm{tube}} \left[\frac{1}{\mathrm{r}} \frac{\partial}{\partial \mathrm{r}} \left(\mathrm{r} \frac{\partial \mathrm{T_{tube}}}{\partial \mathrm{r}} \right) + \frac{\partial^2 \mathrm{T_{tube}}}{\partial \mathrm{z}^2} \right] \qquad \textit{Eq. 3.4}$$

$$\frac{\partial T_{HTF}}{\partial t} + u_z \frac{\partial T_{HTF}}{\partial z} = \alpha_{HTF} \left[\frac{1}{r} \frac{\partial}{\partial r} \left(r \frac{\partial T_{HTF}}{\partial r} \right) + \frac{\partial^2 T_{HTF}}{\partial z^2} \right] \qquad \textit{Eq. 3.5}$$

where, T_{tube} and T_{HTF} are the temperatures of the tube and the HTF, u_z its velocity of HTF in the axial direction. α_{tube} and α_{HTF} are the thermal diffusivity of the tube and HTF. *Eq. 3.5* assumes that the HTF flow was zero in the radial direction and neglects viscous dissipation [58].

The HTF flow was assumed to be laminar and fully developed during the charging and discharging processes and to be stationary otherwise (during charging-hold and discharging-hold processes, explained in the next *Section 3.2.3*). Thus, the velocity of the HTF was given by:

$$u_z(r,z) = \begin{cases} 2u_m \left[1 - \left(\frac{r}{r_i} \right)^2 \right] & \text{during charging} \qquad \textit{Eq. 3.6a} \\ -2u_m \left[1 - \left(\frac{r}{r_i} \right)^2 \right] & \text{during discharging} \qquad \textit{Eq. 3.6b} \\ 0 & \text{otherwise} \qquad \textit{Eq. 3.6c} \end{cases}$$

where, u_m denotes the mean flow velocity of the HTF, r the radial direction, and r_i is the tube's inner radius.

The governing equations (*Eq. 3.1*, *Eq. 3.4*, *and Eq. 3.5*) were discretized by using second-order schemes in space and time, While a PRESTO scheme was employed for the pressure equation because

second order schemes are in- compatible with the enthalpy-porosity approach in ANSYS Fluent. The grid resolution and the time-step for the CFD simulations were chosen after conducting grid and time independence studies (see *Section 3.2.6*). A convergence criterion of 10^{-6} was used for solving all the governing equations.

3.2.3 LHTES system operation and boundary conditions

The total charging time for the LHTES system was nine hours (when solar energy is available), during which hot HTF (at 650 °C) enters the system from Z/L = 1 (inlet during charging) and exits through Z/L = 0 (outlet during charging) while transferring its thermal energy to the PCM. Charging stops either after nine hours from its start or earlier if the average HTF temperature at Z/L = 0 reaches the charging cutoff temperature (376 °C), depending on the maximum inlet temperature limitations of the central receiver. This investigation selected the charging cutoff temperature as 376 °C (40 °C higher than the receiver's design point temperature) based on a similar criterion used by Tehrani et al. [108]. If the charging process stops before nine hours, a 'charging-hold' process starts for the remaining nine hours, during which the LHTES system was inactive (neither being charged nor discharged), and thus the HTF's flow velocity was zero during this process, as given by *Eq. 3.6c*. The relevant boundary conditions during the charging and charging-hold processes for the system are given in *Table 3.2*.

Since the total time used for the charging and charging-hold processes was nine hours, the remaining 15 hours were used to discharge the system. During the discharging process, cold HTF (at 336 °C) enters the system from Z/L = 0 and exits through Z/L =1 while gaining thermal energy from the PCM. Similar to the charging process, discharging also stops either after 15 hours or prior if the average temperature of the HTF at Z/L = 1 (outlet during discharging) reaches the discharging cutoff temperature (456 °C). The discharging cutoff depends on the minimum steam temperature requirement of the Rankine cycle.

A discharging cutoff temperature of 456 °C was chosen since supplying HTF below 456 °C to the Rankine cycle reduced the steam quality below 0.85 (high wetness level of the steam leads to efficiency loss and mechanical damage of the steam turbine), based on a simple thermodynamic analysis

(see *Fig. 3.1*). A similar cutoff criterion was also used by Tehrani et al. [108]. If the discharging process stops before 15 hours, a 'discharging-hold' process starts for the remaining hours during which the HTF is stationary. The thermal boundary conditions during the discharging and 'discharging-hold' processes are also presented in *Table 3.2*. In this way, the LHTES system has four operations in a 24-hour cycle: charging, charging–hold, discharging, and discharging–hold.

Note that during the discharging process, the hot HTF supplied by the LHTES should be between 650 °C (the design point) and 456 °C (the off-design point). This means that the PCM's melting point should also be between 456–650 °C; otherwise, the latent heat stored by the PCM will remain unutilized. Thus, the selection of AlSi12 as the PCM seems reasonable as its melting point temperature is 567 °C. Selecting a PCM with a higher melting point would likely result in poor utilization of its latent heat because as soon as the PCM attains a high temperature (say, around its melting point), the charging cutoff could be triggered and, consequently, terminates the charging process. On the other hand, a PCM with a low melting point temperature would produce low HTF temperatures during discharging, which would shift the power cycle away from the design point (650 °C).

Table 3.2. The thermal boundary conditions

Process	Boundary conditions for the HTF	Boundary conditions for the tube and PCM
Charging and Charging-hold	$T_{HTF}(z = L) = 650\,°C$, $\frac{\partial T_{HTF}}{\partial z}(z = 0) = 0$ $\frac{\partial T_{HTF}}{\partial r}(r = 0) = 0$, *and* $k_{HTF}\frac{\partial T_{HTF}}{\partial r}(r = r_i) = k_{tube}\frac{\partial T_{tube}}{\partial r}(r = r_i)$	$\frac{\partial T_{tube}}{\partial z}(z = 0) = 0$, $\frac{\partial T_{tube}}{\partial z}(z = L) = 0$, $\frac{\partial T_{PCM}}{\partial z}(z = 0) = 0$, $\frac{\partial T_{PCM}}{\partial z}(z = L) = 0$, $\frac{\partial T_{PCM}}{\partial r}(r = R) = 0$, *and* $k_{tube}\frac{\partial T_{tube}}{\partial r}(r = r_o) = k_{PCM}\frac{\partial T_{PCM}}{\partial r}(r = r_o)$
Discharging and Discharging-hold	$T_{HTF}(z = 0) = 336\,°C$, $\frac{\partial T_{HTF}}{\partial z}(z = L) = 0$, $\frac{\partial T_{HTF}}{\partial r}(r = 0) = 0$, *and* $k_{HTF}\frac{\partial T_{HTF}}{\partial r}(r = r_i) = k_{tube}\frac{\partial T_{tube}}{\partial r}(r = r_i)$	

This study performed CFD simulations for multiple charging-discharging cycles (a cycle of 24 hours and includes all the four processes given in *Table 3.2*) of the LHTES system to eventually attain periodic steady-state conditions. The periodic steady state was said to be achieved when the state parameters (PCM temperature and liquid-fraction) and storage effectiveness (SE) of the system were about the same for two successive days, as recommended by Liu et al. [103]. This investigation reached a periodic steady state on day ten, on which the SE value differed by less than 1% from that on day nine.

3.2.4 Model validation

CFD model was validated by simulating the LHTES system that was experimentally studied by Longeon et al. [66] since their geometry was similar to the unit cell used in this investigation (see *Fig. 3.3*), with r_o = 7.5 mm, R = 22 mm, and L = 400 mm. However, they used Rubitherm RT35 (melting point ≈ 35 °C) as the PCM and water as the HTF. The HTF flowed through the inner tube of the system from the top with a temperature of 52 °C with a velocity of 0.01 m/s and, thereby, heated the solid PCM stored in the annular region that was initially at a temperature of 22 °C. They measured the variation of PCM temperature with time at different radial locations (3 mm, 6 mm, and 9 mm outwards from the inner tube) at the center of the system (Z/L = 0.5), as shown in *Fig. 3.3*. Those measurements agreed well with present model predictions (see *Fig. 3.3*), thus validating the CFD modeling technique.

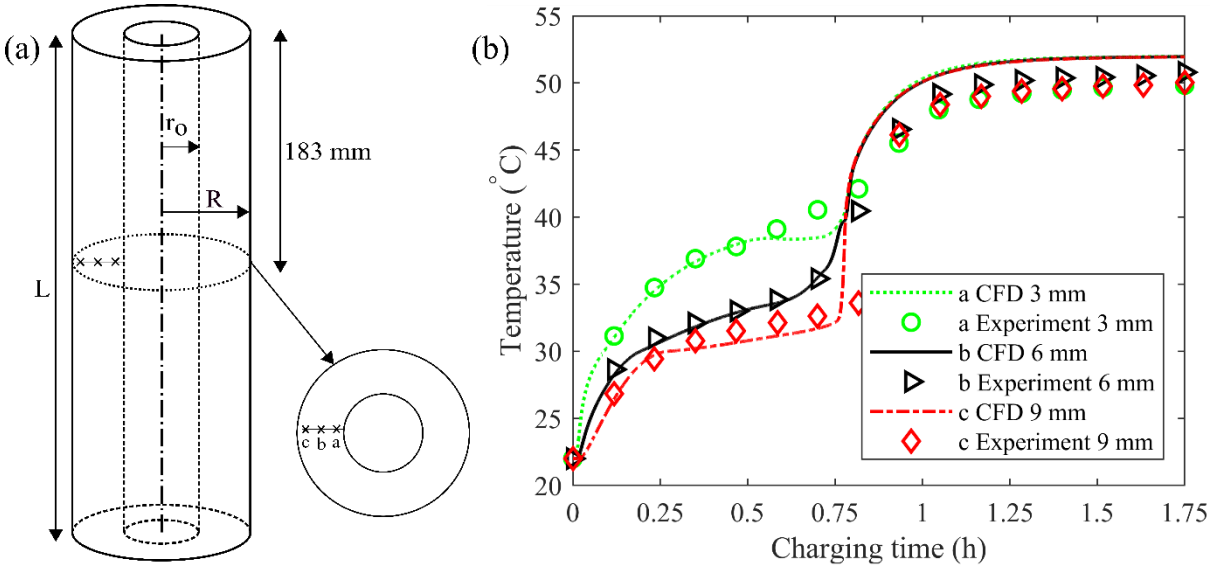

Fig. 3.3 Validation of CFD model using experimental results by Longeon et al. a) experimental setup and b) comparative graph between temperature profile from CFD model with corresponding thermocouples placed at three different locations reported by Longeon et al. [66]

Note that the CFD model used for the above–mentioned validation exercise included 'mushy zone' formation in the PCM by modifying *Eq. 3.3* to account for the difference between the melting and freezing point temperatures of Rubitherm RT35. The energy and liquid-fractions equations (*Eq. 3.2* and *Eq. 3.3*) were then solved using the method suggested by Voller and Swaminathan [107]. However, this effect was not present in AlSi12 since it is a eutectic alloy with the same melting and freezing point temperatures. Furthermore, the validation exercise also incorporated the effects of natural convection in the PCM (a body force term was added to *Eq. 3.1*). This is due to the fact that the LHTES geometry did not satisfy the criteria ($\frac{R^2-{r_o}^2}{2r_oL} \leq 0.005$) of Tehrani et al. [105] for neglecting natural convection. The validation model required about 9 hours of computational time on a 3.40 GHz Intel i7 quad-core processor with 16 GB of RAM for simulating only 1.75 hours of the experimental phenomenon. This CFD model (with natural convection) was computationally very costly for the present investigation since the aim was to simulate multiple charging-discharging cycles of the LHTES system for attaining periodic steady-state conditions (10 days of LHTES system operation). Thus, to save computational time, the present study neglected the effects of natural convection in the CFD model used, as discussed in *Section 3.2.1*.

3.2.5 Performance metrics

Overall, this investigation simulated multiple LHTES system designs to evaluate and optimize the performance of the system under periodic steady-state conditions by using the following performance metrics:

- Total stored energy (Q) was defined as the energy stored in the LHTES system after the completion of the charging process. It was calculated by integrating the heat transfer rate ($\dot{Q}_{PCM}$) from the HTF to the PCM over the complete charging duration (9 hours) as:

$$Q = \int_{t=0}^{t=9\ h} \dot{Q}_{PCM}\,(t)\,dt \qquad \textit{Eq. 3.7}$$

- Specific energy (ε) was defined as the energy stored in the LHTES system after completion of the charging process per unit mass of the PCM (m_{PCM}) and it was calculated as:

$$\varepsilon = \frac{Q}{m_{PCM}} \qquad \textit{Eq. 3.8}$$

- Storage effectiveness (SE) was defined as the ratio of the useful energy stored in the LHTES system after completion of the charging process to the maximum useful energy that can be stored in the system and it was given by:

$$SE\ = \frac{Q - Q_l}{Q_h - Q_l} \qquad \textit{Eq. 3.9}$$

where, Q_l and Q_h are the energy stored in the system at the lowest (336 °C) and highest system temperatures (650 °C), respectively, and both were calculated by assuming that the LHTES system was maintained uniformly at those temperatures.

3.2.6 Grid and time independence tests

This investigation used the preliminary system design (R = 2.8 cm, r_o = 1.3 cm, L = 10 m, u_m = 5.8 mm/s as recommended by Tehrani et al. [99]), for studying the grid and time independence of

the CFD results. CFD simulations were performed with three different grid sizes (see *Table 3.3*) for one charging (9 hours) and discharging cycle (15 hours) of the LHTES system.

Table 3.3 Investigated grid sizes

	Grid size in the axial direction (Δz, mm)	Grid size in the radial direction (Δr, mm)
Coarser grid	111	0.5
Medium grid	56	0.3
Fine grid	28	0.1

Fig. 3.4a shows the energy stored and dispatched from the LHTES system during the charging and discharging processes, respectively, by obtaining CFD simulations conducted with the different grids. This figure clearly shows that all the CFD simulations gave almost identical results, irrespective of the grid size. Therefore, the coarse grid was deemed sufficient for the CFD model and used for all the simulations discussed in the current work.

Similarly, for the time independence test, CFD simulations were performed with three-time steps: large (720 s), medium (360 s), and small (180 s), and computed the energy stored and dispatched from the LHTES system. *Fig. 3.4b* shows that the CFD results were almost identical with the medium and small time steps. Thus, the medium-time step was chosen for conducting all further investigations.

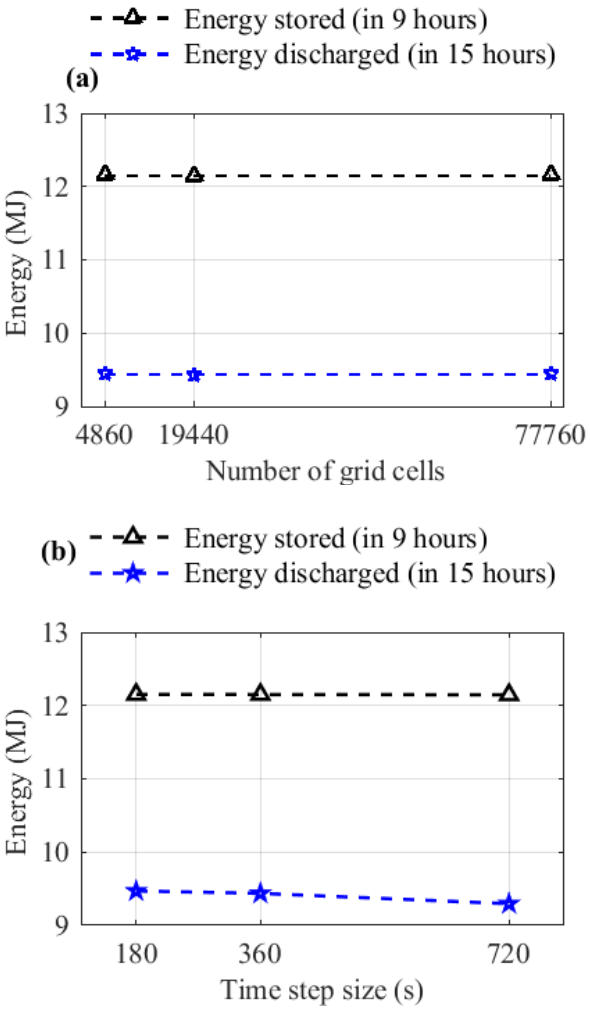

Fig. 3.4 CFD results of energy stored and dispatched from the LHTES system, as obtained with a) different grid sizes and b) different time-steps

3.2.7 Effect of operational strategy (realistic boundary conditions)

This investigation first studied the effect of charging and discharging cutoff temperatures on the performance of the LHTES system (preliminary design with R = 2.8 cm, r_o = 1.3 cm, L = 10 m, and u_m = 5.8 mm/s) by simulating it with and without the incorporation of cutoff temperatures. *Fig. 3.5a* compares the temporal variations of average HTF temperatures at Z/L = 1 (charging inlet and discharging outlet) and Z/L = 0 (discharging inlet and charging outlet) during the charging and discharging processes, with and without cutoff temperatures for the tenth day when the system reached periodic steady-state.

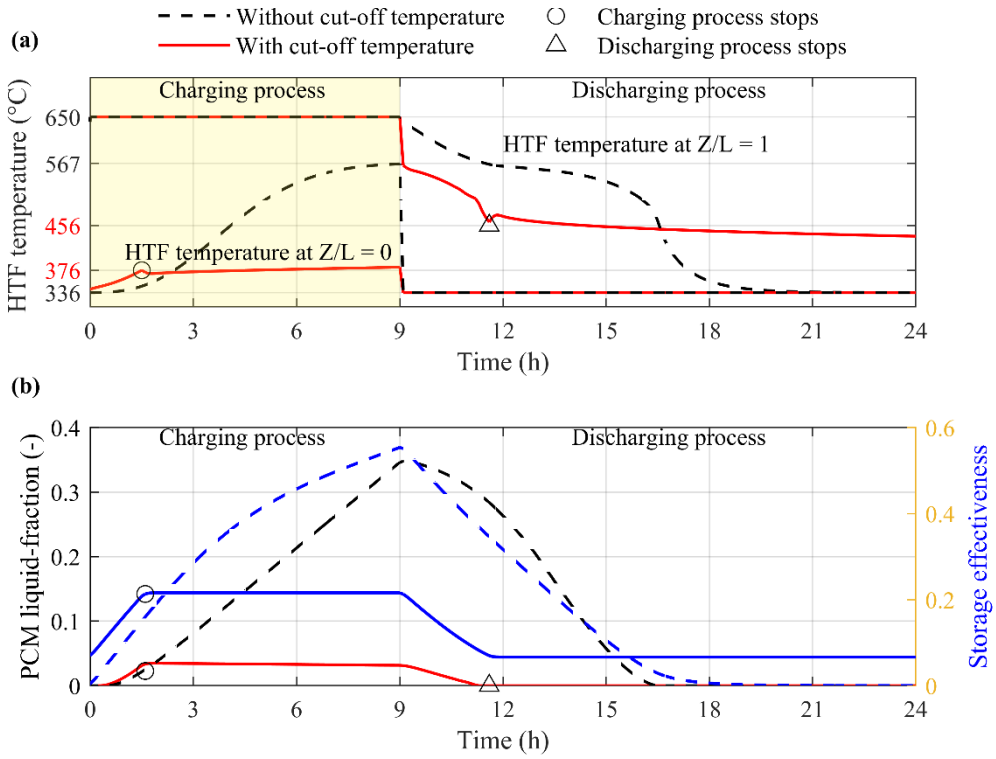

Fig. 3.5 Effect of cut-off temperatures on the temporal variation of the a) average HTF temperature and b) average PCM liquid-fraction under periodic steady-state conditions

As shown in *Fig. 3.5a*, during charging (0–9 h), the HTF temperature at the inlet (Z/L = 1) remains constant (650 °C) while its temperature at the outlet (Z/L = 0) increases with time in both the cases. The useful charging time of the system reduced from full 9 hours (without cutoff temperatures) to only 1.5 hours (with cutoff temperatures) since the HTF temperature at the outlet (Z/L = 0) exceeded the charging cutoff temperature (376 °C) after 1.5 hours (see the circular markers in *Fig. 3.5a*). Similarly, during the discharging process (9–24 h), the useful discharging hours reduced from full 15 hours (without cutoff) to only 2.6 hours (with cutoff) since the HTF temperature at the outlet (Z/L = 1) dropped below the discharging cutoff temperature (456 °C) after 2.6 hours (see the triangular markers in *Fig. 3.5a*).

In the case of without cutoff temperatures, the maximum value of the PCM's average liquid-fraction was 0.35 (see *Fig. 3.5b*), which was similar to those reported in the literature [99,103] since that case could be charged for full 9 hours. However, with cutoff temperatures, the maximum value of the PCM's liquid-fraction was only 0.03 (see *Fig. 3.5b*) due to the significant reduction in useful

charging hours. Thus, the total stored energy (Q), specific energy (ε), and storage effectiveness (SE) also decreased from 30.01 MJ (66.7% latent and 33.3% sensible) to 7.93 MJ (11.6% latent and 88.4% sensible), 0.58 MJ/kg to 0.15 MJ/kg, and 0.55 to 0.21, respectively, due to the implementation of cutoff temperatures. Since cutoff temperatures have a profound impact on the performance of the LHTES system, and these are also essential for the proper operation of the CSP plant's central receiver and steam turbine, thereby, they must be included in the design and analysis process of the LHTES system.

It is also worth comparing the performance of the LHTES system mentioned above (with cutoff temperatures) between the first and tenth day (when the system reached periodic steady-state) to study the effects of the initial conditions on the system's performance. *Fig. 3.6a* shows the temporal variations of HTF temperatures at Z/L = 0 (discharging inlet and charging outlet) and Z/L = 1 (charging inlet and discharging outlet) during the charging and discharging processes on the first and tenth day. This figure shows that the same LHTES system could be charged for 2.4 hours on the first day, whereas it could only be charged for 1.6 hours on the tenth day. The useful charging hours were much higher on day one than on day ten. This is due to the fact that the system was in a completely discharged state on the first day at a temperature of 336 °C. Similarly, while discharging, the system could deliver energy for 3.1 hours and 2.6 hours on the first and tenth day, respectively. Due to higher useful charging hours on the first day, the maximum liquid-fraction of the PCM on day one was also higher than that on day ten, as shown in *Fig. 3.6b*.

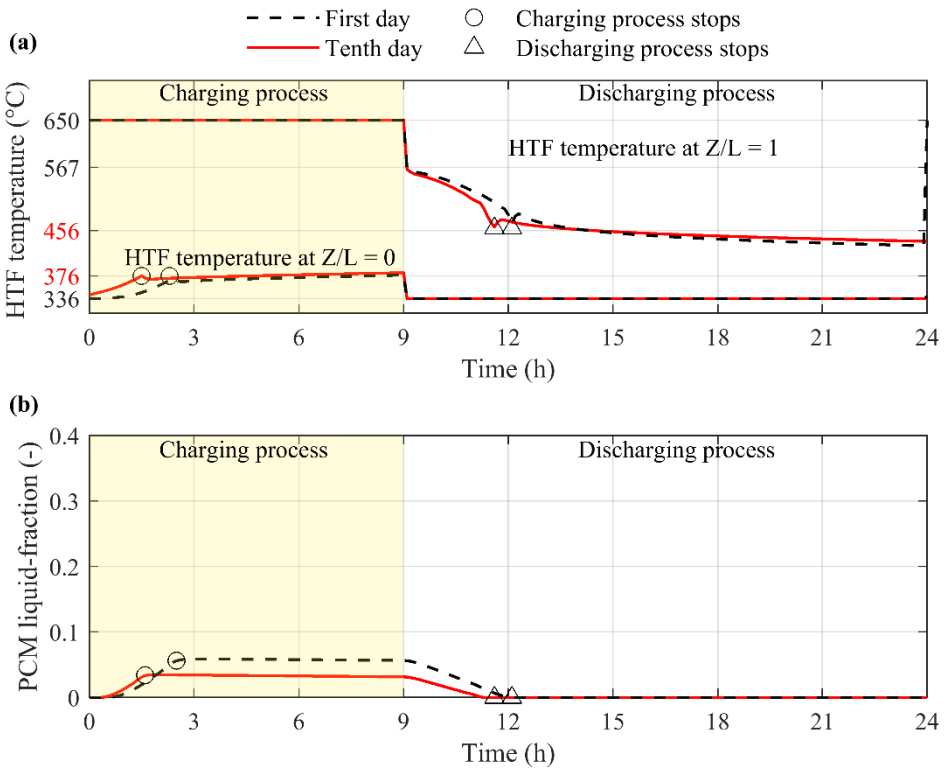

Fig. 3.6 Effect of initial condition on the temporal variation of the a) average HTF temperature and b) average PCM liquid-fraction

Thus, the total stored energy (Q), specific energy (ε), and storage effectiveness (SE) also decrease from 12.97 MJ (12.7% latent and 87.3% sensible) to 7.93 MJ (11.6% latent and 88.4% sensible), 0.25 MJ/kg to 0.15 MJ/kg and 0.24 to 0.21, respectively from day one to day ten. These reductions in Q, ε, and SE show that the system's performance would be overpredicted if the system was only simulated for one day. Therefore, it becomes necessary to study the system for larger time periods such that the initial system conditions do not bias the performance predictions.

This section demonstrated that it is crucial to study the performance of the LHTES system under real-world operating conditions (i.e., periodic steady-state with charging and discharging cutoffs); otherwise, the performance predictions can be severely biased. Thus, this investigation incorporated the above-mentioned boundary conditions in the parametric analysis of the LHTES system (discussed in *Chapter 4* and *Chapter 5*), in which the HTF's flow velocity and the system's geometrical parameters were varied to study their effects on the system's performance

3.3 Design optimization procedure using RSM.

The response surface methodology (RSM) technique [109–111] was adopted in the present investigation to improve the design's performance. The RSM technique establishes a mathematical relation between the design parameters of the LHTES system, for example, L, R, r_o, u_m, and an output parameter ($\overline{D}$). *Eq. 3.10* shows a generalized second-order polynomial equation with model fitting:

$$\overline{D} = a_o + \sum_{j=1}^{n} a_j x_j + \sum_{j<1}^{n} \sum_{l=1}^{n} a_{jl} x_j x_l + \sum_{j=1}^{n} a_{jj} x_j^{\,2} \qquad \textit{Eq. 3.10}$$

where, a_o, a_j, a_{jl}, and a_{jj} are regression coefficients for the intercept, linear, interaction, and quadratic terms, respectively, and x_1, x_2, x_3,….., x_n are the coded value of the input variables, respectively (details are given in ref [110]). In the present study, the RSM technique was implemented using the following steps explained in detail as follows:

Steps: 1 Define

Since the objective is to design systems that meet multiple design objectives, a single response variable "$\overline{D}$" [110], is defined.

Step: 2 Design

After defining the input variables (for example, L, R, r_o, and u_m) and response ($\overline{D}$), the CCD experimental design was chosen to study the effect of input variables on the response and develop the RSM in the form of *Eq. 3.10*.

Step: 3 Run experiments

The cases (defined using CCD experimental design) were simulations in this step, and multi-objective response variable D was calculated for TES systems.

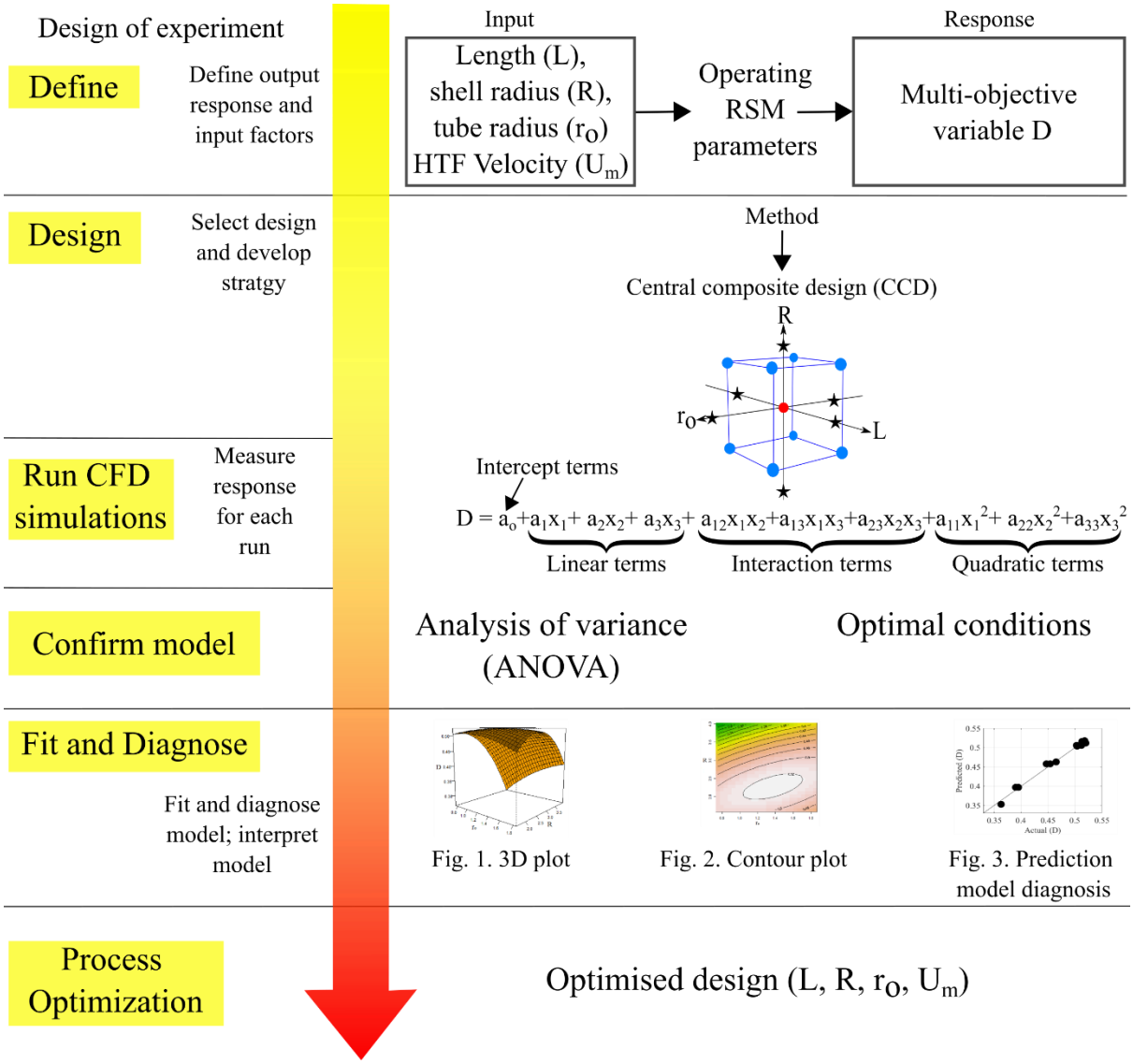

Fig. 3.7 Steps for response surface methodology

Step: 4 Confirm model

All the input factors and multi-objective response variable $\overline{D}$ are used to establish regression models. The best-fitting regression model (with linear, two-way interaction, and pure quadratic terms) was selected from possible combinations based on superior adjusted R^2 value and the analysis of variance (ANOVA). In the test, Pr(>|t|) and Pr(>F) represents the p-value associated with the t-value and the F-value, respectively, where if the p-value < 0.05 for any term, means that the term is significant in the model [112].

The eigenvalue analysis tells the details about the stationary point obtained from the fitted model and the shape of the response surface [110,111]. In particular, when all eigenvalues are negative, the stationary point is present at the coordinate where the maximum value of the response $\overline{D}$ is found. Similarly, the stationary points are at a minimum of $\overline{D}$ if all eigenvalues are positive. Whereas, if eigenvalues are of varied nature or zero, the stationary point is located on a saddle or ridge type of surface, respectively.

Step:5 Fit and diagnose

In this step, the model's fitness is diagnosed using the prediction model diagnosis graph, contour plot, and response surface plot. The prediction model diagnosis graph compares the relationship between the response found using simulation with the predicted response, whereas the contour and response surface plot help to understand the response nature with respect to the significant independent variables. These plots also suggest the direction for further exploration if the optimized design result is distant.

Step:6 Process Optimization

As the objective is to maximize the response variable, the direction of further exploration is decided where the steepest ascent path is followed in the case of first-order models; otherwise, the canonical path is followed for second-order models. The next phase of RSM is planned after the suggested paths are analyzed, and the possible optimal design conditions for the input variables are considered.

Thus, the above steps were followed to find the optimal design of the LHTES system that suits the requirement respective CSP plant.

3.4 Summary

This chapter discusses the details of the LHTES system's description, mathematical model (governing equations, boundary conditions, model validation, grid, and time independence test), and design optimization methodology. As a part of the operational strategies, the boundary conditions also included cutoff temperature and the cyclic steady state, which helped the simulation to mimic the realistic operating conditions of the TES system. To illustrate the effect of realistic boundary conditions (with

and without cutoff temperature as well as with and without cyclic steady state), simulations were set up. The results (after simulating the cases) found that with the incorporation of cutoff temperatures, the system's specific energy and storage effectiveness decreased by 74% and 68%, respectively, due to lower useful charging and discharging times. Similarly, investigation shows that incorporating a cyclic steady-state operational strategy decreased the system's specific energy and storage effectiveness by 40% and 12.5%. Thus, the same operational strategies will be used in *Chapter 4* and *Chapter 5*.

Chapter 4 Parametric analysis of a latent heat thermal energy storage for a CSP plant under realistic operating conditions[2]

In this chapter, the numerical investigation examined the effects of the LHTES system's design parameters on its performance under periodic steady-state with charging and discharging 'cutoff' temperatures to mimic its real-world operation.

4.1 System description and methodology

A 2D axisymmetric unit cell model of the LHTES system (with length L, shell radius R, and tube radius r_o and HTF's flow velocity u_m, see *Fig. 3.2c*) is used in the present study. To simplify the model, PCM and HTF zones were considered, whereas the tube thickness was ignored. By varying the HTF's flow velocity (u_m) and the geometric parameters (R, r_o, L) of the LHTES system, the present study examined their effects on the LHTES system's performance under the operational strategy, as discussed in *Section 3.2.3*.

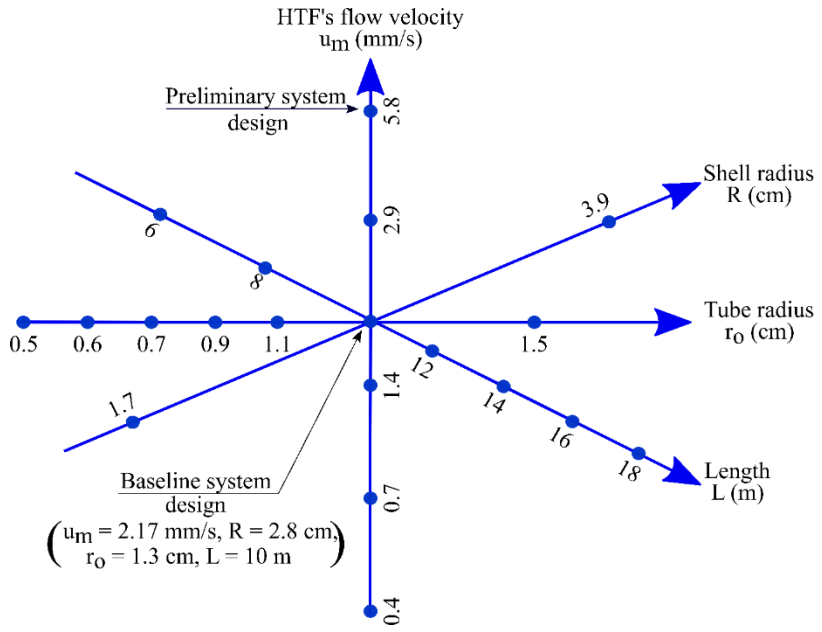

Fig. 4.1 The design parameters investigated for the LHTES system

[2] This study has been published
Vivek Tiwari, Aakash C. Rai, P. Srinivasan, Parametric analysis and optimization of a latent heat thermal energy storage system for concentrated solar power plants under realistic operating conditions, Renewable Energy, Volume 174, 2021, Pages 305-319, ISSN 0960-1481, https://doi.org/10.1016/j.renene.2021.04.073.

4.2 Results and discussion

The preliminary system design was taken from the recommended design (R = 2.8 cm, r_o = 1.3 cm, L = 10 m, and u_m = 5.8 mm/s) of Tehrani et al. [99]. However, with this design, the useful charging and discharging time (1.6 hours and 2.6 hours, respectively) were found to be inadequate for efficient system operation (see *Section 3.2.7*) due to the incorporation of the cutoff temperatures. As a consequence, the HTF's flow velocity was reduced to 2.17 mm/s, which will be discussed in *Section 4.2.1*. This new condition was taken as the baseline system design for further investigations, as shown in *Fig. 4.1*. The effects of the system's geometrical parameters on its performance were then evaluated by varying one parameter at a time and keeping all the others constant (see *Sections 4.2.1–4*). Furthermore, an optimization study was conducted to improve the system's performance, as discussed in *Section 4.2.5*.

4.2.1 Effect of HTF's velocity (u_m)

This investigation studied the effect of HTF's flow velocity (u_m) on the performance of the LHTES system by comparing six cases with different velocities. The geometrical parameters were kept identical in all those cases, which were those of the preliminary design (L = 10 m, R = 2.8 cm, and r_o = 1.3 cm), as shown in *Fig. 4.1*. A range of velocities was investigated by halving the Reynolds number (Re) in each step, starting from Re = 80 (u_m = 5.8 mm/s) of the preliminary system design to Re = 5 (u_m = 0.4 mm/s). This reduction in Re was necessary to increase the useful charging and discharging hours of the preliminary LHTES system design. An additional case was studied with Re = 30 (u_m = 2.17 mm/s) to capture the velocity that maximized the system's performance.

Fig. 4.2a compares the temporal variations of HTF temperatures at the Z/L = 1 and Z/L = 0 during the charging and discharging processes for a range of HTF flow velocities. For a better illustration, only four velocities are shown in this figure. As evident from *Fig. 4.2a*, when the HTF's flow velocity decreased from 5.8 mm/s to ≤ 1.4 mm/s, the useful charging time of the system increased from 1.6 hours to full 9 hours. This change happened because the HTF temperature at the system outlet (Z/L = 0 during charging) increased slowly over time at low flow velocities; thus, it will reach the

charging cutoff temperature at a later time. A similar occurrence occurred during the discharging process, i.e., when the HTF's flow velocity decreased, the useful discharging hours increased from only 2.6 hours to full 15 hours.

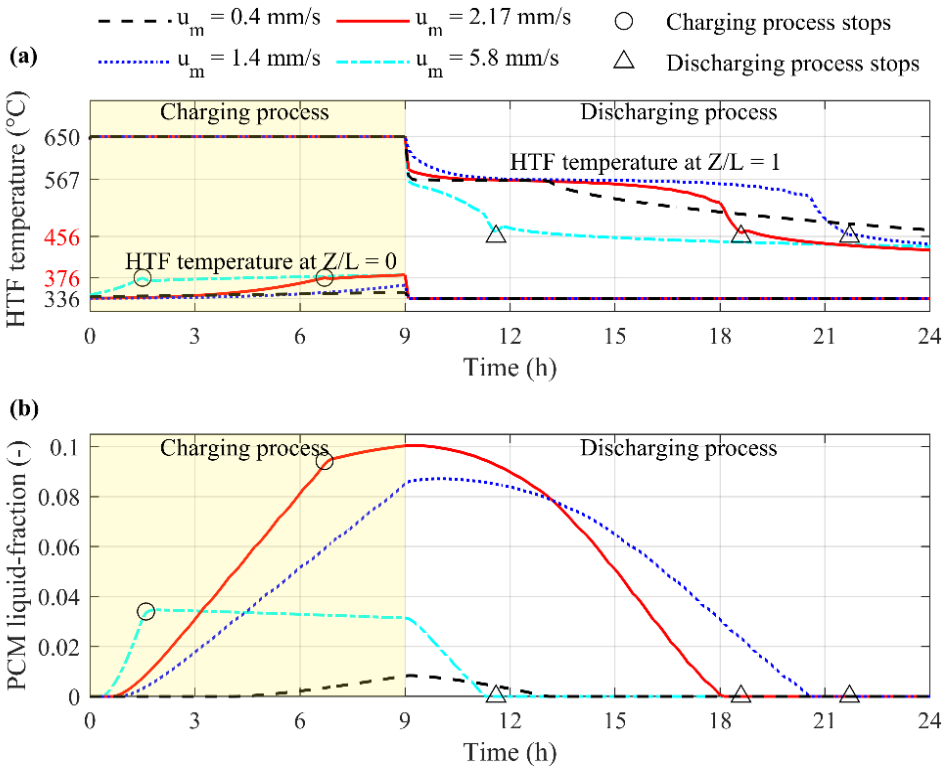

Fig. 4.2 Effect of HTF's velocity on the temporal variation of the a) average HTF temperature and b) average PCM liquid-fraction

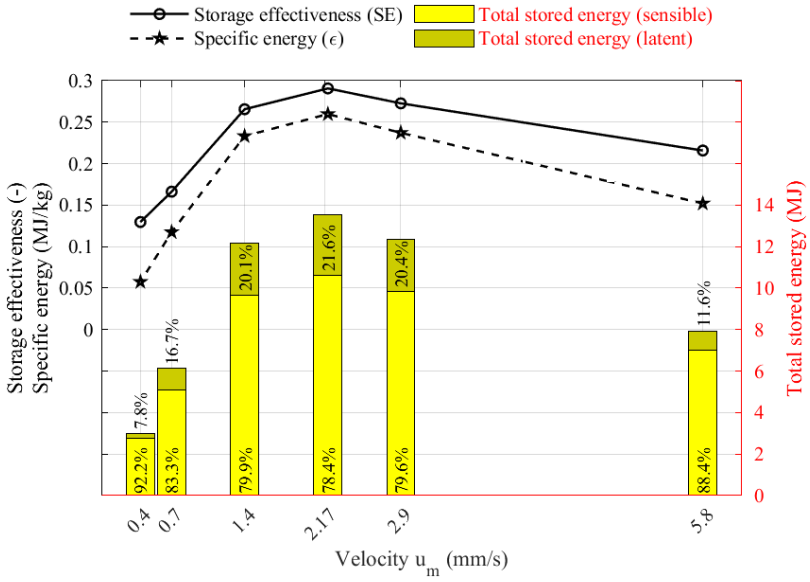

Fig. 4.3 Effect of HTF's velocity on the LHTES system's performance

Note that as the HTF's velocity was reduced from 5.8 mm/s to 2.17 mm/s, the maximum liquid-fraction of the PCM also increased due to an increase in the useful charging hours, as depicted in *Fig. 4.2b*. This phenomenon also led to an increase in the total stored energy (Q), specific energy (ε), and storage effectiveness (SE) of the LHTES system, as shown in *Fig. 4.3*. In addition, a further reduction in the HTF's velocity, from 2.17 mm/s to 0.4 mm/s, led to a decrease in the maximum liquid-fraction of the PCM (see *Fig. 4.2b*), since the heat transfer between the HTF and PCM diminished at very low velocities. However, the useful charging hours remain almost constant (9 h). Consequently, the Q, ε, and SE of the LHTES system also reduced, as shown in *Fig. 4.3*. Thus, the maximum value for the Q, ε, and SE of the system occurred at u_m = 2.17 mm/s since this velocity was neither too high to reduce the useful charging time considerably, nor too low to adversely affect the heat transfer from the HTF to the PCM. Thus, the performance of the system was the best at this velocity (u_m = 2.17 mm/s), and this condition was called the baseline design (L = 10 m, R = 2.8 cm, r_o = 1.3 cm, u_m = 2.17 mm/s), as shown in *Fig. 4.1*. The baseline design's geometrical parameters (R, r_o, and L) was varied one at a time to study their effects on the LHTES system's performance, as discussed in the following sub-sections.

4.2.2 Effect of shell radius (R)

This investigation studied the effect of shell radius (R) on the performance of the LHTES system by simulating two additional cases with shell radii equal to 1.7 cm (R/r_o = 1.3) and 3.9 cm (R/r_o = 3) and, thereby, compared their performance with the baseline system design (R = 2.8 cm ⇒ R/r_o = 2.15). The additional values of shell radii were based on the recommendations of Tehrani et al. [26] and Bellecci et al. [54,55].

Fig. 4.4 shows the variations in HTF temperatures at Z/L = 1 and Z/L = 0 with time for LHTES systems having different shell radii during the charging and discharging processes. The useful charging time of the system increased from only 2.3 hours to full 9 hours as the shell radius increased from 1.7 cm to 3.9 cm. A similar phenomenon occurred during the discharging process, in which useful discharging hours increased (from 3.2 hours to 13.7 hours) with an increase in the shell radius.

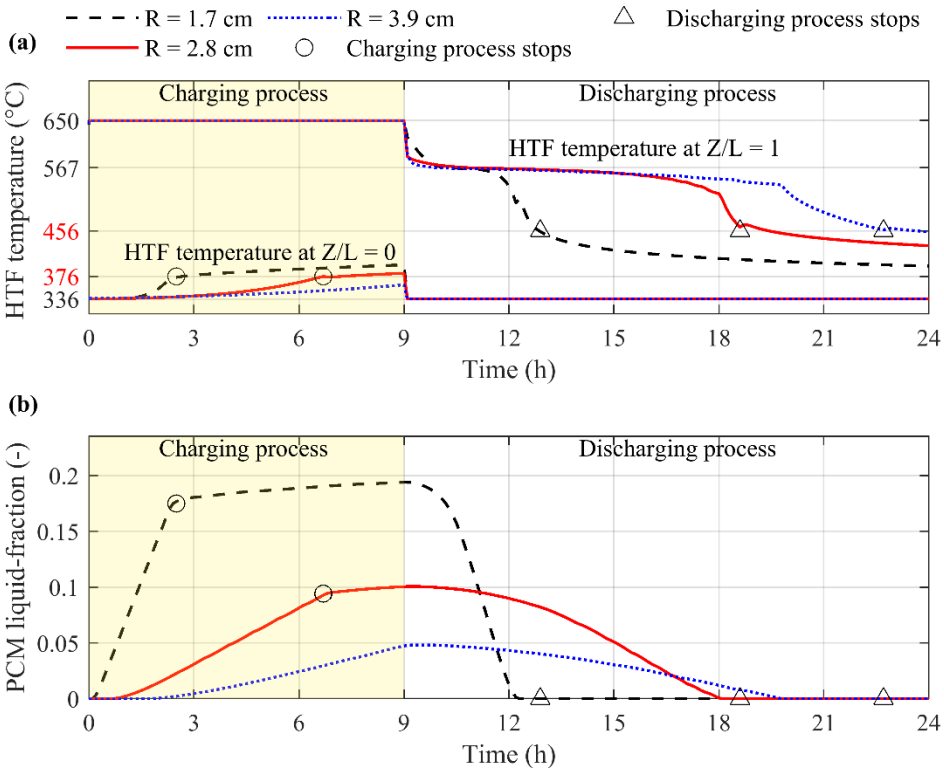

Fig. 4.4 Effect of shell radius on the temporal variation of the a) average HTF temperature and b) average PCM liquid-fraction

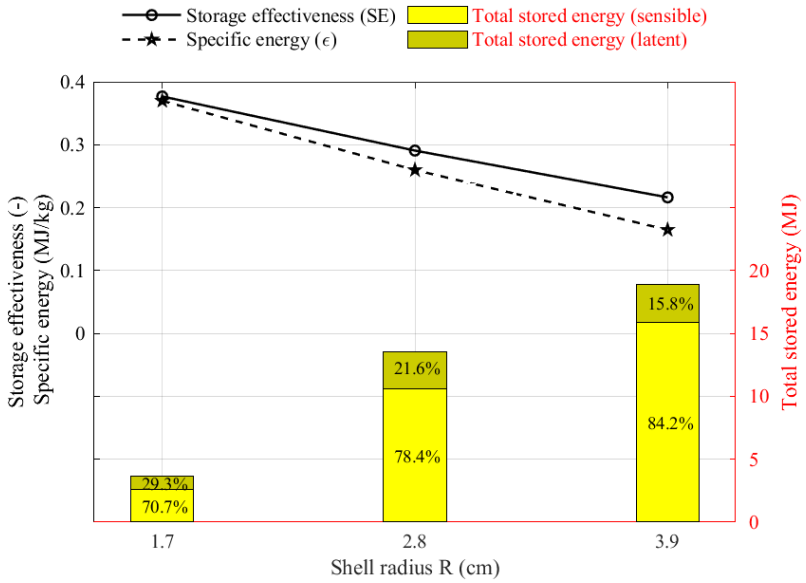

Fig. 4.5 Effect of shell radius on the LHTES system's performance

Although the useful charging and discharging hours increased with shell radius, the maximum liquid-fraction of the PCM was reduced (refer *Fig. 4.4*), since more PCM was available for energy storage in those designs with larger shell radii. Similar to the maximum liquid-fraction, SE and ε also

reduced with an increase in the shell radius, as shown in *Fig. 4.5*. However, by varying the shell radius (small to large), the total energy stored increased, where more useful charging time and PCM mass were available at a larger radius, as shown in *Fig. 4.5*.

4.2.3 Effect of tube radius (r_o)

The effect of tube radius (r_o) was next explored the performance of the LHTES system by comparing seven cases (r_o = 0.5 cm, 0.6 cm, 0.7 cm, 0.9 cm, 1.1 cm, 1.3 cm, and 1.5 cm) with different tube radii ranging from 0.5 cm (R/r_o = 5.6) to 1.5 cm (R/r_o = 1.8), as shown in *Fig. 4.1*.

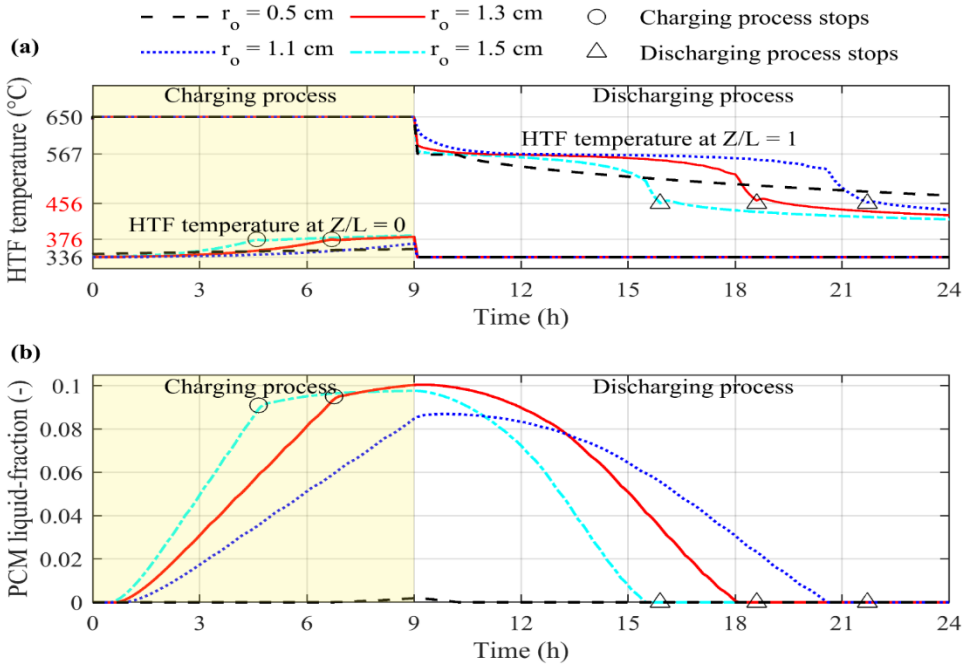

Fig. 4.6 Effect of tube radius on the temporal variation of the a) average HTF temperature and b) average PCM liquid-fraction

Fig. 4.6a compares the temporal variations of HTF temperatures at *Z/L* = 1 and *Z/L* = 0 for a range of tube radii (r_o) during the charging and discharging process. Note that only four representative values of tube radii are shown in *Fig. 4.6*. This figure shows that the useful charging hours initially remain constant (full 9 hours) as r_o increased from 0.5 cm to 1.1 cm, and then decrease from 9 hours to 4.6 hours on further increase in r_o. This phenomenon happens because an increase in the tube radius increases the HTF flow and reduces the PCM mass (since the shell radius is constant) at the same time. In other words, at higher tube radii, the HTF carries more thermal energy, whereas the PCM is

insufficient for storing this excess energy, thus leading to reduces charging hours. Similarly, during the discharging process, as r_o increased from 0.5 cm to 1.5 cm, the useful discharging hours also decreased from the full 15 hours (at r_o = 0.5 cm – 0.6 cm) to only 6.9 hours (at r_o = 1.5).

Fig. 4.6b shows that the maximum liquid-fraction of the PCM increased as the tube radius increased from 0.5 cm to 1.3 cm since the useful charging time was roughly constant, whereas the HTF flow increased and the PCM mass reduced. This phenomenon also led to higher values of Q, ε, and SE, as shown in *Fig. 4.7*. However, a further increase in the tube radius (from 1.3 cm to 1.5 cm) led to a slight reduction in the maximum liquid-fraction due to a decrease in the useful charging hours (from 6.7 h to 4.6 h), which also reduced the Q, ε, and SE values.

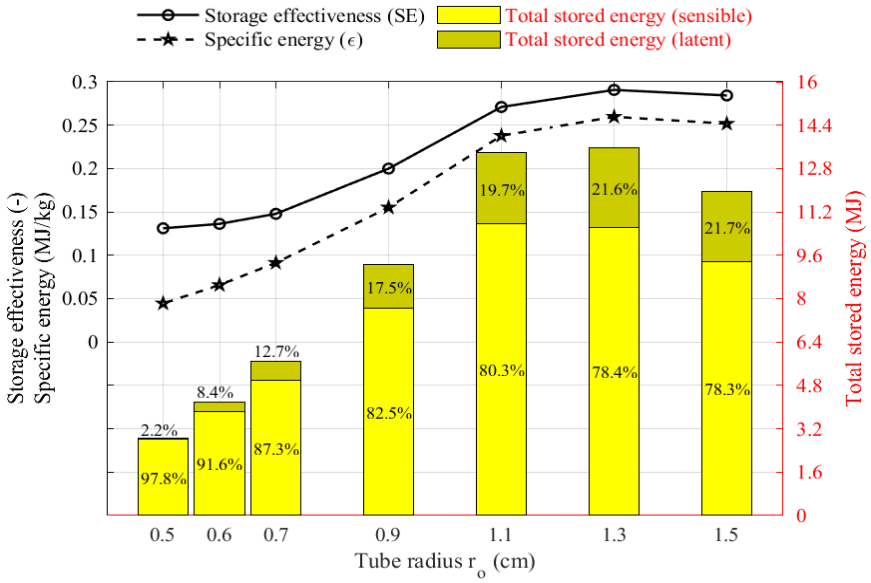

Fig. 4.7 Effect of tube radius on the LHTES system's performance

4.2.4 Effect of length (L)

Finally, the effect of the tube's length (L) was studied on the performance of the LHTES system by comparing seven cases with lengths ranging from 6 m to 18 m, at an interval of 2 m between them. The temporal variations of HTF temperatures were compared at Z/L = 1 and Z/L = 0 for four different lengths (L) during the charging and discharging processes, as shown in *Fig. 4.8a*. This figure shows that the useful charging hours of the system increased from only 2.3 hours at L = 6 m to full 9 hours at $L \geq 14$ m. Similarly, the useful discharging hours increased from 3.8 hours to 12.9 hours, with an increase in

the length. The charging and discharging hours increased with length because of an increase in the mass of PCM. Similarly, the maximum liquid-fraction of the PCM also increased as the length was increased from 6 m to 12 m, as shown in *Fig. 4.8b*, due to an increase in the useful charging hours.

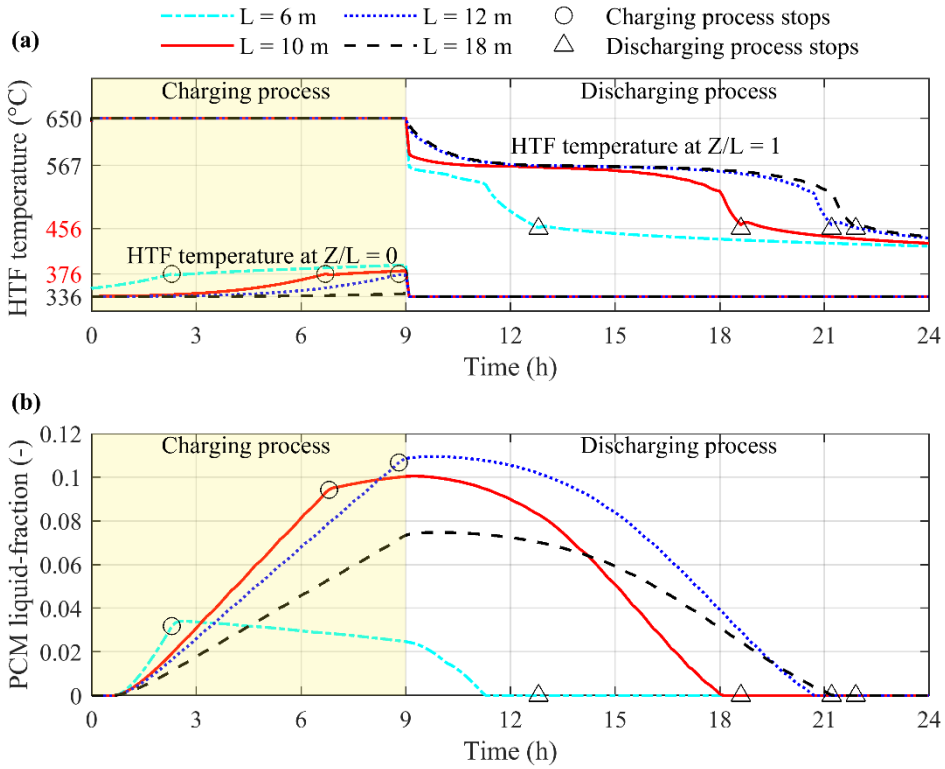

Fig. 4.8 Effect of length on the temporal variation of the a) average HTF temperature and b) average PCM liquid-fraction

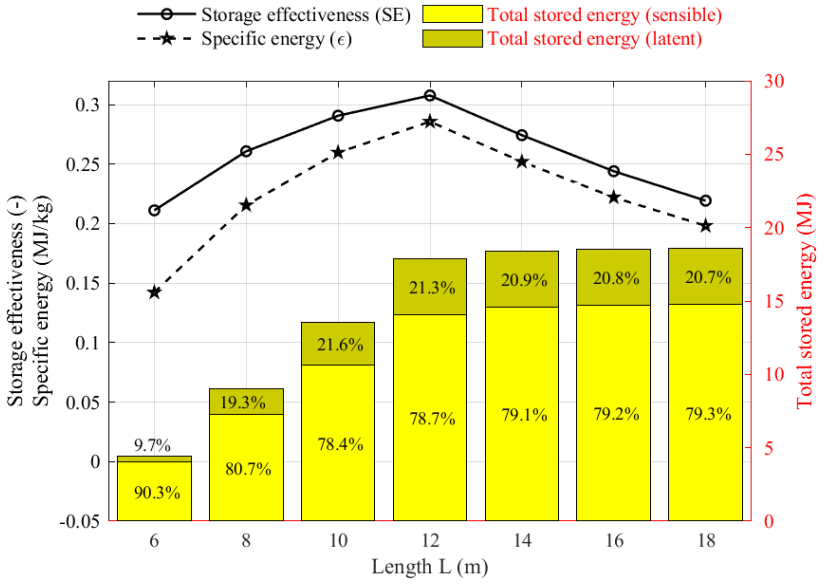

Fig. 4.9 Effect of length on the LHTES system's performance

This change also led to an increase in Q, ε, and SE values, as shown in *Fig. 4.9*. On further increase in the length, the maximum liquid-fraction, ε, and SE decreased, whereas Q remained about the same. This happened because of that the LHTES system becomes very long, and a large amount of PCM is available for energy storage, out of which, a substantial portion remains unutilized.

4.2.5 Design optimization

To optimize the LHTES system's design (u_m, r_o, R, and L were the design variables); this investigation used the response surface methodology (RSM). The objective was to maximize the product of storage effectiveness and charging time ($D = SE \times t_c$) since a good design should have high SE (higher SE means better PCM utilization) and t_c (higher t_c means better utilization of sunny hours). A detailed description of the RSM is given in *Appendix A*, and the final results are discussed below.

Table 4.1 shows the top five design choices obtained from the optimization study (with the highest D values) along with the previous best case taken from the parametric study discussed above (*Section 4.2.1-4*). Clearly, the optimization process significantly improved the D value (by 31–36%), although all the designs could be charged for almost full nine hours, as shown in *Table 4.1*. Thus, improvements in D values were predominantly due to an increase in the SE (SE increased by 29–33%), indicating that the new design choices better utilized the PCM for energy storage than the previous best design. This also led to higher specific energy values (ε increased by 38–43%) in the new choices. However, the total energy stored was much lower in the new design choices since the PCM mass was significantly reduced in those designs (69.0–78.6% lower PCM mass), which also led to slightly lower discharging times.

It was also found that new design choices could supply higher HTF temperatures during the discharging process (leads to higher power cycle efficiency), and lower HTF temperatures (leads to higher receiver efficiency) during the charging process, as compared to the previous best design, as shown in *Fig. A- 5* (see *Appendix A*) for choice # 1. In *Table 4.1*, other design choices also had similar charging and discharging cycles as choice # 1 and were not shown in *Fig. A- 5*. Thus, the adopted

optimization technique not only significantly improved the LHTES system's performance but would also lead to improvements in the CSP plant efficiency.

Table 4.1 The top five design choices were obtained using the response surface methodology (RSM).

	u_m (mm/s)	r_o (cm)	R (cm)	L (m)	D (h)	t_c (h)	t_d (h)	SE (-)	ε (MJ/kg)	Q (MJ)
Previous best	2.17	1.30	2.80	12.0	2.71	8.8	12.2	0.31	0.29	17.9 (21.3% latent)
Choice # 1	1.04	1.17	1.57	14.8	3.68	9	11.7	0.41	0.42	5.7 (26.7% latent)
Choice # 2	1.32	1.00	1.43	14.6	3.68	8.9	11.5	0.41	0.42	5.5 (25.8% latent)
Choice # 3	1.26	1.14	1.58	16.1	3.64	9	11.7	0.40	0.41	6.7 (26.1% latent)
Choice # 4	0.98	1.17	1.57	14.5	3.60	9	11.7	0.40	0.41	5.5 (26.6% latent)
Choice # 5	1.49	1.10	1.59	17.3	3.56	9	11.8	0.40	0.40	7.8 (25.4% latent)

4.3 Summary

To further investigate the suitability of the AlSi12-based LHTES system, the LHTES system's performance was compared with other TES systems reported by Tehrani et al. [99], who studied a shell-and-tube LHTES system with different energy storage options (SHTES using concrete, LHTES using PCMs, and a hybrid of both) for integration into a CSP plant. They reported that liquid-fractions equal to 0.24 and 0.60 for a single PCM of Li_2CO_3–K_2CO_3 and for hybrid design with H325/H430/H525 PCMs, respectively, when charged for 9 hours without incorporating cutoffs. It was found that the PCM liquid-fractions obtained in our study are slightly lower than those reported in the literature due to the incorporation of cutoff temperatures. The SE values were also lower in our study (SE = 0.40–0.41 for our recommended designs) as compared to those (SE = 0.53–0.61) reported by Tehrani et al. [99]. Similar to the previous study, Liu et al. [103] studied a shell-and-tube LHTES system with different hybrid designs. They reported higher SE values (0.43–0.70) as compared to the current study. Nevertheless, due to the high latent heat capacity of AlSi12, the system has higher specific energy values ($\varepsilon \approx$ 0.40–0.42 MJ/kg) as compared to those (ε = 0.17–0.39 MJ/kg) reported by Liu et al. [103]. This indicates that the AlSi12 system will require the least material for energy storage.

Chapter 5 A multi-objective design optimization of a latent heat thermal energy storage (LHTES) system for CSP plants under realistic operating conditions[3]

A power plant can be classified into two types based on its load handling capacity and duration of power generation, namely: a) peak load power plants and b) baseload power plants. While the peak load power plant generates electricity only during peak demand hours, whereas the baseload power plant generates electricity continuously during the day. Thus, this chapter investigated two use-case scenarios, i.e., the TES system integrated with hybrid PV-CSP [113,114] and baseload CSP plants [115–117].

The hybrid PV-CSP plant configuration is the peak load power plant, in which PV produces electricity during sunny hours, whereas the CSP produces electricity in non-sunny hours of peak load demand. This plant configuration helps balance solar energy production and electricity demand (for details, refer to the "Duck curve" in *Section 1.1*). The other plant configuration is the baseload power plant, which operates round-the-clock to provide continuous minimum power. Each of the plant configurations has different objectives, discussed in the subsequent section. Thus, both LHTES designs were optimized using RSM to meet the goals of each plant configuration.

5.1 System description

As discussed in *Chapter 3*, the thermal energy storage (TES) system was designed to integrate into a next-generation high-temperature solar power tower (SPT) CSP plant of 167 MWe capacity, as shown in *Fig. 5.1*. The CSP plant consists of solar and power blocks. The solar block comprises a central receiver that receives heat energy and transfers it to the power block using HTF. The HTF supplies thermal energy from the solar field to the steam generator at the temperature of 650 °C and exits at a temperature of 336 °C with a mass flow rate of HTF ($\dot{m}_{HTF}$) in the header pipe. The power block gets the heat energy ($P_{steam} = 337\ MW_{th} = P_{ele} \,/\, \eta_{cycle}$) and uses it to convert the water into steam using

[3] The manuscript of this work is under preparation.

a steam generator, and consequently, the generated steam runs the turbine to produce electricity. The surplus energy collected by the solar block during sunny hours is stored in the TES. In order to accomplish the study's objectives, TES systems were integrated into CSP plants to meet peak and baseload electricity demand. LHTES design methodology is applied for two use case configurations: hybrid PV-CSP plant and baseload CSP plant.

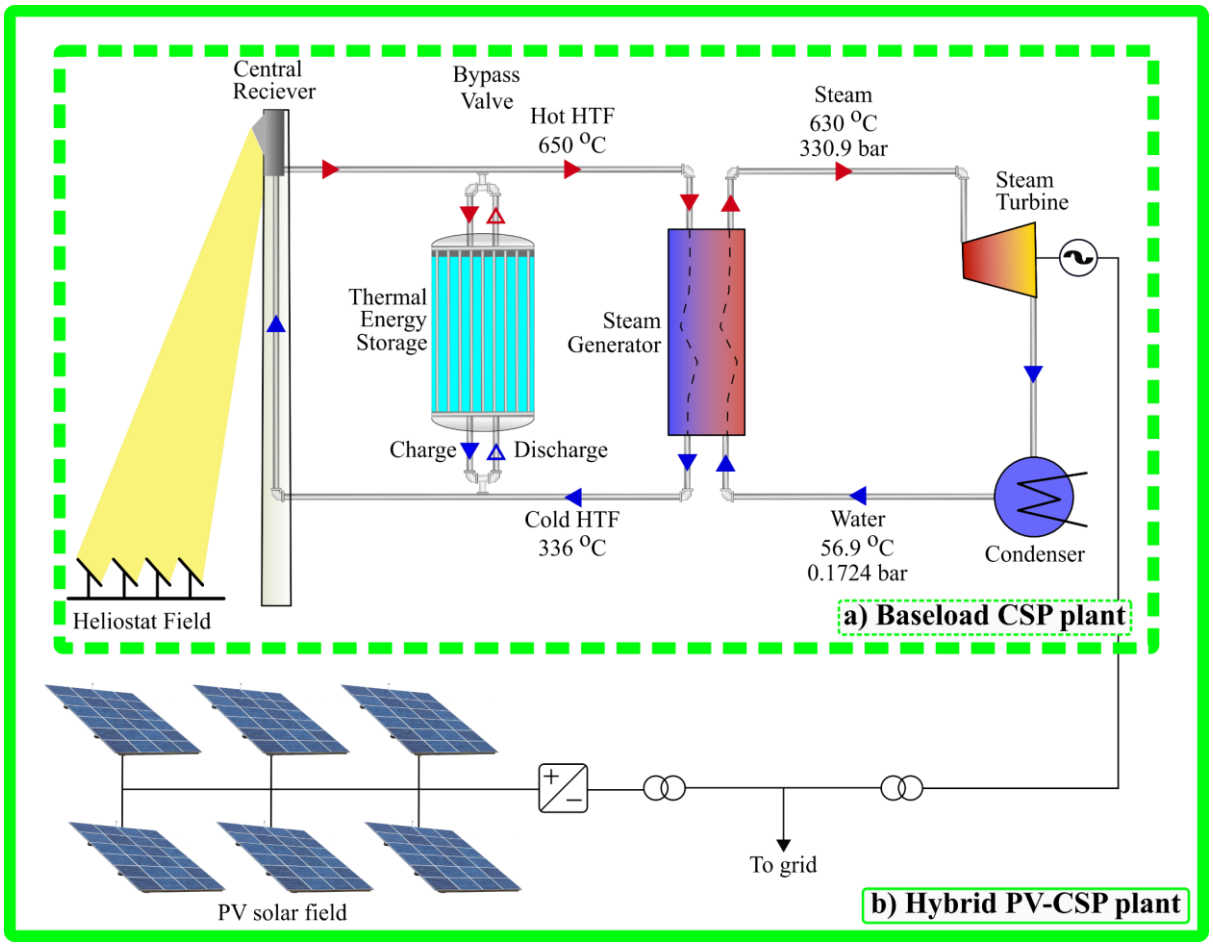

Fig. 5.1 Thermal energy storage integrated into a 167 MWe concentrated solar power plant a) baseload CSP plant (inside the dotted box) and b) Hybrid CSP-PV plant (inside the solid box)

In the hybrid PV-CSP plant (*Fig. 5.1b*), CSP produces electricity during non-sunny and peak load demand hours, whereas PV produces electricity during sunny hours. The combination of PV with the CSP-TES plant can produce electricity at a lower tariff (LCOE) due to PV's cheaper electricity production in the daytime and, subsequently, TES's competitive storage cost compared to expensive thermochemical batteries [118]. In this plant, TES receives thermal energy from the central receiver

through the HTF, gets charged in sunny hours (assumed to be 9 hours), and discharges heat energy to the power block in non-sunny hours. Thus, the design objective is to maximize the usable storage capacity of the hybrid PV-CSP plant while maximizing the discharge time for higher electricity production during non-sunny periods.

In contrast to the hybrid PV-CSP plant configuration, a baseload CSP plant (*Fig. 5.1a*) must operate round-the-clock to provide continuous minimum power. Such a plant requires three solar fields (solar multiplier, SM = 3), where one solar field would run the power block, and the remaining solar fields would supply the energy to the TES during sunny hours (assumed to be 9 hours). As part of the TES system, solar fields charge two identical storage blocks. The TES blocks can then be discharged sequentially during hours of low solar radiation so that the cumulative discharging time is 18 hours (i.e., total non-sunny hours); as a result, the power plant will run 24 hours a day. In this regard, the design objective is to maximize the usable storage capacity and limit the discharge time to 9 hours for each TES block.

5.2 Methodology

As discussed in *Section 3.1*, the LHTES system's performance can be evaluated by analyzing a single unit cell, assuming that the TES system behaves as a composite of several identical unit cells. *Fig. 3.2b* illustrates the general structure of a single unit cell (of length L) consisting of a tube (through which HTF flows, with an inner radius r_i and an outer radius r_o) and its annular region (with a radius R, which contains PCM). It is important to note that the unit cell geometry is axisymmetric. Thus, a two-dimensional axisymmetric geometrical representation (*Fig. 3.2c*) would be sufficient for the CFD simulations of the LHTES system. To examine the unit cell's heat-transfer characteristics, a commercial CFD package (ANSYS FLUENT) was employed to model its charging and discharging behavior. Details about the governing equations, boundary conditions, validation against experimental data, and grid-and-time independence analysis are provided in *Section 3.2*. As discussed in *Chapter 4*, the previous investigation neglected the conduction mode of heat transfer in the tube sandwiched between the HTF and PCM zone. However, in the present study, governing equations are modified to account

for heat transfer through the tube, which is imperative since a significant amount of energy is stored in the tube and HTF material (~ 30%), affecting the system's performance. Thus, the 2D axisymmetric CFD model was simulated using realistic boundary conditions (details in *Section 3.2.7*).

The CFD model discussed above includes the length (L), shell radius (R), and tube radius (r_o) of the system and the mass flow rate of the HTF ($\dot{m}$) as inputs and charging-discharging performance as output. However, $\dot{m}$ depends on the mass flow rate of the HTF in the heater pipe ($\dot{m}_{HTF}$) and the number of unit cells (decided based on SE). Thus, an iterative method is needed to find $\dot{m}$, which is explained in the following sub-section.

5.2.1 An iterative method to find $\dot{m}$

The CFD model simulated the charging-discharging behavior of the unit cell, with its length (L), shell radius (R), tube radius (r_o), and the mass flow rate of the HTF flowing in the cell ($\dot{m}_{unit}$) as inputs. However, note that only the geometric parameters (L, R, and r_o) were the independent variables for the model since $\dot{m}_{unit}$ can be calculated from the system's geometry, material properties, and operation conditions, as explained below.

We calculated $\dot{m}_{unit}$ by using the following equation:

$$\dot{m}_{unit} = \frac{\dot{m}_{total}}{N} \quad \text{(Eq. 5.1)}$$

where $\dot{m}_{total}$ is the total mass flow rate of the HTF ($\dot{m}_{total} = 1358.54\ kg/s$ based on the operating parameters of the CSP) and N the number of unit cells. The above equation assumes that the the HTF flow is equally distributed amongst N unit cells. N was calculated by using:

$$N = \frac{E_d}{E_{unit}} \quad \text{(Eq. 5.2)}$$

where E_d is the required capacity of the LHTES system and E_{unit} the energy stored by a single unit cell. E_d was calculated as 3,033 MWh by multiplying the power input to the LHTES system (337 MW) with the charging hours (9 h), while E_{unit} was obtained from:

$$E_{unit} = SE \times E_{unit,max} \quad \text{(Eq. 5.3)}$$

where SE is the storage effectiveness of the unit cell and $E_{unit,max}$ its maximum storage capacity. $E_{unit,max}$ was obtained by summing the storage capacities of the PCM, the tube material, and the HTF contained in the unit cell, using the following expression:

$$E_{unit,max} = m_{PCM}\, L + m_{PCM} C_{PCM} (T_H - T_L) + m_{tube}\, C_{tube}\, (T_H - T_L) + m_{HTF}\, C_{HTF}\, (T_H - T_L) \quad \text{(Eq. 5.4)}$$

where m_{PCM}, m_{tube}, and m_{HTF} are the mass of the PCM, tube material, and HTF contained in the unit cell, respectively; L the PCM's latent heat capacity; C_{PCM}, C_{tube}, and C_{HTF} the specific heat capacities of the PCM, tube material, and HTF, respectively; and T_H and T_L the highest and lowest temperature encountered by the LHTES system (650 °C and 336 °C). We calculated m_{PCM}, m_{tube}, and m_{HTF} from the unit cell's geometry and the densities of the PCM, tube material, and HTF; thus, $E_{unit,max}$ was obtained from the system's geometry, material properties, and operating temperatures.

By combining Eqs. 5.1–3, we obtain:

$$\dot{m}_{unit} = \frac{\dot{m}_{HTF} \times E_{unit,max} \times SE}{E_d} \quad \text{(Eq. 5.5)}$$

where $\dot{m}_{HTF} = 1{,}358.54$ kg/s, $E_{unit,max}$ = 3,033 MWh, and $E_{unit,max}$ was calculated from Eq. 4. Note that to calculate $\dot{m}_{unit}$ (an input for the CFD simulation) using Eq. 5.5, SE is required, which is a simulation output. Thus, to calculate $\dot{m}_{unit}$, we used an iterative approach, as shown in Fig. 5.2. In this approach, we use a guess value of SE to calculate $\dot{m}_{unit}$. The CFD simulations are then run, and the actual SE of the unit cell is obtained, which is then used to update the value of $\dot{m}_{unit}$ for the next simulation. The process converges when the guessed SE value equals that obtained from the CFD simulations. An iteration cycle is shown in *Table 5.1* for the interested reader.

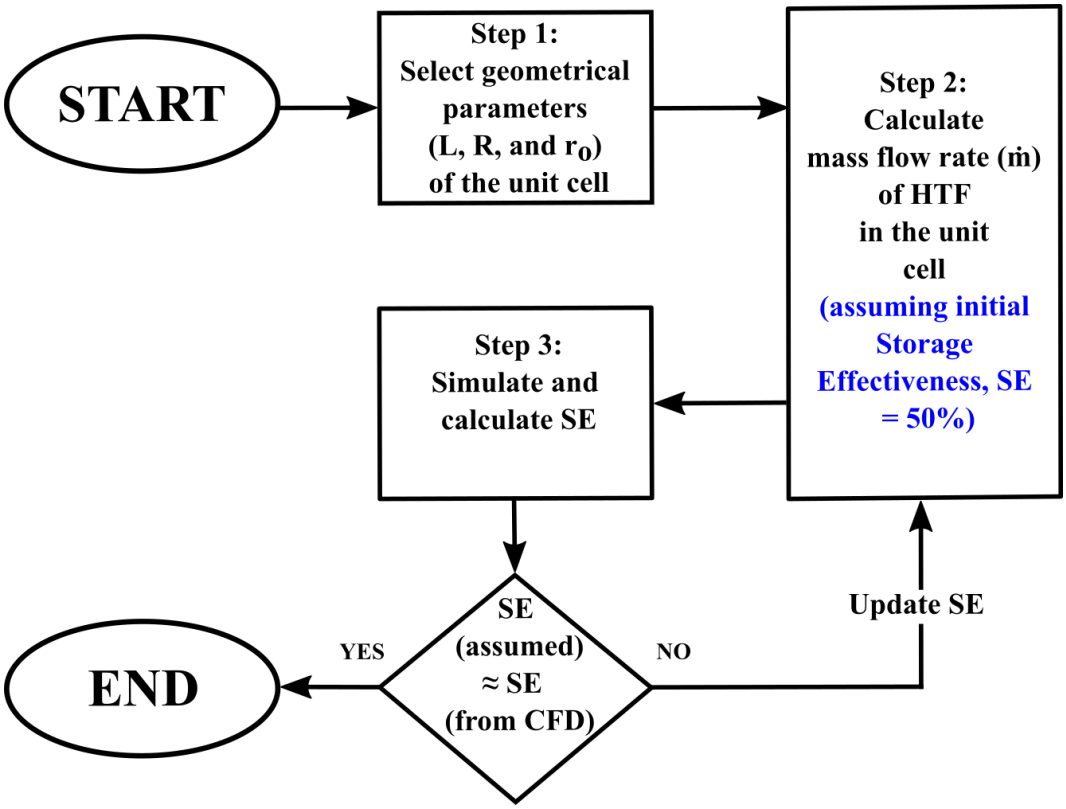

Fig. 5.2 Flow chart to find a unit cell's mass flow rate (ṁ)

Table 5.1. Example to find the mass flow rate of HTF in a unit cell

Case	L	r_o	R	Assumed SE	$\dot{m}_{HTF}$	N_p	$\dot{m}$	Actual SE	t_c	t_d	Q
	(m)	*(cm)*	*(cm)*	*(-)*	*(kg/s)*	*(-)*	*(kg/s)*	*(-)*	(h)	(h)	*(MWh)*
A	50	1.3	2.8	0.50	1358.54	138,558	0.018	0.27	5	7.5	1652.2
B	50	1.3	2.8	0.34	1358.54	120,026	0.012	0.31	8.4	11.8	2790.9
C	50	1.3	2.8	0.33	1358.54	117,927	0.012	0.33	8.9	12.4	2953.1

A design with t_d and Q of 12.4 h and 2953.1 MWh, respectively, were achieved following this approach, which will serve as the baseline design for further optimization, discussed in the following section.

5.2.2 Design optimization

The response surface methodology (RSM) technique was adopted to improve the LHTES system's design. The technique models the system's response as a linear or quadratic function of the design

parameters (L, R, and r_o in the present study) and obtains the optimum value of the response. The CCD experimental design was used to study the effect of input variables on the response and develop the RSM. The CCD design (see *Fig. 5.3*) is used to build the model for the response variables, where several designs are shown in a design space. In order to employ the RSM technique, a design space is needed for the investigation. More details of the technique can be obtained from the study by Myers [110].

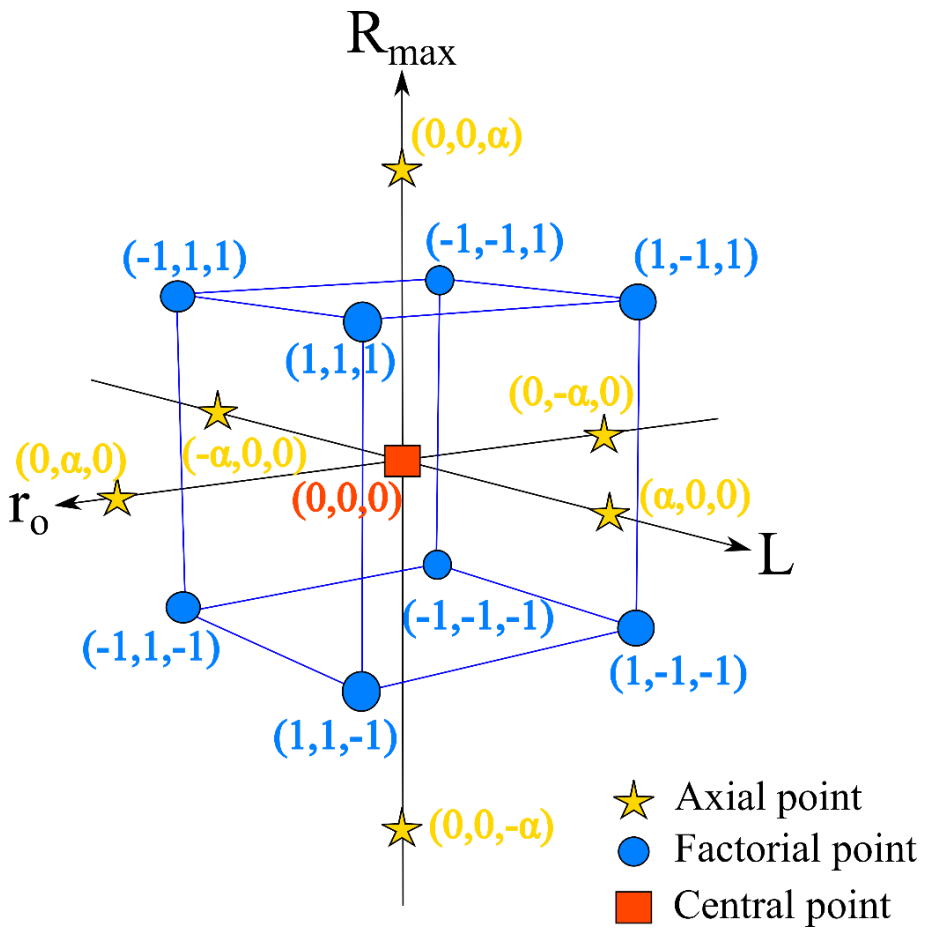

Fig. 5.3 Schematic of the central composite design (CCD) used to build the model

Two use-case scenarios were demonstrated for the LHTES system: (a) a hybrid PV-CSP and (b) a baseload CSP. For the hybrid PV-CSP system, the objective was to maximize the t_d and SE, while for the baseload CSP, the aim was to maximize SE and obtain t_d equal to 9 h. Since it was needed to meet multiple design objectives for each use case, the desirability variable D [110] is defined as the geometric mean of d_1 and d_2:

a) Since the objective for both hybrid PV-CSP and baseload CSP plants is to have high storage

effectiveness, the variable is normalized as:

$$d_1 = \frac{SE - \mathrm{SE}_{min}}{\mathrm{SE}_{\max} - \mathrm{SE}_{min}} \qquad \textit{Eq. 5.1}$$

here, the minimum SE is zero, i.e., energy stored in the unit cell is zero, and the maximum SE is one, i.e., energy stored is equal to the storage capacity of the unit cell.

a) In the case of the discharge time (t_d), the normalization procedures were different for both plant configurations since the aim in a PV-CSP plant is to maximize t_d, while the aim in baseload CSP plants is to achieve a target value (9 hours) of t_d. The appropriate normalization functions for the PV-CSP plant and baseload plant, respectively, are as follows:

$$d_2 = \frac{t_d - t_{min}}{t_{\max} - t_{min}} \qquad \textit{Eq. 5.2}$$

$$d_2 = \begin{cases} 0, & If\ t_d = t_{min} \quad \textit{Eq. 5.3a} \\ \dfrac{t_d - t_{min}}{t_{target} - t_{min}}, & If\ t_{min} < t_d \leq t_{target} \quad \textit{Eq. 5.5b} \\ \dfrac{t_{max} - t_d}{t_{max} - t_{target}}, & If\ t_{target} \leq t_d < t_{max} \quad \textit{Eq. 5.5c} \\ 0, & If\ t_d \geq t_{max} \quad \textit{Eq. 5.5d} \end{cases}$$

where the minimum t_d is zero, i.e., the HTF temperature is equal to the charging cutoff temperature at the outlet of LHTES, and the velocity of HTF is set to zero, whereas the maximum t_d is 15 h, i.e., the temperature of the HTF never reaches the cutoff temperature of the LHTES during the charging operation.

The design cycle was started with a baseline LHTES design (L = 50 m, r_i = 1.2 cm, r_o = 1.3 cm, R = 2.8 cm, and N_p =117,927) that was obtained from the eNTU approach (explained in *Appendix B*).

The feasible design space for the RSM ranged from L ϵ [29-71], L/r_o ϵ [2229-6637], and R/r_o ϵ [1.11-7.45] as recommended in the literature [26,54,55].

5.3 Results and Discussion

The CFD results showed that the baseline design could store 2953.1MWh of energy, which is slightly lower than the desired capacity (3033 MWh). The charging time (t_c), discharging time (t_d), and storage effectiveness (SE) were 8.9 h, 12.4 h, and 0.32, respectively. The same baseline was used for both plant configurations (hybrid PV-CSP and baseload CSP) since the eNTU method used to generate the baseline design does not discriminate between the different use cases. Since the baseline design was identical, the initial design space remained the same. The following sub-sections (*Section 5.3.1* and *Section 5.3.2*) discuss the optimization results along with the geometry and performance of LHTES systems for hybrid PV-CSP and baseload CSP plants, respectively.

5.3.1 Hybrid PV-CSP plant

Eq. 5.4 shows the mathematical relation for the response surface between the multi-objective response variable ($\bar{D}$) for the PV-CSP plant and the LHTES system's geometrical parameters (r_o is the tube radius, and R is the shell radius). The unit cell's length (L) does not affect the system's performance, as the CFD results showed little impact on t_d or SE. The model equation successfully predicted the LHTES system's performance ($\overline{D}$) from its geometrical parameters, with the maximum difference between the predicted performance ($\overline{D}$) and desirability (D) obtained from CFD results being 2.6 %, as shown in *Fig. 5.4*.

$$\overline{D} = 0.64 - 0.456r_o + 0.159R + 0.09r_oR + 0.09{r_o}^2 - 0.06R^2 \qquad Eq.\ 5.4$$

The contour and response surface plots described by *Eq. 5.4* are given in *Fig. 5.5*. The optimized design with the maximum predicted value of $\bar{D}$ = 0.524 was found at r_o = 1.37 cm and R = 2.7 cm, as shown in *Fig. 5.5a*. However, when this design was simulated using CFD, the desirability (D) was found to be slightly lower at 0.517. *Table 5.2* shows the performance of the optimized design compared to the baseline design. A slight difference was found in the t_d and SE values of the optimum design as

compared to their baseline values, which led to a minor improvement in D (by ~ 1%). However, the optimum LHTES design's specific energy (ε) was significantly higher than the baseline (by 9%). Furthermore, the energy stored and dispatched (Q) by the optimized design was sufficient to meet the required capacity for the hybrid PV-CSP plant (3033 MWh, as discussed in *Section 5.1*), whereas the baseline design had a slightly lower capacity. Overall, the optimized design has superior performance over the baseline design.

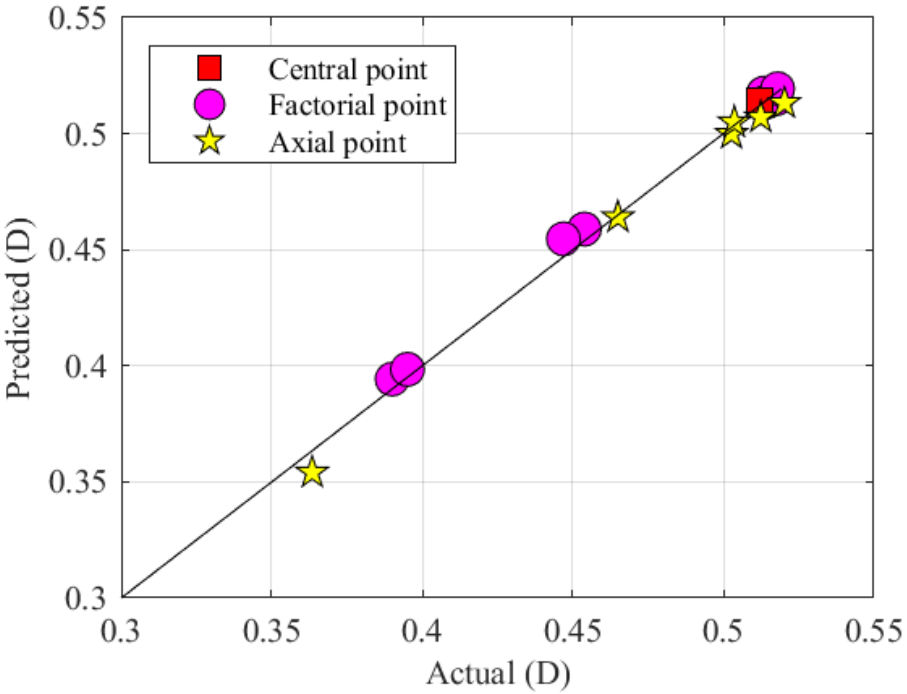

Fig. 5.4 RSM prediction model diagnosis for hybrid CSP-PV plant

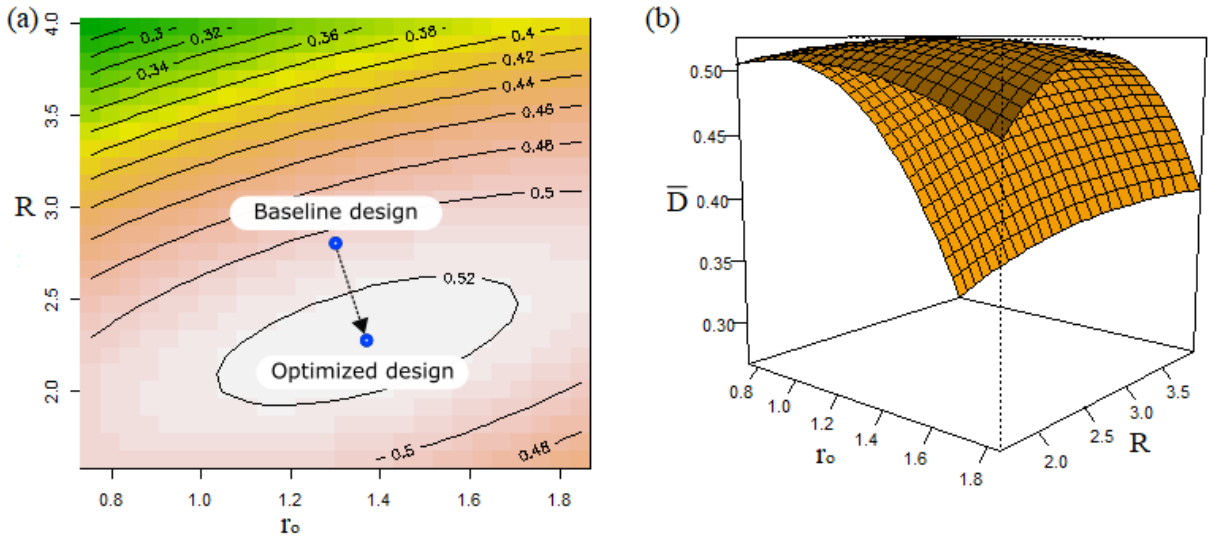

Fig. 5.5 (a) The 2-dimensional contour and (b) the 3-dimensional response surface plots showing the effects of tube radius (r_o) and shell radius (R) on the LHTES system's desirability ($\overline{D}$)

Table 5.2 The performance of the optimized design for the peak load plant (obtained using response RSM) compared with the baseline design

Designs	L (m)	r_o (cm)	R (cm)	N_p (-)	u_m (mm/s)	t_c (h)	t_d (h)	SE (-)	ε (MJ/kg)	Q (MWh)	D (-)
Baseline	50	1.30	2.8	114819	11.86	8.9	12.4	0.32	0.352	2953.1	0.512
Optimized	50	1.37	2.27	202571	6.00	9.0	12.3	0.33	0.384	3034.8	0.517

As the RSM predicted that length does not significantly affect the LHTES system's performance, design alternatives were generated by varying the length of the system (ranging from 37.5 to 62.5 m). The effect of length on the performance of the optimized design was examined by maintaining the dimensions of R and r_o constant throughout. The result shows (details in *Table 5.3*) that the length has an insignificant effect on the performance of the LHTES system for hybrid PV-CSP plants, as the desirability remains nearly unchanged.

Table 5.3 Effect of length on optimized LHTES system's for the peak load power plant model

L (m)	r_o (cm)	R (cm)	N_p (-)	u_m (mm/s)	t_c (h)	t_d (h)	SE (-)	ε (MJ/kg)	Q (MWh)	D (-)
37.5	1.371	2.27	269,989	4.50	9.0	12.2	0.33	0.383	3032.3	0.515
50	1.371	2.27	202,571	5.99	9.0	12.3	0.33	0.384	3035.9	0.517
62.5	1.371	2.27	161,994	7.50	9.0	12.3	0.33	0.384	3034.3	0.517

5.3.2 Baseload CSP plant

The best-fit model for the baseload CSP plant establishes the mathematical relationship between the tube radius (r_o) and the shell radius (R) using a multi-objective response variable ($\bar{D}$), as shown in *Eq. 5.5*. Thus, the model accurately predicted the system's performance with a maximum error of 4% between predicted ($\bar{D}$) and CFD results (D), as shown in *Fig. 5.6*.

$$\bar{D} = 0.56 - 0.03r_o - 0.0149R - 0.05r_oR + 0.057{r_o}^2 + 0.039R^2 \qquad Eq.\ 5.5$$

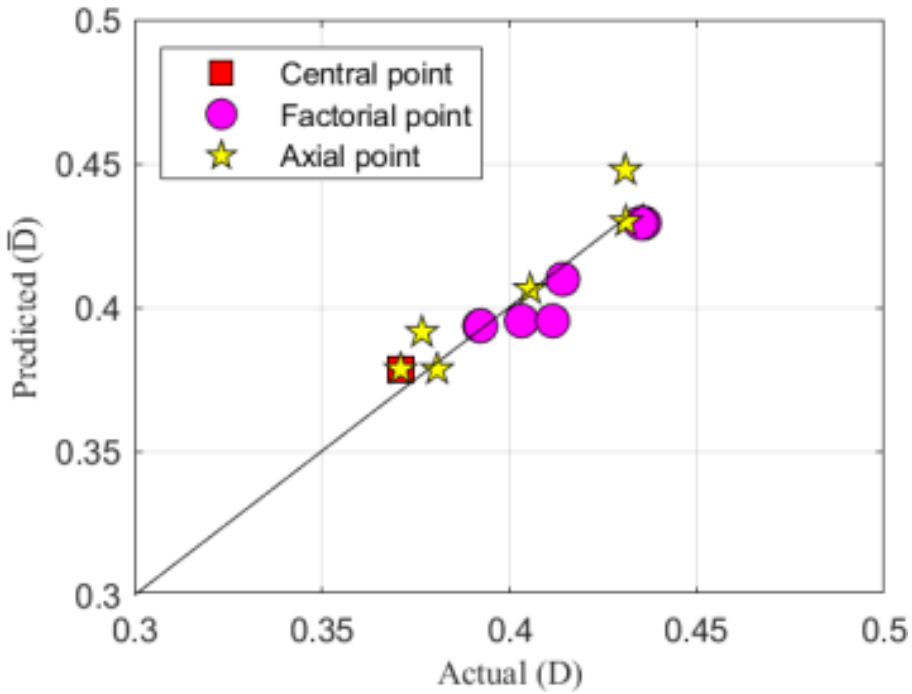

Fig. 5.6 (a) The 2-dimensional contour and (b) the 3-dimensional response surface plots showing the effects of tube radius (r_o) and shell radius (R) on the LHTES system's desirability ($\bar{D}$)

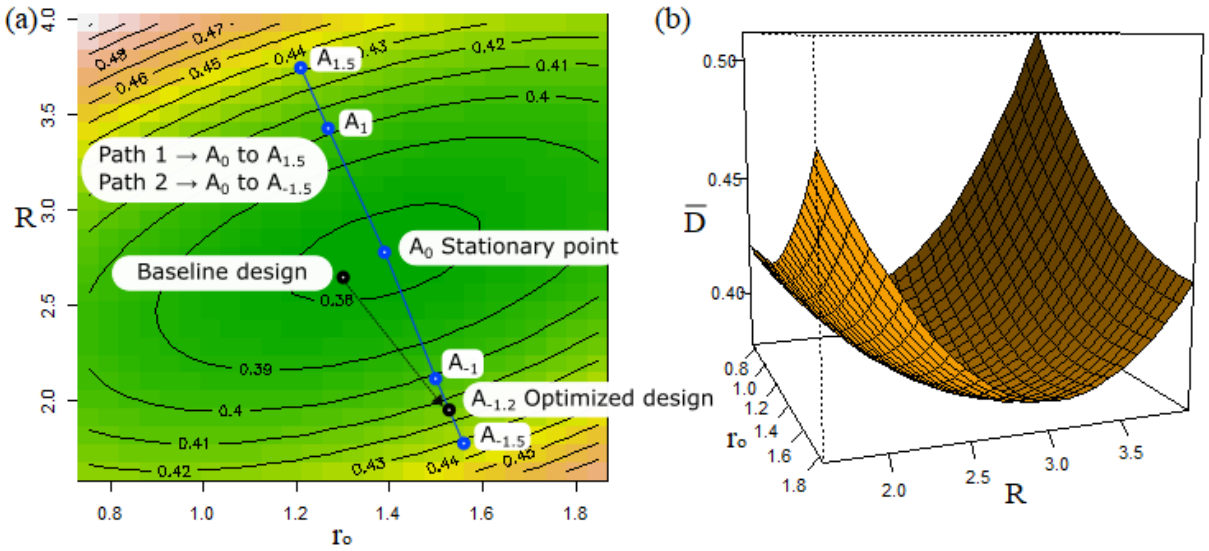

Fig. 5.7 a) The contour plot, and b) The response surface plot of shell radius (R) and tube radius (r_o) with its effects on the response output ($\bar{D}$)

The contour and response surface plots show that the stationary point (at r_o = 1.39 cm and R = 2.77 cm) suggested by RSM is located at the minimum predicted value of $\bar{D}$. However, the goal is to maximize $\bar{D}$, which can be accomplished by further exploring the designs along the two steepest ascent paths (represented by the blue line in *Fig. 5.7a*). Path 1 goes from A_0 to $A_{1.5}$ (see *Fig. 5.7a*), along which R increases while r_o decreases. The designs on this path (see *Table 5.4*) have higher desirability than the baseline design due to favorable discharging characteristics (t_d = 10 h in $A_{1.5}$, against a target of 9 h). However, they have a lower value of SE because the unit cell's PCM mass has increased, and the charging time has decreased. Path 1 was not pursued further due to the design's low SE, which represents underutilized PCMs.

The other steepest ascent path, i.e., path 2, goes from A_0 to $A_{-1.5}$ along which R decreases while r_o increases (see *Fig. 5.7a*). On this route, the desirability (D) increased (see *Table 5.4*) due to an increase in SE and a decrease in t_d (closer to the target td of 9 h). Note that the ratio of shell to tube diameter (R/r_o) of the LHTES system decreases along this path, as shown in *Table 5.4*. A decrease in R/r_o below 1.3 is generally not suitable as it leads to a tiny amount of the PCM in the shell region and leads to a large number of unit cells with low HTF velocities [24,49,50]. Thus, with R/r_o limited to 1.3, design $A_{-1.2}$ can be considered the optimum design and did not carry out another optimization cycle as

design $A_{-1.2}$ is located at the edge of the design space with a scarce chance of any significant improvement. The optimum design had higher SE and better discharging characteristics (t_d = 11.8 hours, against a target of 9 h) than the baseline design, leading to significantly higher desirability, as shown in *Table 5.4*. The ε and Q were also considerably improved in the optimum design.

Table 5.4 The performance of the optimized design of LHTES for baseload CSP plant obtained using response surface methodology (RSM) compared with the baseline design

Path	Designs	L (m)	r_o (cm)	R (cm)	R/r_o (-)	N_p (-)	u_m (mm/s)	t_c (h)	t_d (h)	SE (-)	ε (MJ/kg)	Q (MWh)	D (-)
	Baseline	50	1.30	2.8	2.15	114,819	11.86	8.9	12.4	0.32	0.352	2953.1	0.371
Path 1→	$A_{1.5}$	50	1.21	3.75	3.00	57,967	27.24	6.3	10.0	0.22	0.237	2057.3	0.429
	$A_{1.0}$	50	1.27	3.42	2.70	71,638	19.92	7.2	10.9	0.25	0.276	2366.0	0.417
	A_0*	50	1.39	2.77	2.00	121,586	9.73	9.0	12.5	0.32	0.360	2985.7	0.366
←Path 2	A_{-1}	50	1.50	2.11	1.40	277,863	3.58	9.0	12.0	0.33	0.419	3051.5	0.405
	$A_{-1.2}$**	50	1.53	1.98	1.30	356,139	2.71	9.0	11.8	0.33	0.451	3053.1	0.418
	$A_{-1.5}$	50	1.56	1.79	1.14	585,722	1.57	9.0	11.4	0.33	0.580	3053.2	0.444

**Stationary point design, ** Optimized design*

However, the optimized design had a higher discharge time (11.8 h) than the target (9 h) set for the LHTES system to be used in a baseload-CSP power plant, meaning that the system would be slow to discharge. In other words, on charging the baseload-CSP plant (with solar multiplier = 3) for 9 h, the plant will run for 23.6 h (11.8 h × 2) after sunny hours, which is higher than the desired storage capacity of 18 h.

However, the slow-discharging characteristics of the LHTES system may even prove *beneficial* for the baseload-CSP plant since the plant can remain operational (at part load conditions) even with reduced charging hours. To verify this, the optimized design was simulated with charging time reduced from 9 h to 6 h, as shown in *Table 5.5*. It was found that even if this LHTES system is charged for 7 hours, the system can discharge for 9.3 h (against a targeted t_d of 9 h) with Q equal to 2033.7 MWh. Charing hours below 7 h will lead to insufficient energy storage for running a baseload CSP plant. Thus,

the optimized design seems adequate to deliver the required power to run the baseload CSP plant, as long as the charging duration is more than 7 hours.

Table 5.5 Performance of optimized design of LHTES for baseload CSP plants with discharging time of 6 to 9 h

t_c	L	r_o	R	u_m	t_d	SE	ε	Q
(h)	*(m)*	*(cm)*	*(cm)*	*(mm/s)*	*(h)*	*(-)*	*(MJ/kg)*	*(MWh)*
9	50	1.53	1.98	2.71	11.8	0.33	0.451	3053.1
8	50	1.53	1.98	2.71	10.5	0.29	0.400	2713.4
7	50	1.53	1.98	2.71	9.3	0.26	0.350	2373.5
6	50	1.53	1.98	2.71	8.1	0.22	0.300	2033.7

5.4 Summary

The TES system integrated with the peak load CSP plant has t_d, SE, and Q of 12.3 h, 33%, and 3034 MWh, respectively. Compared to the baseline design, optimized design performance improved by 1%. Similarly, the TES system integrated with a hybrid PV-CSP plant has t_d, SE, and Q of 11.8 h, 33%, and 3053.1 MWh, respectively. Performance of optimized design improved by 12.66% over baseline design. Both design configurations accomplished the respective objectives required for hybrid PV-CSP and baseload CSP plants.

Chapter 6 Compatibility of structural materials with AlSi12 alloys-based phase change material and enhance the corrosion resistance property by ceramic coatings[4]

This chapter presents the compatibility of steel structural materials (SS316, SS202, and P91) with molten AlSi12. Simultaneously, ceramics coatings as the corrosion resistance protection layer over the steel coupons are investigated. This study suggests a suitable steel substrate and ceramic coating for the structural material of the TES system's container.

6.1 Experimental description

6.1.1 Materials

6.1.1.1 Synthesis of AlSi12 alloy (PCM)

A 150 g of AlSi12 sample was prepared using the stoichiometric proportion of primary metals, i.e., 88 % (by weight) of Al shots and 12% (by weight) of Si granular supplied by Alfa Aesar (with purity higher than 99.9%), as shown in step 1 of *Fig. 6.1*. The primary metals were weighed (using Contech CAH-223 high precision digital balance with a precision limit of 0.001 g), mixed, and placed in an alumina boat, after which the crucible was heated to 900 °C for five hours in a vacuum atmosphere. External mechanical stirrings were given at regular intervals to ensure the homogeneity of the alloy. The primary metals melted and formed an ingot of AlSi12 alloy, which was taken for microstructural and XRD examination, as described in *Section 6.2.1*.

[4] This work is in under review in the Journal of Energy Storage (submitted in November 2022).

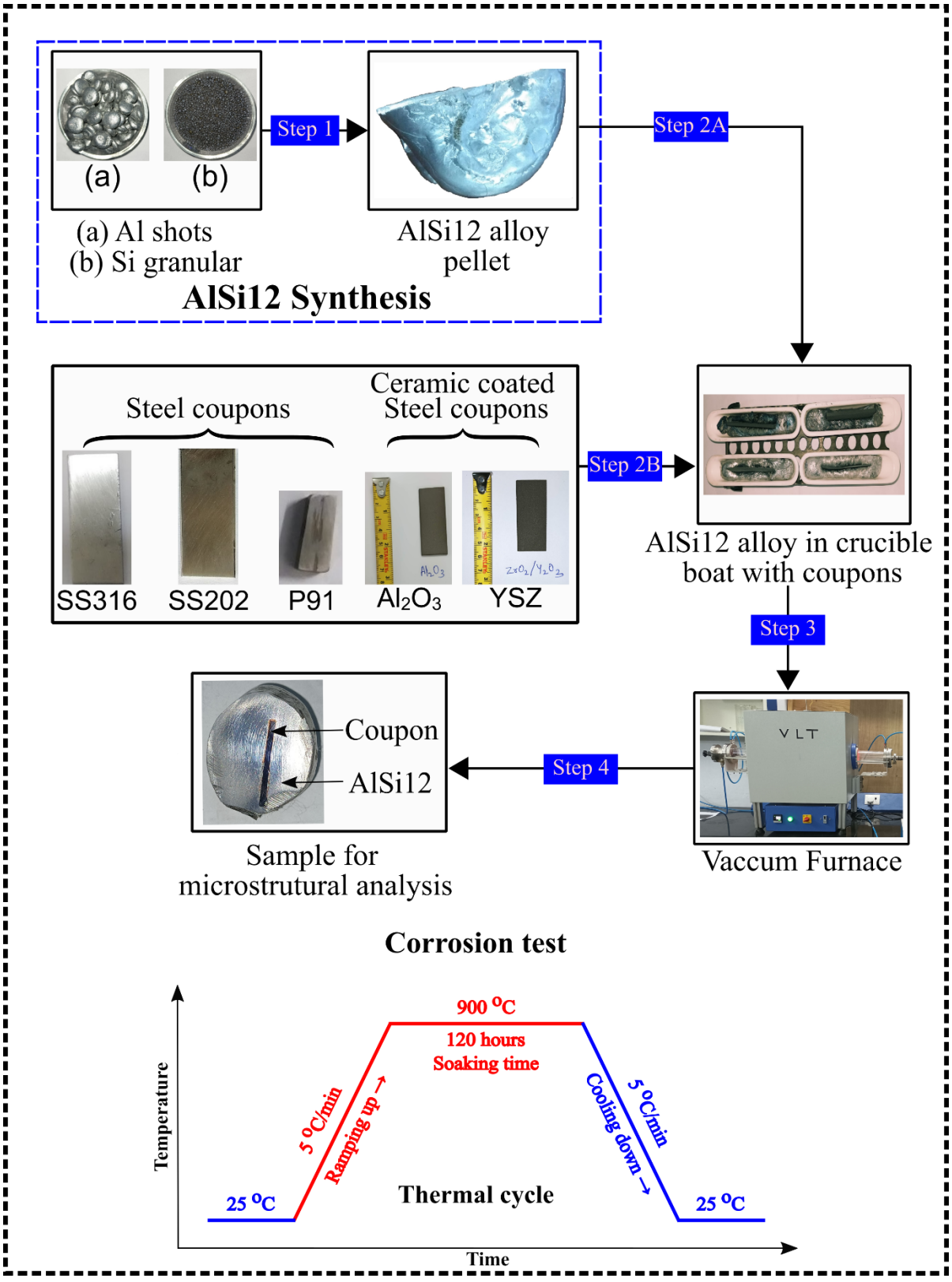

Fig. 6.1 Corrosion test (upper) and Thermal cycle (lower)

6.1.1.2 Steels and ceramic-coated steels structural materials coupons

This study's objectives are as follows: a) compatible steel structural materials and b) corrosion-protective coating over steel structural material. The former part of the study investigated the corrosion of AlSi12 alloy with three steel structural materials, i.e., SS316, SS202, and P91, as shown in *Fig. 6.2* [32], where the P91 has the lowest percentage of Cr and Ni in their composition. The structural materials were machined in the shape of coupons (5.0×2.0×0.2 cm^3) and polished, where the P91 coupon was a cut section of a pipe, and the other two coupons were carved from their respective metal sheets.

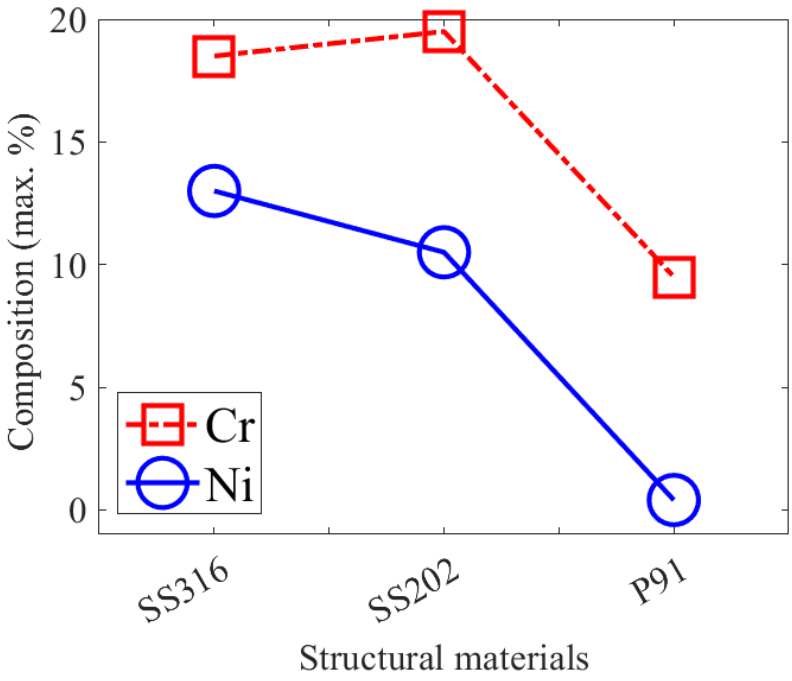

Fig. 6.2 Maximum composition of chromium (Cr) and nickel (Ni) in the structural materials (ASME specification, in wt.%) [32]

In the later part of the present study, the alumina (Al_2O_3) and yttria-stabilized zirconia (YSZ) ceramics were examined as corrosion-protective coatings on steel structural materials due to their proven corrosion resistance with molten AlSi12 [48,50,94]. Both the coatings were deposited on steel SS316 substrates (coupons size 5.0 × 2.0 × 0.2 cm3) using an atmospheric plasma spray technique (M/s. Spraymet Surface Technologies Pvt Ltd., Bangalore, India.) with an average thickness of 400 µm.

Before spraying, substrates are grit blasted with 150 µm alumina powder and bond coated with NiCoCrAlY to enhance bond strength and ceramic coating adhesion to steel substrates.

Fig. 6.3 Experimental facility a) front view, b) side view of the high-temperature vacuum furnace, and c) vacuum system

6.1.2 Corrosion test

After successfully synthesizing the AlSi12 alloy, the corrosion test was performed under the vacuum environment in a high-temperature furnace (manufactured by M/s. Vacuum & Lab Technologies, Bangalore, India), and additional furnace details are shown in *Fig. 6.3*. First, five AlSi12 alloy samples (20 g each) were melted in a vacuum furnace at 900 °C, as shown in step 2A of *Fig. 6.1*. Additionally, steel (SS316, SS202, and P91) and ceramic-coated steel (Al_2O_3 and YSZ) structural material coupons were heated simultaneously, as shown in step 2B. The coupons were perpendicularly inserted into the

AlSi12 alloy in the crucible, and consequently, the alloy was allowed to solidify. As soon as the samples had cooled (step 3), the crucibles were placed back in the vacuum furnace and conducted 120 hours of corrosion testing at an isothermal temperature of 900 °C under a vacuum environment (6.3 × 10-6 Torr). During the test, a steady 5 °C/min ramping and cooling rate were maintained to prevent thermal shock (as shown in the lower panel of *Fig. 6.1* – Thermal cycle). After 120 hours (step 4), the crucibles were brought to room temperature and, thus, the samples were cut transversely and polished. Morphological information between the coupons and AlSi12 alloy was recorded using FEI-SEM (Apreo S LoVac) and Oxford AZtec EDS for analyzing microstructural and elemental distribution.

6.2 Results and discussion

6.2.1 Microstructure and crystalline phase observation of AlSi12 (PCM)

After alloy synthesis, the AlSi12 sample was polished to observe the microstructure and surface morphology by optical microscope (GIPPON INC Japan), and the crystalline phase was analyzed by X-ray diffraction (Rigaku, Japan, SmartLab 9kW). *Fig. 6.4* presents the microstructure of AlSi12 and shows the presence of grey lamellar structured (fibrous shape) eutectic Si in the Al substrate; this is due to the AlSi12 being present in the form of a eutectic alloy of aluminum and silicon. Similarly, the diffraction pattern obtained from the sample indicates the presence of Al and Si as the elements based on Bragg's angle corresponding to the two elements present in the alloy. Thus, the Al and Si detected phase positions across Bragg peaks are shown using the blue diamond and the red square markers in *Fig. 6.5*, which presents the X-ray diffractograms of the crystalline phase of Al-Si eutectic alloy. The microstructure and XRD analysis obtained for AlSi12 have good agreement with the previous studies [47,48,94], which confirm the successful synthesis of Al-Si eutectic alloy.

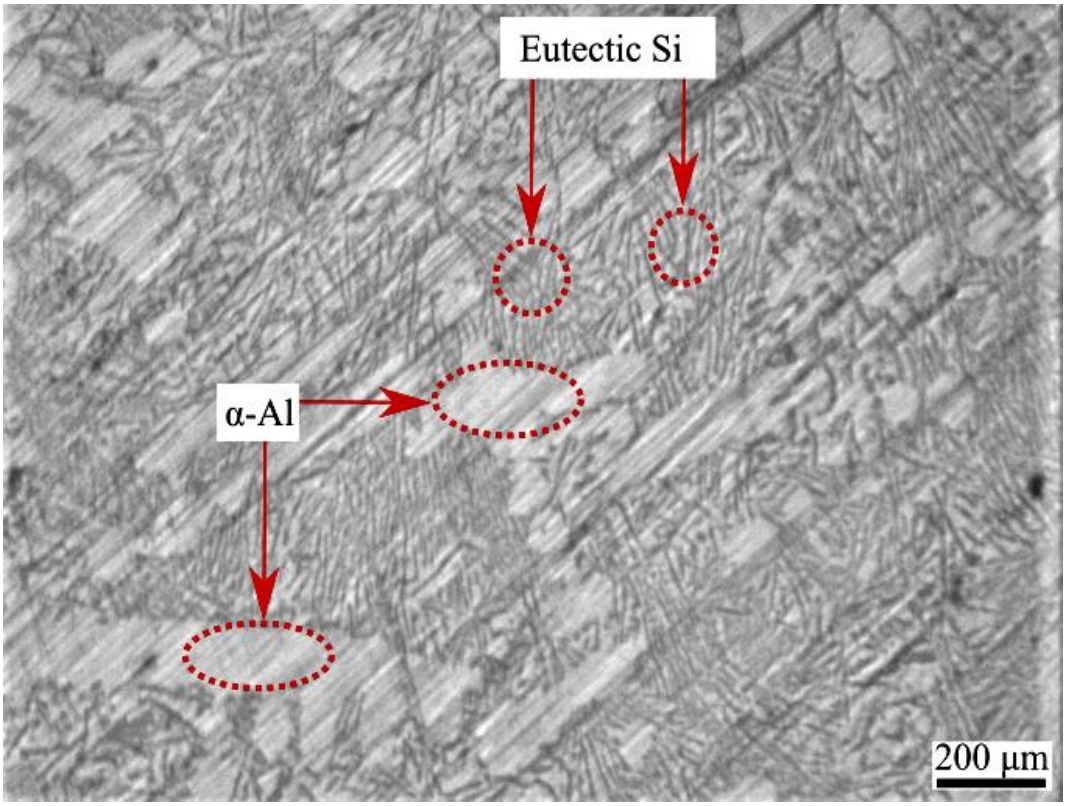

Fig. 6.4 Microstructure of synthesized AlSi12 alloy

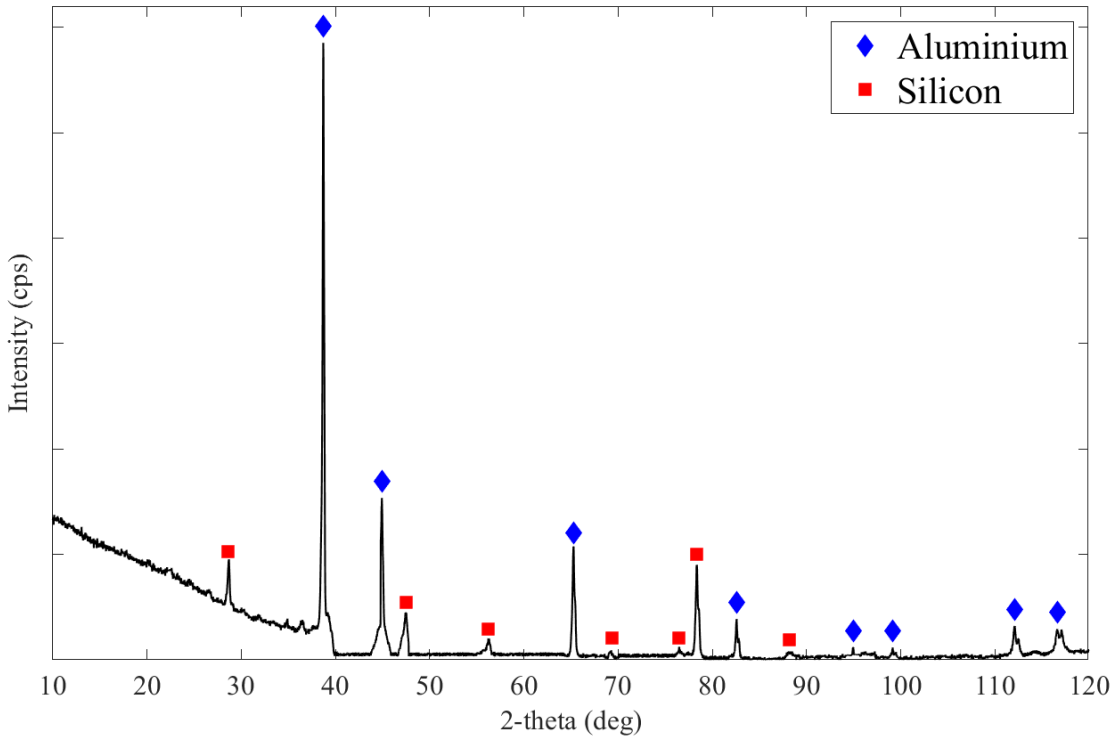

Fig. 6.5 X-ray diffraction (XRD) spectra of synthesized AlSi12 alloy

6.2.2 Interaction of steel structural materials with AlSi12 alloy

A heat transfer experimental investigation by Rea et al. [92] reported the failure of the TES prototype when SS316 dissolved in molten AlSi12. However, the present study reports the compatibility behavior of SS316, SS202, and P91 steels with molten AlSi12 alloy with the help of corresponding SEM and EDX maps after 120 hours of the corrosion test, shown in *Fig. 6.6*. The first observation in Fig. 6.6a (SEM micrograph and EDX mapping) is the reaction of the SS316 coupon with molten AlSi12, which results in the dissolution of the coupon. The observations show that the coupon has a significant change in thickness from 2mm to a few micrometers (< 25µm).

A similar interpretation can be made from Fig. 6.6b, where the SS202 coupon also reacted with molten AlSi12, although the corrosion reaction was less severe. Moreover, the thickness varied at different locations in the coupon, which indicates that corrosion was not uniform throughout the surface. However, Fig. 6.6c shows that P91 does not experience significant corrosion when in contact with molten AlSi12 since a clear boundary is visible between P91 and AlSi12. It is concluded that the corrosion reaction is very severe in SS316 and minimal in P91, as the Cr and Ni percentages in the steel composition are highest in SS316 and lowest in P91. These results are inevitable to show that steel's Ni and Cr percentage plays an essential role in selecting steel structural materials.

6.2.3 Corrosion test analysis between coated steel structural materials and AlSi12 (PCM)

As ceramics are inert to molten PCM, coating the steel surface with ceramic materials is a cost-effective way to prevent corrosion. The present study investigates alumina (Al_2O_3) and yttria-stabilized zirconia (YSZ) ceramic coatings as protective coats between steel and AlSi12 by analyzing corresponding SEM and EDX maps after 120 hours of the corrosion test. *Fig. 6.7a* shows the interaction between the Al_2O_3-coated steel with molten AlSi12. The result indicates that the steel coupon dissolved over the AlSi12, which proves that the Al_2O_3 coating was delaminated from the steel surface, allowing the molten AlSi12 to interact with the steel. However, *Fig. 6.7b* shows the YSZ coating remains intact during the experiment, which can be observed in the SEM micrograph and EDX mapping of the interface between YSZ-coated steel and AlSi12.

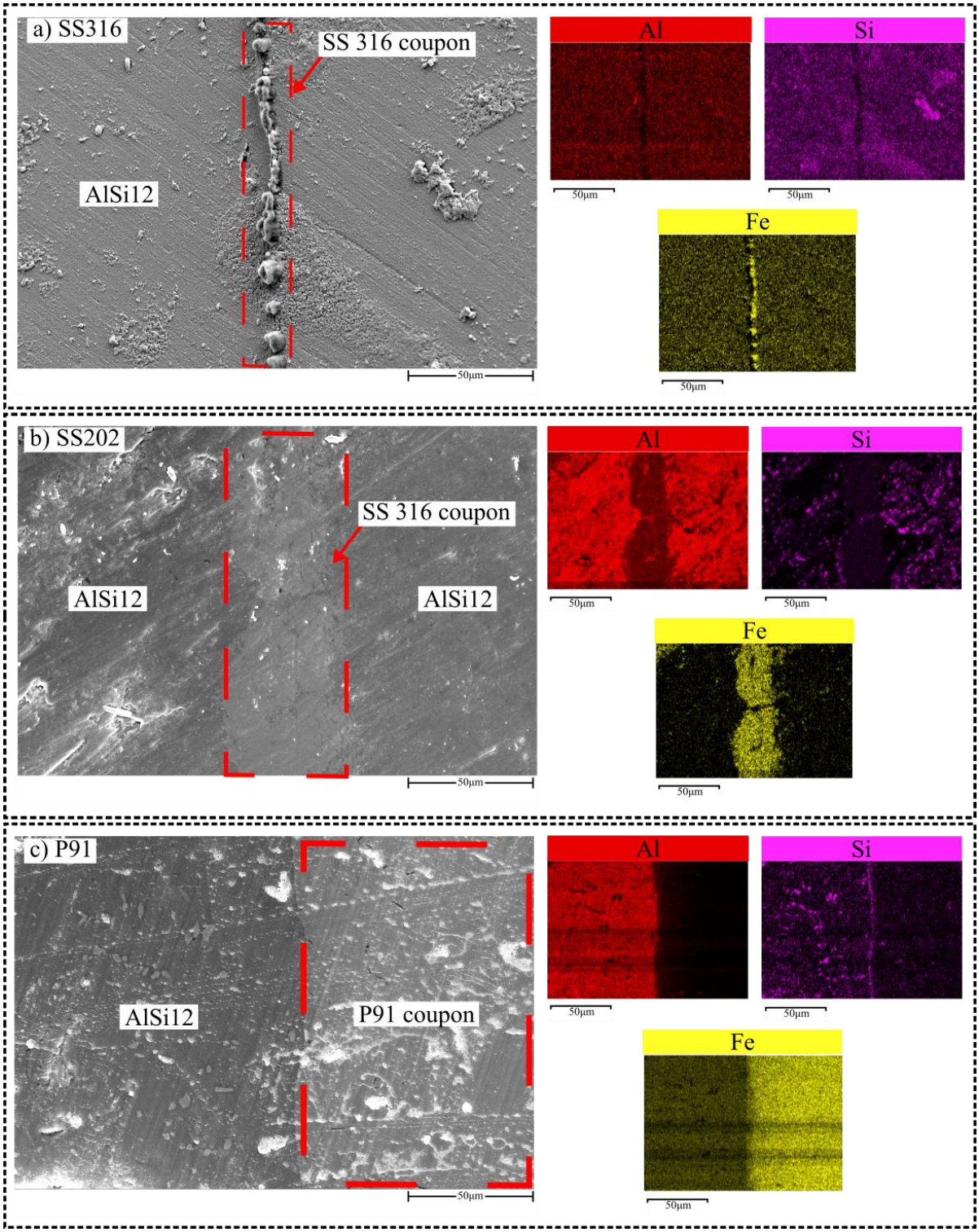

Fig. 6.6 SEM micrograph and EDX mapping of interface between SS316, SS202, and P91 with molten AlSi12 after 120 hours of isothermal (900 °C) corrosion test

The failure of Al_2O_3 coating can be explained as there is a difference in thermal expansion between Al-Si alloy (23×10^{-6}/°C) compared to Al_2O_3 (8×10^{-6}/°C). Mechanical stress was generated by the mismatch in the thermal expansions of materials, ultimately leading to failure to containment material. However, YSZ resists crack propagation due to the transformation toughening property [119], which not only extends the lifetime and reliability of the coating but also offers resistance to erosion and chemical reactions.

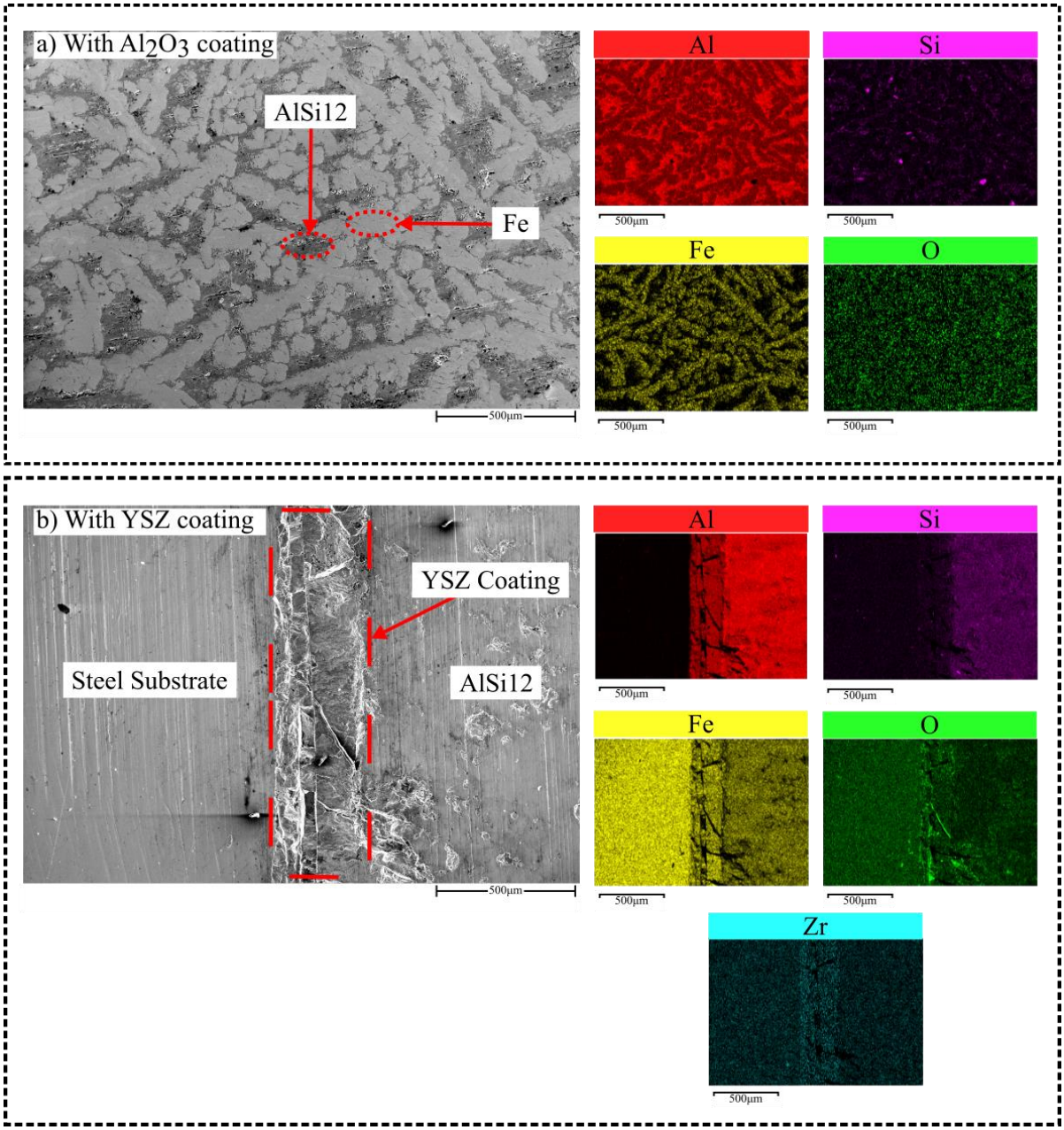

Fig. 6.7 SEM micrograph and EDX mapping of interface between SS316, SS202, and P91 with molten AlSi12 after 120 hours of isothermal (900 °C) corrosion test

6.3 Summary

This study examines the compatibility of steel structural materials (SS316, SS202, and P91) and ceramic-coated steel (alumina – Al_2O_3 and yttria-stabilized zirconia – YSZ) with molten AlSi12. The experiment indicates that P91 steel and YSZ-coated steel have better corrosion resistance when measured over 120 hours.

Chapter 7 Conclusion and future scope of the work

This study was motivated primarily by the desire to find out suitable LHTES system for next-generation CSP plants. The present work has carried out a numerical and material investigation for developing the LHTES system. In the former investigation, parametrical analysis (*Section 7.1*) and multi-objective design optimization (*Section 7.2*) were conducted using realistic operating conditions. And in the latter investigation (*Section 7.3*), a compatibility test was performed to find suitable structural materials and ceramic coatings.

7.1 Parametric analysis of an LHTES system

The study, presented in *Chapter 4*, investigated the performance of an AlSi12-based high-temperature LHTES system for integration in the next generation of CSP plants by *incorporating charging and discharging cutoff temperatures under periodic steady-state conditions* to mimic its real-world operation. This investigation demonstrated that with the incorporation of cutoff temperatures, the specific energy (ε) and storage effectiveness (SE) of the system decreased by 74% and 68%, respectively, due to lower useful charging (t_c) and discharging times (t_d). Furthermore, it is essential to study the LHTES system's performance under periodic steady-state; otherwise, the performance predictions can be severely biased due to the impact of the system's initial state on its performance.

In light of the above, by varying the geometrical and operational parameters of the LHTES system, including its shell radius (R), tube radius (r_o), length (L), and the HTF's flow velocity (u_m), an analysis was carried out to examine their effect on the system's performance under realistic operating conditions. It was found that the system could be efficiently charged and discharged for longer durations by either increasing R or L since an increase in these parameters meant more PCM was available for energy storage. On the other hand, t_c and t_d reduced with an increase in r_o or u_m since increasing those parameters mainly led to an increase in the thermal energy content of the HTF, which meant that the LHTES system could be charged and discharged quickly. The LHTES system's geometry and the HTF's flow velocity also substantially influenced its performance as characterized by ε and SE metrics,

but in a different manner than their influence on t_c and t_d. For the range of parameters investigated in this study, the system's performance improved by either reducing R (from 3.9 to 1.7 cm); or by increasing r_o (from 0.5 to 1.3 cm), L (from 6 to 12 m), or u_m (from 0.4 to 2.17 mm/s). A further increase in r_o (from 1.3 to 1.5 cm), L (from 12 to 16 m), or u_m (from 2.17 to 5.8 mm/s) was found detrimental to the system's performance.

Finally, an optimized design was proposed with high t_c and t_d as well as improved performance, using the response surface methodology. The optimized design could not only be charged for the full nine hours but also had SE and ε values that were 33% and 43% higher, respectively, than the previous best design.

7.2 Multi-objective design optimization of an LHTES system

In this study (*Chapter 5*), using the response surface methodology (RSM) technique, the main focus was optimizing the shell-and-tube LHTES system design for the hybrid PV-CSP and baseload CSP plants. A two-dimensional numerical model was used to evaluate the performance of the unit cell under realistic operating conditions, where the L, R, r_o, and $\dot{m}$ as the input, and output as SE and t_d. An iterative method was proposed to find the $\dot{m}$ for the respective design of the unit cell (with L, R, and r_o) and the baseline design was chosen using an analytical eNTU approach. Lastly, a multi-objective design optimization – RSM was proposed for both plant configurations. Thus, the conclusion drawn from the results are as follows:

- The hybrid PV-CSP is the integrated system where the electricity generated using a PV system with cheaper production costs is delivered during sunny hours. Whereas, in non-sunny hours, the electricity is generated by the CSP plants using the inexpensive energy storage medium (LHTES). The objective was framed as optimizing the LHTES system for a hybrid PV-CSP plant to maximize the t_d and SE. As a result, the design was found optimum with R = 2.27 cm and r_o = 1.37 cm. The investigation depicted an insignificant influence of L on the system's performance; thus, it was selected as 50 m. The optimized design has t_d of 12.3 h. The values for SE, ε, and Q were found as 0.33, 0.384 MJ/kg, and 3034.8 MWh, respectively.

- The baseload CSP plants are designed to operate round the clock and deliver constant electricity. The TES system for this plant consists of two identical storage blocks, each charged by a solar field during sunny hours. The TES blocks will be discharged one after the other during hours of low solar radiation, making the cumulative discharging time a minimum of 18 h (i.e., total non-sunny hours). Thus, the objective for optimizing the LHTES system of a base load power plant is to obtain t_d equal to 9 h and maximize the SE. As a result, with parameters R = 1.98 cm and r_o = 1.53 cm, the design reached its optimum stage. Similar to the previous plant configuration, L was selected as 50 m due to its negligible effect on the system's performance. Furthermore, the system's performance for SE and ε were found as 0.33 and 0.451 MJ/kg, respectively. The cumulative Q was 6106.2 MWh, with t_d of 23.6 h for both identical storage blocks. The proposed TES system can even deliver energy as low as 7 h of t_c.

In summary, the optimized designs achieve the objectives for both configurations, improving over baseline designs by 1% and 27.22% for the hybrid PV-CSP plant and the baseload CSP plant, respectively.

7.3 Compatibility between AlSi12 and structural materials

This study (presented in *Chapter 6*) has examined the corrosion resistance properties of steel structural materials (SS316, SS202, and P91) and ceramic-coated steels (Al_2O_3 and YSZ) in AlSi12. Compatibility tests were carried out in a vacuum environment at an isothermal temperature of 900 °C for 120 hours. According to the results, the following conclusions are drawn:

- SS316 entirely dissolved in the molten AlSi12, whereas molten AlSi12 penetrated SS202. In comparison to SS316 and SS202 stainless-steel coupons, the P91 offers good corrosion resistance for the duration of the experiment.

- Al_2O_3 coating on steel was unstable as the coating lost its strength during the experiment, which allowed molten AlSi12 to react with steel, resulting in its dissolution. In contrast to Al_2O_3, YSZ offers stability during the investigation due to its transformation toughening property.

This study suggests that P91 steel can serve as a structural material for the AlSi12 thermal energy storage system, and YSZ ceramic coating may act as a protective coating. It is recommended that the compatibility study between YSZ-coated P91 and molten AlSi12 be conducted beyond 120 hours to examine microstructural changes on the coated surface. Therefore, the present study enables plant developers to make informed decisions regarding the choice of structural materials and ceramic coatings for AlSi12-based high-temperature LHTES.

The major conclusions from this chapter can be summarized as follows:

1. Parametric analysis of an LHTES system:

    - Incorporating charging and discharging cutoff temperatures in the AlSi12-based LHTES system resulted in a decrease in specific energy (ε) and storage effectiveness (SE) due to reduced useful charging and discharging times.

    - The system's performance was influenced by geometrical and operational parameters such as shell radius (R), tube radius (r_o), length (L), and HTF's flow velocity (u_m).

    - Increasing R or L allowed for efficient charging and discharging for longer durations by providing more PCM for energy storage.

    - Increasing r_o or u_m led to reduced charging and discharging times by increasing the thermal energy content of the HTF.

    - The optimized design achieved high charging and discharging times, as well as improved performance compared to previous designs.

2. Multi-objective design optimization of an LHTES system:

    - The hybrid PV-CSP plant's LHTES system was optimized to maximize discharging time (t_d) and storage effectiveness (SE) by adjusting parameters such as R and r_o.

- The baseload CSP plant's LHTES system was optimized to achieve a minimum discharging time of 9 hours and maximize SE by adjusting parameters R and r_o.
- Length (L) had a negligible effect on the system's performance in both plant configurations.
- The optimized designs significantly improved performance compared to baseline designs, achieving the desired objectives.

3. Compatibility between AlSi12 and structural materials:

- SS316 stainless steel entirely dissolved in molten AlSi12, while molten AlSi12 penetrated SS202 stainless steel. P91 steel exhibited good corrosion resistance.
- Al_2O_3 coating on steel was unstable and lost its strength, allowing molten AlSi12 to react with steel. YSZ coating offered stability due to its transformation toughening property.
- P91 steel can serve as a suitable structural material, and YSZ ceramic coating may act as a protective coating for the AlSi12-based LHTES system.
- Further compatibility studies beyond 120 hours are recommended to examine microstructural changes on the coated surface.

These conclusions provide valuable insights into the performance, design optimization, and compatibility of the AlSi12-based high-temperature LHTES system, facilitating informed decision-making for the selection of structural materials and ceramic coatings in future CSP plant developments.

7.4 Future scope of work

The present work conducted the numerical and material investigations required for developing the LHTES system. However, further work is needed to bring the LHTES system to the commercial production level (see *Fig. 2.1*). In light of the present work's findings, the following recommendations are made for future research:

- The present study investigated the LHTES system with a single PCM configuration. However, multiple PCMs (cascaded) configurations should be analyzed using realistic operating conditions to see their impact on the system's average liquid-fraction and storage effectiveness.

- Heat transfer due to natural convection in the PCM was neglected in the present study, which was reasonable since all the investigated LHTES system geometries satisfied the condition recommended by Tehrani et al. [105] for neglecting natural convection effects in a shell-and-tube type LHTES system. The primary reason for neglecting natural convection effects was to save on computational time since each simulation had to be run for a very long duration (ten days) to achieve periodic steady-state conditions. However, the error of neglecting natural convection should be recalculated using realistic operating conditions.

- A detailed techno-economic analysis conducted in collaboration with global manufacturers will be used to assess LHTES' economic performance. The results of this study can provide insight into the development of the LHTES system as well as cost comparisons of competing energy storage technologies.

- LHTES system's numerical results should be compared with the experimental investigation at the prototype and pilot project (field test) levels before commercial production. The results will provide a better understanding of the system's actual thermal behavior and heat transfer performance.

Appendix A: Design optimization

This investigation used the response surface methodology (RSM) for conducting the design optimization of the LHTES system. RSM proceeds through the following three steps to achieve design improvements [120]:

Step 1. Set up a series of experiments (with different design variables) for adequate predictions of a response (the objective) within a region of interest.

Step 2. Fit an empirical model (typically linear or quadratic models are used) to the data obtained from the experiments conducted in the preceding step.

Step 3. Determine the optimum conditions on the design variables that optimize (minimize or maximize) the response.

Thus, in RSM, the above–mentioned steps are applied through successive design cycles to improve the response (the objective) until an optimum is achieved.

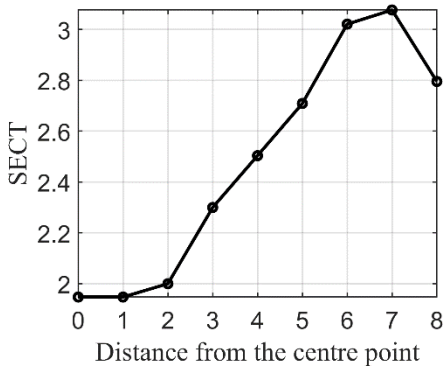

Fig. A- 1 Response (D) obtained from CFD simulations conducted along the path of steepest ascent in the first design cycle

In this investigation, the design variables were u_m, r_o, R, and L, with the objective being to maximize D (the product of storage effectiveness and charging time). The baseline design (L = 10 m, r_o = 1.3 cm, R = 2.8 cm, and u_m = 2.17 mm/s) was taken as the center point, and then used the 2^4 factorial design (see *Table A- 1*) to initiate the first design cycle of RSM. In the first cycle, It was found that a first-order model (with linear and two-way interaction terms) was adequate to model the response (D)

in the region of interest. Since the first-order model was found adequate, additional CFD simulations were conducted in the direction that the model recommended providing a maximum increase in D (the direction of steepest ascent, see *Fig. A- 1*), until the D values started to deteriorate, indicating the end of the first design cycle. This approach found that D could be improved by 58.0 % with respect to the center point, and the new design variables were L = 13.90 m, r_o = 1.18 cm, R = 1.99 cm, and u_m = 1.75 mm/s. Note that the fitted model is only accurate in the region where the experiments were conducted during Step-1 of the RSM cycle; thus, choosing the model further and further away from the experimental region, the model's performance deteriorates, and additional experiments are required.

Table A- 1 The design variables for the first design cycle

Factor	Length (L, m)	Tube radius (r_o, cm)	Shell radius (R, cm)	Velocity (u_m, mm/s)
Factorial high	12.0	1.40	3.35	2.50
Centre point	10.00	1.30	2.80	2.17
Factorial low	8.0	1.20	2.25	1.78

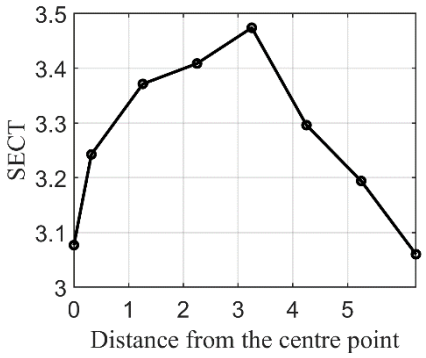

Fig. A- 2 Response (D) obtained from CFD simulations conducted along the canonical path in the second design cycle

In the second RSM design cycle, further CFD simulations were performed using the 24-factorial design centered around the point found to be the best in the previous cycle (L = 13.90 m, r_o = 1.18 cm, R = 1.99 cm, and u_m = 1.75 mm/s). However, a first-order model was found inadequate to model the response in this region– an indication of curvature in the response. Thus, additional simulations were conducted using the central composite design (CCD), in which eight more axial runs were added to the previous 24 factorial designs (see *Table A- 2*). A second-order model (with linear, quadratic, and two-way interaction terms) was fitted for which the canonical analysis showed a rising-

ridge stationary point, indicating that moving outside the current design space might provide further performance improvements [121]. Thus, further CFD simulations were conducted along the canonical path recommended by the model (direction of the steepest ascent applied to a second-order) to increase D further, as shown in *Fig. A- 2*. This further increased the D by 12.9% as compared to the previous best design, with the new design variables being L = 15.64 m, r_o = 1.10 cm, R = 1.58 cm, and u_m = 1.47 mm/s, thus completing the second design cycle.

Table A- 2 The design variables for the second design cycle

Factor	Length (L, m)	Tube radius (r_o, cm)	Shell radius (R, cm)	Velocity (u_m, mm/s)
Axial high	15.90	1.28	2.54	2.08
Factorial high	14.90	1.23	2.26	1.91
Centre point	13.90	1.18	1.99	1.75
Factorial low	12.90	1.13	1.71	1.58
Axial low	11.90	1.08	1.44	1.42

To initiate the third design cycle, more CFD simulations (using the 2^4 factorial design) were conducted around the previous best design (L = 15.64 m, r_o = 1.10 cm, R = 1.58 cm, and u_m = 1.47 mm/s). Once again, a first-order response function was found inadequate; thus, additional simulations were conducted using the central composite design, as shown in *Table A- 3*.

Table A- 3 The design variables for the third design cycle

Factor	Length (L, m)	Tube radius (r_o, cm)	Shell radius (R, cm)	Velocity (u_m, mm/s)
Axial high	17.64	1.30	1.88	1.77
Factorial high	16.64	1.20	1.73	1.62
Centre point	15.64	1.10	1.58	1.47
Factorial low	14.64	1.00	1.43	1.32
Axial low	13.64	0.90	1.28	1.17

A second-order model was found adequate in this region, as given by:

$$D = 58.96 - 0.91L - 25.10r_o - 34.97R - 9.86u_m + 5.33Ru_m - 8.67r_o u_m + 0.67\,Lu_m + 29.33\,r_o R - 4{r_o}^2 - 1.6R^2 \quad \textit{Eq. A- 1}$$

where D is the response predicted by the model. Note that the model equation only contains terms deemed statistically significant, and the models' R^2 and R^2_{adj} were equal to 0.87 and 0.78, respectively. *Fig. A- 3* shows actual and model-predicted D values for the third design cycle and indicates that the second-order model can appropriately predict the response.

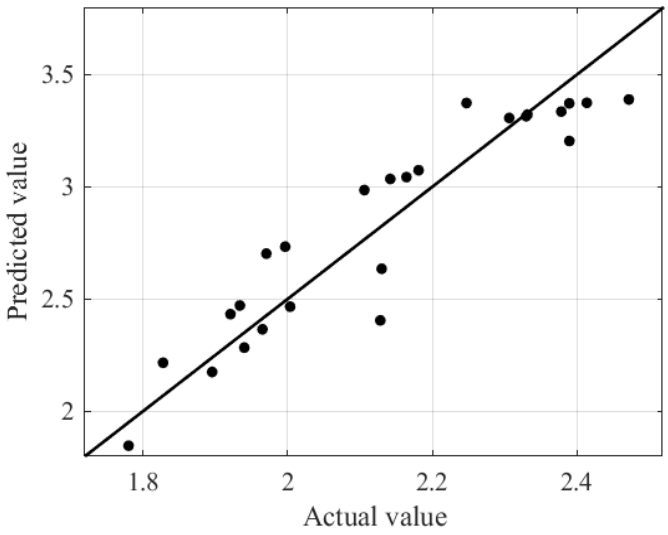

Fig. A- 3 Actual and model-predicted value of D

The canonical analysis of the model showed a stationary saddle point where the response is neither maximum nor minimum. Thus, further simulations were conducted along the canonical path, as shown in *Fig. A- 4*. The performance of the design with L = 14.77 m, r_o = 1.17 cm, R = 1.58 cm, and u_m = 1.26 mm/s was found to be the best- D increased by 6.0% as compared to the previous best design (see *Fig. A- 4*). Since the D increment obtained in this cycle was only 6%, additional RSM design cycles were not conducted and provided the top five design choices (based on D) in *Table 4.1*. Clearly, the suggested designs improved the D value by 31–36% compared to the previous best design choice, as shown in *Table 4.1*.

Fig. A- 5a shows the temporal variation of HTF temperatures at Z/L = 1 and Z/L = 0 during the charging and discharging processes for choice # 1 recommended by RSM and the previous best design. It is conspicuous that useful charging hours slightly increased (from 8.8 h to 9.0 h) while the discharging hours marginally decreased (from 12.2 h to 11.8 h) due to the optimization process. It was also found that the new design choice could provide higher HTF temperatures during the discharging process (leads

to higher power cycle efficiency), and lower HTF temperatures (leads to higher receiver efficiency) during the charging process, as compared to the previous best design, as shown in *Fig. A- 5a*. Thus, the adopted optimization technique significantly improved the LHTES system's performance and the CSP plant efficiency. It was also noted that the optimized design has a significantly higher liquid-fraction (0.20) at the end of the charging process (see *Fig. A- 5b*) compared to the previous best design (0.11).

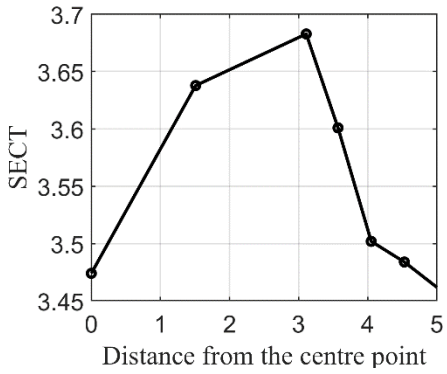

Fig. A- 4 Response (D) obtained from CFD simulations conducted along the canonical path in the third design cycle

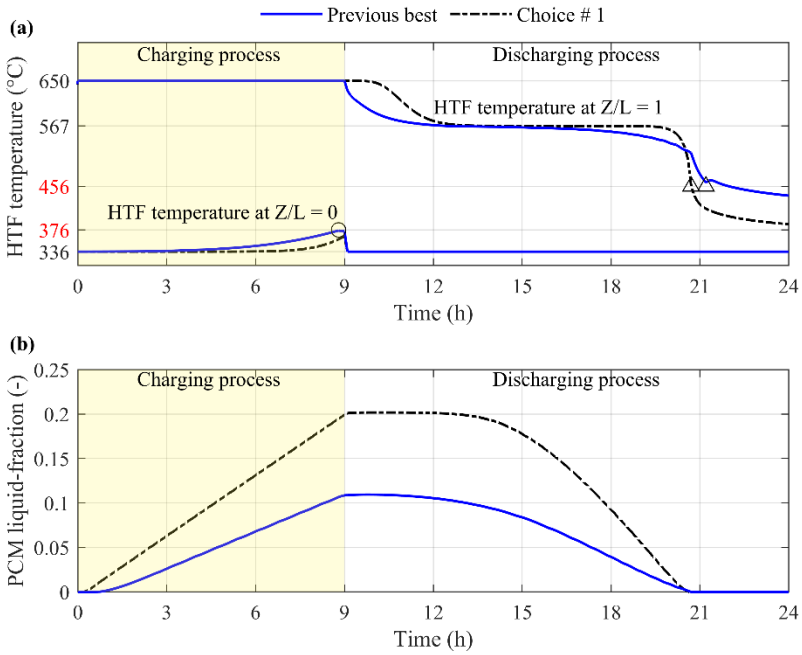

Fig. A- 5 The temporal variation of the a) average HTF temperature and b) average PCM liquid-fraction in the previous best design and design choice # 1 obtained from the response surface methodology

Appendix B: Preliminary design using an analytical solution 'e-NTU'

To select the preliminary design of the unit cell (geometry - L, r_o, and R as shown in *Fig. 3.2c*) for investigation, we have chosen an analytical method, 'eNTU' [122–127]. In this method, the effect of the unit cell's geometry and HTF's velocity on the average effectiveness is investigated, where average effectiveness ($\bar{\varepsilon}$) can be defined as the ratio of the difference between the inlet temperature and outlet temperature to the difference between the highest and lowest operating temperature of the TES system at the time of charging operation.

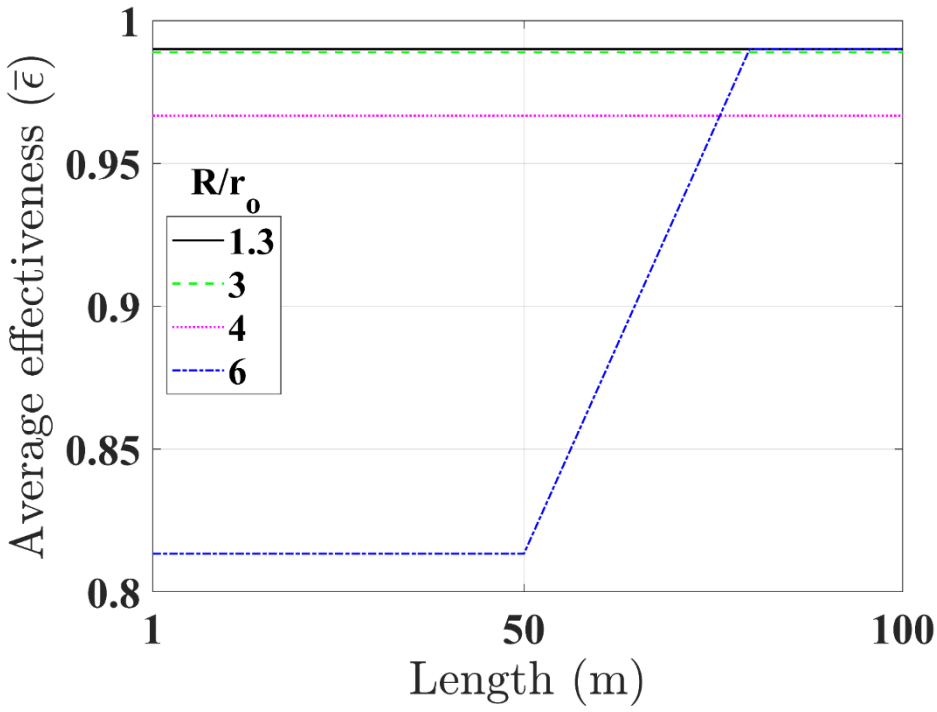

Fig. B- 1 Effect of variation of the ratio of R to the ro from 1.3 to 6 and length from 1 to 100 on the Average effectiveness

$$\bar{\boldsymbol{\varepsilon}} = \frac{T_H - T_{output}}{T_H - T_L} \qquad \textit{Eq. B- 1}$$

Further details of the eNTU method can be found in Tay et al. [124].

Initially, the values for r_i and r_o were chosen as constant (i.e., 1.2 and 1.3 cm, respectively), and the ratios of R/r_o varied from 1.3 to 6 to find R values. For every R/r$_o$, A range of L from 1 to 100 m

was investigated. As the length increases, the number of unit cells decreases, increasing the velocity of HTF in each unit cell. *Fig. B- 1* shows that for R/r_o < 3, $\bar{\varepsilon}$ was always nearly 0.99**.** On the other hand, $\bar{\varepsilon}$ is less than 0.99 for R/r_o > 3 when Re < 2300 and $\bar{\varepsilon}$ is nearly 0.99 for R/r_o > 3 when Re > 2300. To maximize $\bar{\varepsilon}$ and maintain flow in the laminar region, the value for R/r_o was selected as 2.15 (mean value between 1.3 and 3). Similarly, the value for L was selected as 50 m (mean value between 1 and 100 m). Thus, a geometry for base case design (with L = 50 m, r_i = 1.2 cm, r_o = 1.3 cm, and R = 2.8 cm) was chosen.

It must be noted that SE was assumed to be 0.5, for which the number of unit cells and velocity in each unit cell were found to be 75,477 and 18.04 mm/s, respectively. In order to verify this assumption, a CFD simulation was set up using chosen base case design, and it was found that the actual SE was 0.27, which is less than the assumed SE. Thus, the process of assuming SE and running CFD simulations was reiterated until the assumed SE was equal to the actual SE, which was found after three iterations. Finally, the base case design (with L = 50 m, r_i = 1.2 cm, r_o = 1.3 cm, R = 2.8 cm, and u_m = 11.86 mm/s) was selected for further investigation. The number of unit cells and velocity in each unit cell for this design were found to be 114,819 and 11.86 mm/s, respectively (refer to *Fig. B- 2*). A newer SE was assumed using *Table B- 1*, where α is the relaxation factor.

$$New\ assumed\ SE = old\ assumed\ SE + \alpha\ (actual\ SE - old\ assumed\ SE) \qquad Eq.\ B\text{-}\ 2$$

Table B- 1 Iterative CFD simulations for confirming the preliminary design

Case	L	R	r_o	Relaxation factor α	Assumed SE	N_p	u_m	Actual SE	$\bar{\varepsilon}$	t_c	t_d
	(m)	(cm)	(cm)	(-)	(-)	(-)	(mm/s)	(-)	(-)	(h)	(h)
A				-	0.5	75,477	18.04	0.27	0.94	5	7.5
B	50	2.8	1.3	0.75	0.34	110,445	12.33	0.31	0.97	8.4	11.8
C				0.65	0.33	114,819	11.86	0.33	0.97	8.9	12.4

Fig. B- 2 shows the temporal temperature profile of all three iterations. It can be noted that with every iteration, velocity is decreasing results in an increase of $\bar{\varepsilon}$, t_c, and t_d (refer to *Table B- 1*).

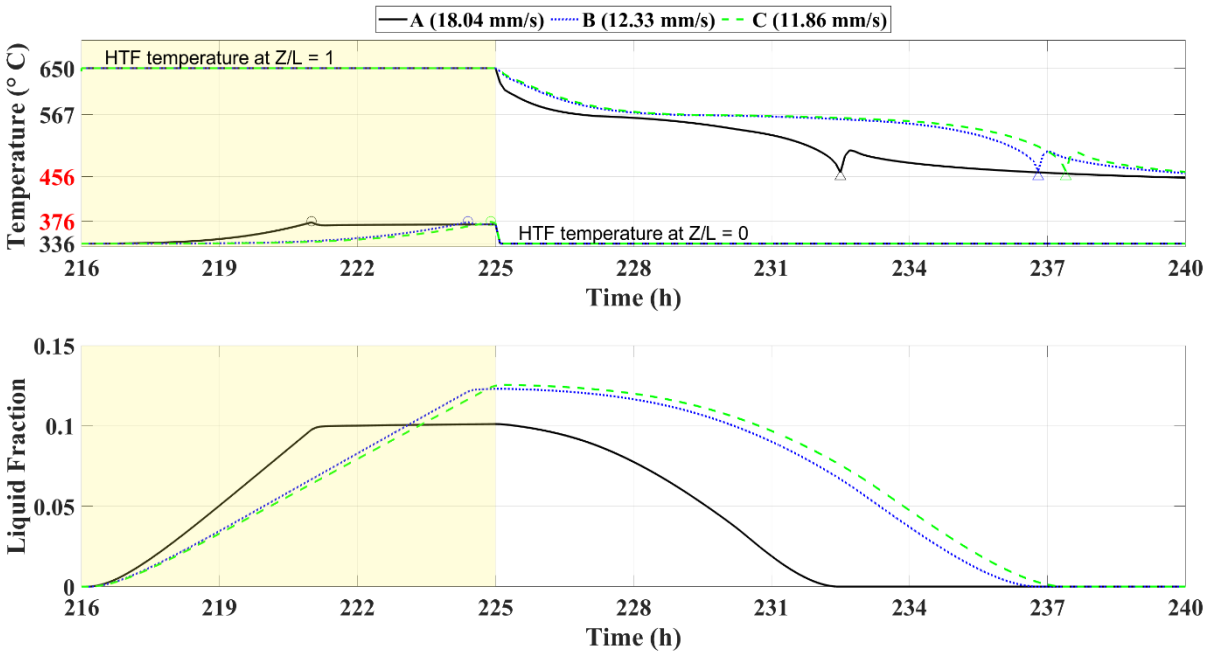

Fig. B- 2 Temporal temperature profile for Iterative CFD simulations cases for confirming the preliminary design

References

[1] IRENA, World Energy Transitions Outlook: 1.5 Degrees Pathway, Abu Dhabi, 2021. https://irena.org/publications/2021/March/World-Energy-Transitions-Outlook.

[2] IRENA, Renewable Power Generation Costs in 2021, Abu Dhabi, 2022. https://www.irena.org/publications/2022/Jul/Renewable-Power-Generation-Costs-in-2021.

[3] P. Denholm, M. O'Connell, G. Brinkman, J. Jorgenson, Overgeneration from Solar Energy in California: A Field Guide to the Duck Chart, 2015. http://www.nrel.gov/docs/fy16osti/65453.pdf.

[4] U.S. Department of Energy, Battery Storage in the United States: An Update on Market Trends, 2021. https://www.eia.gov/analysis/studies/electricity/batterystorage/pdf/battery_storage_2021.pdf.

[5] A. Bettoli, M. Linder, T. Nauclér, J. Noffsinger, S. Sengupta, H. Tai, G. van Gendt, Net-zero Power: Long Duration Energy Storage for a Renewable Grid, 2021. http://www.ldescouncil.com/insights.

[6] H.L. Zhang, J. Baeyens, J. Degrève, G. Cacères, Concentrated solar power plants: Review and design methodology, Renew. Sustain. Energy Rev. 22 (2013) 466–481. https://doi.org/10.1016/j.rser.2013.01.032.

[7] J. Khan, M.H. Arsalan, Solar power technologies for sustainable electricity generation - A review, Renew. Sustain. Energy Rev. 55 (2016) 414–425. https://doi.org/10.1016/j.rser.2015.10.135.

[8] A.G. Fernández, J. Gomez-Vidal, E. Oró, A. Kruizenga, A. Solé, L.F. Cabeza, Mainstreaming commercial CSP systems: A technology review, Renew. Energy. 140 (2019) 152–176. https://doi.org/10.1016/j.renene.2019.03.049.

[9] M.T. Islam, N. Huda, A.B. Abdullah, R. Saidur, A comprehensive review of state-of-the-art concentrating solar power (CSP) technologies: Current status and research trends, Renew. Sustain. Energy Rev. 91 (2018) 987–1018. https://doi.org/10.1016/j.rser.2018.04.097.

[10] O. Behar, A. Khellaf, K. Mohammedi, A review of studies on central receiver solar thermal power plants, Renew. Sustain. Energy Rev. 23 (2013) 12–39. https://doi.org/10.1016/j.rser.2013.02.017.

[11] Concentrating solar power generation in the Sustainable Development Scenario, 2000-2030, Int. Energy Agency. (2020). https://www.iea.org/data-and-statistics/charts/concentrating-solar-power-generation-in-the-sustainable-development-scenario-2000-2030 (accessed August 26, 2020).

[12] B. Xu, P. Li, C. Chan, Application of phase change materials for thermal energy storage in concentrated solar thermal power plants: A review to recent developments, Appl. Energy. 160 (2015) 286–307. https://doi.org/10.1016/j.apenergy.2015.09.016.

[13] G.J. Kolb, C.K. Ho, T.R. Mancini, J.A. Gary, Power Tower Technology Roadmap and

Cost Reduction Plan, 2011. https://prod-ng.sandia.gov/techlib-noauth/access-control.cgi/2011/112419.pdf.

[14] J. Lilliestam, R. Pitz-Paal, Concentrating solar power for less than USD 0.07 per kWh: finally the breakthrough?, Renew. Energy Focus. 26 (2018) 17–21. https://doi.org/10.1016/j.ref.2018.06.002.

[15] G.J. Kolb, An Evaluation of Possible Next-Generation High-Temperature Molten-Salt Power Towers, 2011. https://www.osti.gov/servlets/purl/1035342.

[16] O. Achkari, A. El Fadar, Latest developments on TES and CSP technologies – Energy and environmental issues, applications and research trends, Appl. Therm. Eng. 167 (2020) 114806. https://doi.org/10.1016/j.applthermaleng.2019.114806.

[17] I. Dincer, M.A. Rosen, Thermal Energy Storage: Systems and Applications, Third edi, Wiley, 2021. https://www.wiley.com/en-gb/Thermal+Energy+Storage%3A+Systems+and+Applications%2C+3rd+Edition-p-9781119713159.

[18] E. González-Roubaud, D. Pérez-Osorio, C. Prieto, Review of commercial thermal energy storage in concentrated solar power plants: Steam vs. molten salts, Renew. Sustain. Energy Rev. 80 (2017) 133–148. https://doi.org/10.1016/j.rser.2017.05.084.

[19] Q. Li, C. Li, Z. Du, F. Jiang, Y. Ding, A review of performance investigation and enhancement of shell and tube thermal energy storage device containing molten salt based phase change materials for medium and high temperature applications, Appl. Energy. 255 (2019). https://doi.org/10.1016/j.apenergy.2019.113806.

[20] S. Kuravi, J. Trahan, D.Y. Goswami, M.M. Rahman, E.K. Stefanakos, Thermal energy storage technologies and systems for concentrating solar power plants, Prog. Energy Combust. Sci. 39 (2013) 285–319. https://doi.org/10.1016/j.pecs.2013.02.001.

[21] S.S. Mostafavi Tehrani, R.A. Taylor, K. Nithyanandam, A. Shafiei Ghazani, Annual comparative performance and cost analysis of high temperature, sensible thermal energy storage systems integrated with a concentrated solar power plant, Sol. Energy. 153 (2017) 153–172. https://doi.org/10.1016/j.solener.2017.05.044.

[22] S. Seddegh, X. Wang, A.D. Henderson, Z. Xing, Solar domestic hot water systems using latent heat energy storage medium: A review, Renew. Sustain. Energy Rev. 49 (2015) 517–533. https://doi.org/10.1016/j.rser.2015.04.147.

[23] S.H. Goods, R.W. Bradshaw, M.R. Prairie, J.M. Chavez, Corrosion of stainless and carbon steels in molten mixtures of industrial nitrates, 1994. http://www.osti.gov/energycitations/servlets/purl/10141843-h6DbZ5/native/.

[24] M. Sarvghad, T.A. Steinberg, G. Will, Corrosion of stainless steel 316 in eutectic molten salts for thermal energy storage, Sol. Energy. 172 (2018) 198–203. https://doi.org/10.1016/j.solener.2018.03.053.

[25] A.G. Fernández, M.I. Lasanta, F.J. Pérez, Molten salt corrosion of stainless steels and low-Cr steel in CSP plants, Oxid. Met. 78 (2012) 329–348. https://doi.org/10.1007/s11085-012-9310-x.

[26] S.S.M. Tehrani, R.A. Taylor, P. Saberi, G. Diarce, Design and feasibility of high temperature shell and tube latent heat thermal energy storage system for solar thermal power plants, Renew. Energy. 96 (2016) 120–136.

https://doi.org/10.1016/j.renene.2016.04.036.

[27] B. Zalba, J.M. Marin, L.F. Cabeza, H. Mehling, Review on Phase changing materials to store energy, Appl. Therm. Eng. 23 (2003) 251–283. https://doi.org/10.1016/S1359-4311(02)00192-8.

[28] M. Liu, W. Saman, F. Bruno, Review on storage materials and thermal performance enhancement techniques for high temperature phase change thermal storage systems, Renew. Sustain. Energy Rev. 16 (2012) 2118–2132. https://doi.org/10.1016/j.rser.2012.01.020.

[29] B. Cárdenas, N. León, High temperature latent heat thermal energy storage: Phase change materials, design considerations and performance enhancement techniques, Renew. Sustain. Energy Rev. 27 (2013) 724–737. https://doi.org/10.1016/j.rser.2013.07.028.

[30] Y. Dutil, D.R. Rousse, N. Ben Salah, S. Lassue, L. Zalewski, A review on phase-change materials: Mathematical modeling and simulations, Renew. Sustain. Energy Rev. 15 (2011) 112–130. https://doi.org/10.1016/j.rser.2010.06.011.

[31] A.S. Fleischer, Thermal energy storage using phase change materials: Fundamentals and applications, 2015. https://doi.org/10.1007/978-3-319-20922-7.

[32] H. Nazir, M. Batool, F.J. Bolivar Osorio, M. Isaza-Ruiz, X. Xu, K. Vignarooban, P. Phelan, Inamuddin, A.M. Kannan, Recent developments in phase change materials for energy storage applications: A review, Int. J. Heat Mass Transf. 129 (2019) 491–523. https://doi.org/10.1016/j.ijheatmasstransfer.2018.09.126.

[33] A. Palacios, C. Barreneche, M.E. Navarro, Y. Ding, Thermal energy storage technologies for concentrated solar power – A review from a materials perspective, Renew. Energy. (2019). https://doi.org/10.1016/j.renene.2019.10.127.

[34] T. ur Rehman, H.M. Ali, M.M. Janjua, U. Sajjad, W.M. Yan, A critical review on heat transfer augmentation of phase change materials embedded with porous materials/foams, Int. J. Heat Mass Transf. 135 (2019) 649–673. https://doi.org/10.1016/j.ijheatmasstransfer.2019.02.001.

[35] S. Khare, M. Dell'Amico, C. Knight, S. McGarry, Selection of materials for high temperature latent heat energy storage, Sol. Energy Mater. Sol. Cells. 107 (2012) 20–27. https://doi.org/10.1016/j.solmat.2012.07.020.

[36] A.I. Fernández, C. Barreneche, M. Belusko, M. Segarra, F. Bruno, L.F. Cabeza, Considerations for the use of metal alloys as phase change materials for high temperature applications, Sol. Energy Mater. Sol. Cells. 171 (2017) 275–281. https://doi.org/10.1016/j.solmat.2017.06.054.

[37] C. Zhou, S. Wu, Medium- and high-temperature latent heat thermal energy storage: Material database, system review, and corrosivity assessment, Int. J. Energy Res. 43 (2019) 621–661. https://doi.org/10.1002/er.4216.

[38] E. Risueño, S. Doppiu, J. Rodríguez-Aseguinolaza, P. Blanco, A. Gil, M. Tello, A. Faik, B. D'Aguanno, Experimental investigation of Mg-Zn-Al metal alloys for latent heat storage application, J. Alloys Compd. 685 (2016) 724–732. https://doi.org/10.1016/j.jallcom.2016.06.222.

[39] E. Risueño, Investigation of Mg-Zn-Al Metal Alloys as New PCMs for Latent Heat

Energy Storage Applications, University of the Basque Country, 2016. http://hdl.handle.net/10810/21185.

[40] E. Risueño, A. Faik, A. Gil, J. Rodríguez-Aseguinolaza, M. Tello, B. D'Aguanno, Zinc-rich eutectic alloys for high energy density latent heat storage applications, J. Alloys Compd. 705 (2017) 714–721. https://doi.org/10.1016/j.jallcom.2017.02.173.

[41] E. Risueño, A. Gil, J. Rodríguez-Aseguinolaza, A. Gil, M. Tello, A. Faik, B. D'Aguanno, Thermal cycling testing of Zn–Mg–Al eutectic metal alloys as potential high-temperature phase change materials for latent heat storage, J. Therm. Anal. Calorim. 129 (2017) 885–894. https://doi.org/10.1007/s10973-017-6261-0.

[42] A. Rawson, C. Villada, M. Kolbe, V. Stahl, F. Kargl, Suitability of aluminium copper silicon eutectic as a phase change material for thermal storage applications: Thermophysical properties and compatibility, Energy Storage. 4 (2022) 1–15. https://doi.org/10.1002/est2.299.

[43] J.Q. Sun, R.Y. Zhang, Z.P. Liu, G.H. Lu, Thermal reliability test of Al-34%Mg-6%Zn alloy as latent heat storage material and corrosion of metal with respect to thermal cycling, Energy Convers. Manag. 48 (2007) 619–624. https://doi.org/10.1016/j.enconman.2006.05.017.

[44] Z. Sun, Linfeng Li, X. Cheng, J. Zhu, Y. Li, W. Zhou, Thermal properties and the prospects of thermal energy storage of Mg–25%Cu–15%Zn eutectic alloy as phase change material, Materials (Basel). 14 (2021). https://doi.org/https://doi.org/10.3390/ma14123296.

[45] Y. El Karim, Y. Grosu, A. Faik, R. Lbibb, Investigation of magnesium-copper eutectic alloys with high thermal conductivity as a new PCM for latent heat thermal energy storage at intermediate-high temperature, J. Energy Storage. 26 (2019) 100974. https://doi.org/10.1016/j.est.2019.100974.

[46] J.P. Kotzé, T.W. Von Backström, P.J. Erens, High temperature thermal energy storage utilizing metallic phase change materials and metallic heat transfer fluids, J. Sol. Energy Eng. Trans. ASME. 135 (2013). https://doi.org/10.1115/1.4023485.

[47] Z. Wang, H. Wang, M. Yang, W. Sun, G. Yin, Q. Zhang, Z. Ren, Thermal reliability of Al-Si eutectic alloy for thermal energy storage, Mater. Res. Bull. 95 (2017) 300–306. https://doi.org/10.1016/j.materresbull.2017.07.040.

[48] Y. Zhao, H.B. Liu, C.Y. Zhao, Experimental study on the cycling stability and corrosive property of Al-Si alloys as phase change materials in high-temperature heat storage, Sol. Energy Mater. Sol. Cells. 203 (2019) 110165. https://doi.org/10.1016/j.solmat.2019.110165.

[49] Z. Wang, H. Wang, X. Li, D. Wang, Q. Zhang, G. Chen, Z. Ren, Aluminum and silicon based phase change materials for high capacity thermal energy storage, Appl. Therm. Eng. 89 (2015) 204–208. https://doi.org/10.1016/j.applthermaleng.2015.05.037.

[50] R. Fukahori, T. Nomura, C. Zhu, N. Sheng, N. Okinaka, T. Akiyama, Thermal analysis of Al-Si alloys as high-temperature phase-change material and their corrosion properties with ceramic materials, Appl. Energy. 163 (2016) 1–8. https://doi.org/10.1016/j.apenergy.2015.10.164.

[51] M. Esen, T. Ayhan, Development of a model compatible with solar assisted cylindrical energy storage tank and variation of stored energy with time for different phase change materials, Energy Convers. Manag. 37 (1996) 1775–1785. https://doi.org/10.1016/0196-8904(96)00035-0.

[52] Y. Tao, M. Li, Y. He, W. Tao, Effects of parameters on performance of high temperature molten salt latent heat storage unit, Appl. Therm. Eng. 72 (2014) 48–55. https://doi.org/10.1016/j.applthermaleng.2014.01.038.

[53] L. Kalapala, J.K. Devanuri, Influence of operational and design parameters on the performance of a PCM based heat exchanger for thermal energy storage – A review, J. Energy Storage. 20 (2018) 497–519. https://doi.org/10.1016/j.est.2018.10.024.

[54] C. Bellecci, M. Conti, Phase change thermal storage: transient behaviour analysis of a solar receiver/storage module using the enthalpy method, Int. J. Heat Mass Transf. 36 (1993) 2157–2163. https://doi.org/10.1016/S0017-9310(05)80146-2.

[55] C. Bellecci, M. Conti, Transient behaviour analysis of a latent heat thermal storage module, Int. J. Heat Mass Transf. 36 (1993) 3851–3857. https://doi.org/10.1016/0017-9310(93)90065-E.

[56] Y. Cao, A. Faghri, Performance characteristics of a thermal energy storage module : a transient PCM/forced convection conjugate analysis, Int. Jounal Heat Mass Transf. 34 (1991) 93–101. https://doi.org/10.1016/0017-9310(91)90177-G.

[57] L. Kalapala, J.K. Devanuri, Parametric investigation to assess the melt fraction and melting time for a latent heat storage material based vertical shell and tube heat exchanger, Sol. Energy. 193 (2019) 360–371. https://doi.org/10.1016/j.solener.2019.09.076.

[58] W.W. Wang, L.B. Wang, Y.L. He, The energy efficiency ratio of heat storage in one shell-and-one tube phase change thermal energy storage unit, Appl. Energy. 138 (2015) 169–182. https://doi.org/10.1016/j.apenergy.2014.10.064.

[59] W. Wang, K. Zhang, L. Wang, Y. He, Numerical study of the heat charging and discharging characteristics of a shell-and-tube phase change heat storage unit, Appl. Therm. Eng. 58 (2013) 542–553. https://doi.org/10.1016/j.applthermaleng.2013.04.063.

[60] Y.B. Tao, Y.L. He, Numerical study on thermal energy storage performance of phase change material under non-steady-state inlet boundary, Appl. Energy. 88 (2011) 4172–4179. https://doi.org/10.1016/j.apenergy.2011.04.039.

[61] A. Trp, K. Lenic, B. Frankovic, Analysis of the influence of operating conditions and geometric parameters on heat transfer in water-paraffin shell-and-tube latent thermal energy storage unit, Appl. Therm. Eng. 26 (2006) 1830–1839. https://doi.org/10.1016/j.applthermaleng.2006.02.004.

[62] A. Trp, An experimental and numerical investigation of heat transfer during technical grade paraffin melting and solidification in a shell-and-tube latent thermal energy storage unit, 79 (2005) 648–660. https://doi.org/10.1016/j.solener.2005.03.006.

[63] M. Lacroix, Numerical simulation of a shell-and-tube latent heat thermal energy storage unit, Sol. Energy. 50 (1993) 357–367. https://doi.org/10.1016/0038-092X(93)90029-N.

[64] H. El Qarnia, Numerical analysis of a coupled solar collector latent heat storage unit using various phase change materials for heating the water, Energy Convers. Manag. 50 (2009) 247–254. https://doi.org/10.1016/j.enconman.2008.09.038.

[65] H.A. Adine, H. El Qarnia, Numerical analysis of the thermal behaviour of a shell-and-tube heat storage unit using phase change materials, Appl. Math. Model. 33 (2009) 2132–2144. https://doi.org/10.1016/j.apm.2008.05.016.

[66] M. Longeon, A. Soupart, J. Fourmigué, A. Bruch, P. Marty, Experimental and numerical study of annular PCM storage in the presence of natural convection, Appl. Energy. 112 (2013) 175–184. https://doi.org/10.1016/j.apenergy.2013.06.007.

[67] R.G. Kemink, E.M. Sparrow, Heat transfer coefficients for melting about a vertical cylinder with or without subcooling and for open or closed containment, Int. J. Heat Mass Transf. 24 (1981) 1699–1710. https://doi.org/10.1016/0017-9310(81)90078-8.

[68] B. Kalhori, S. Ramadhyani, Studies on heat transfer from a vertical cylinder, with or without fins, embedded in a solid phase change medium, J. Heat Transfer. 107 (1985) 44–51. https://doi.org/10.1115/1.3247400.

[69] P.R. Souza Mendes, A.C. Pinho Brasil, Heat transfer during melting around an isothermal vertical cylinder, J. Heat Transfer. 109 (1987) 961–964. https://doi.org/10.1115/1.3248210.

[70] M. Esen, A. Durmuş, A. Durmuş, Geometric design of solar-aided latent heat store depending on various parameters and phase change materials, Sol. Energy. 62 (1998) 19–28. https://doi.org/10.1016/S0038-092X(97)00104-7.

[71] M. Fang, G. Chen, Effects of different multiple PCMs on the performance of a latent thermal energy storage system, Appl. Therm. Eng. 27 (2007) 994–1000. https://doi.org/10.1016/j.applthermaleng.2006.08.001.

[72] S. Seddegh, X. Wang, A.D. Henderson, A comparative study of thermal behaviour of a horizontal and vertical shell-and-tube energy storage using phase change materials, Appl. Therm. Eng. 93 (2016) 348–358. https://doi.org/10.1016/j.applthermaleng.2015.09.107.

[73] S. Seddegh, X. Wang, A.D. Henderson, Numerical investigation of heat transfer mechanism in a vertical shell and tube latent heat energy storage system, Appl. Energy. 154 (2015) 698–706. https://doi.org/10.1016/j.applthermaleng.2015.05.067.

[74] X. Xiao, P. Zhang, Numerical and experimental study of heat transfer characteristics of a shell-tube latent heat storage system: Part I - Charging process, Energy. 79 (2015) 337–350. https://doi.org/10.1016/j.energy.2014.11.020.

[75] X. Xiao, P. Zhang, Numerical and experimental study of heat transfer characteristics of a shell-tube latent heat storage system: Part II - Discharging process, Energy. 80 (2015) 177–189. https://doi.org/10.1016/j.energy.2014.11.061.

[76] M. Akgün, O. Aydin, K. Kaygusuz, Experimental study on melting/solidification characteristics of a paraffin as PCM, Energy Convers. Manag. 48 (2007) 669–678. https://doi.org/10.1016/j.enconman.2006.05.014.

[77] F. Agyenim, P. Eames, M. Smyth, Experimental study on the melting and solidification behaviour of a medium temperature phase change storage material (Erythritol) system augmented with fins to power a LiBr/H2O absorption cooling

system, Renew. Energy. 36 (2011) 108–117. https://doi.org/10.1016/j.renene.2010.06.005.

[78] Y. Wang, L. Wang, N. Xie, X. Lin, H. Chen, Experimental study on the melting and solidification behavior of erythritol in a vertical shell-and-tube latent heat thermal storage unit, Int. J. Heat Mass Transf. 99 (2016) 770–781. https://doi.org/10.1016/j.ijheatmasstransfer.2016.03.125.

[79] Z. Fan, C.A. Infante Ferreira, A.H. Mosaffa, Numerical modelling of high temperature latent heat thermal storage for solar application combining with double-effect H2O/LiBr absorption refrigeration system, Sol. Energy. 110 (2014) 398–409. https://doi.org/10.1016/j.solener.2014.09.036.

[80] H. Pointner, A. de Gracia, J. Vogel, N.H.S. Tay, M. Liu, M. Johnson, L.F. Cabeza, Computational efficiency in numerical modeling of high temperature latent heat storage: Comparison of selected software tools based on experimental data, Appl. Energy. 161 (2016) 337–348. https://doi.org/10.1016/j.apenergy.2015.10.020.

[81] F. Fornarelli, S.M. Camporeale, B. Fortunato, M. Torresi, P. Oresta, L. Magliocchetti, A. Miliozzi, G. Santo, CFD analysis of melting process in a shell-and-tube latent heat storage for concentrated solar power plants, Appl. Energy. 164 (2016) 711–722. https://doi.org/10.1016/j.apenergy.2015.11.106.

[82] S. Riahi, W.Y. Saman, F. Bruno, M. Belusko, N.H.S. Tay, Impact of periodic flow reversal of heat transfer fluid on the melting and solidification processes in a latent heat shell and tube storage system, Appl. Energy. 191 (2017) 276–286. https://doi.org/10.1016/j.apenergy.2017.01.091.

[83] M.D. Muhammad, O. Badr, H. Yeung, CFD modeling of the charging and discharging of a shell-and-tube latent heat storage system for high-temperature applications, Numer. Heat Transf. Part A Appl. 68 (2015) 813–826. https://doi.org/10.1080/10407782.2015.1023094.

[84] S.S.M. Tehrani, System-Level Analysis of High-Temperature Thermal Energy Storage Systems for Solar Power Plants, The University of New South Wales, 2017. https://doi.org/10.26190/unsworks/20151.

[85] Y.B. Tao, V.P. Carey, Effects of PCM thermophysical properties on thermal storage performance of a shell-and-tube latent heat storage unit, Appl. Energy. 179 (2016) 203–210. https://doi.org/10.1016/j.apenergy.2016.06.140.

[86] Y.Q. Li, Y.L. He, H.J. Song, C. Xu, W.W. Wang, Numerical analysis and parameters optimization of shell-and-tube heat storage unit using three phase change materials, Renew. Energy. 59 (2013) 92–99. https://doi.org/10.1016/j.renene.2013.03.022.

[87] T. Pirasaci, D.Y. Goswami, Influence of design on performance of a latent heat storage system for a direct steam generation power plant, Appl. Energy. 162 (2016) 644–652. https://doi.org/10.1016/j.apenergy.2015.10.105.

[88] Y.B. Tao, Y.L. He, Z.G. Qu, Numerical study on performance of molten salt phase change thermal energy storage system with enhanced tubes, Sol. Energy. 86 (2012) 1155–1163. https://doi.org/10.1016/j.solener.2012.01.004.

[89] S.S.M. Tehrani, R.A. Taylor, Off-design simulation and performance of molten salt cavity receivers in solar tower plants under realistic operational modes and control

strategies, Appl. Energy. 179 (2016) 698–715. https://doi.org/10.1016/j.apenergy.2016.07.032.

[90] J.A. Hesketh, P.J. Walker, Effects of wetness in steam turbines, Proc. Inst. Mech. Eng. Part C J. Mech. Eng. Sci. 219 (2005) 1301–1314. https://doi.org/10.1243/095440605X32110.

[91] M. Sarvghad, S. Delkasar Maher, D. Collard, M. Tassan, G. Will, T.A. Steinberg, Materials compatibility for the next generation of concentrated solar power plants, Energy Storage Mater. 14 (2018) 179–198. https://doi.org/10.1016/j.ensm.2018.02.023.

[92] J.E. Rea, C.J. Oshman, A. Singh, J. Alleman, P.A. Parilla, C.L. Hardin, M.L. Olsen, N.P. Siegel, D.S. Ginley, E.S. Toberer, Experimental demonstration of a dispatchable latent heat storage system with aluminum-silicon as a phase change material, Appl. Energy. 230 (2018) 1218–1229. https://doi.org/10.1016/j.apenergy.2018.09.017.

[93] M. Yan, Z. Fan, Durability of materials in molten aluminum alloys, J. Mater. Sci. 36 (2001) 285–295. https://doi.org/10.1023/A:1004843621542.

[94] A. Dindi, N. Lopez Ferber, D. Gloss, E. Rilby, N. Calvet, Compatibility of an Aluminium-Silicon metal alloy-based phase change material with coated stainless-steel containers, J. Energy Storage. 32 (2020) 101961. https://doi.org/10.1016/j.est.2020.101961.

[95] M. Jonemann, Advanced Thermal Storage System with Novel Molten Salt, 2013. http://www.nrel.gov/docs/fy13osti/58595.pdf.

[96] L. Heller, Literature Review on Heat Transfer Fluids and Thermal Energy Storage Systems in CSP Plants, 2013. https://sterg.sun.ac.za/wp-content/uploads/2011/08/HTF_TESmed_Review_2013_05_311.pdf.

[97] K. Vignarooban, X. Xu, A. Arvay, K. Hsu, A.M. Kannan, Heat transfer fluids for concentrating solar power systems - A review, Appl. Energy. 146 (2015) 383–396. https://doi.org/10.1016/j.apenergy.2015.01.125.

[98] M. Liu, R. Jacob, M. Belusko, S. Riahi, F. Bruno, Techno-economic analysis on the design of sensible and latent heat thermal energy storage systems for concentrated solar power plants, Renew. Energy. 178 (2021) 443–455. https://doi.org/10.1016/j.renene.2021.06.069.

[99] S.S. M Tehrani, Y. Shoraka, K. Nithyanandam, R.A. Taylor, Cyclic performance of cascaded and multi-layered solid-PCM shell-and-tube thermal energy storage systems: A case study of the 19.9 MW e Gemasolar CSP plant, Appl. Energy. 228 (2018) 240–253. https://doi.org/10.1016/j.apenergy.2018.06.084.

[100] S.S. Mostafavi Tehrani, Y. Shoraka, K. Nithyanandam, R.A. Taylor, Shell-and-tube or packed bed thermal energy storage systems integrated with a concentrated solar power: A techno-economic comparison of sensible and latent heat systems, Appl. Energy. 238 (2019) 887–910. https://doi.org/10.1016/j.apenergy.2019.01.119.

[101] Y. Zhao, H.B. Liu, C.Y. Zhao, Experimental study on the cycling stability and corrosive property of Al-Si alloys as phase change materials in high-temperature heat storage, Sol. Energy Mater. Sol. Cells. 203 (2019) 110165. https://doi.org/10.1016/j.solmat.2019.110165.

[102] S. Arena, E. Casti, J. Gasia, L.F. Cabeza, G. Cau, Numerical analysis of a latent heat thermal energy storage system under partial load operating conditions, Renew. Energy. 128 (2018) 350–361. https://doi.org/10.1016/j.renene.2018.05.072.

[103] M. Liu, S. Riahi, R. Jacob, M. Belusko, F. Bruno, Design of sensible and latent heat thermal energy storage systems for concentrated solar power plants: Thermal performance analysis, Renew. Energy. 151 (2020) 1286–1297. https://doi.org/10.1016/j.renene.2019.11.115.

[104] C. Prakash, M. Samonds, A.K. Singhal, A fixed grid numerical methodology for phase change problems involving a moving heat source, Int. J. Heat Mass Transf. 30 (1987) 2690–2694. https://doi.org/10.1016/0017-9310(87)90152-9.

[105] S.S. Mostafavi Tehrani, G. Diarce, R.A. Taylor, The error of neglecting natural convection in high temperature vertical shell-and-tube latent heat thermal energy storage systems, Sol. Energy. 174 (2018) 489–501. https://doi.org/10.1016/j.solener.2018.09.048.

[106] V.R. Voller, C. Prakash, A Fixed grid numerical modelling methodology for convection diffusion mushy region phase change problems, Int. Jounal Heat Mass Transf. 30 (1978) 1709–1719. https://doi.org/https://doi.org/10.1016/0017-9310(87)90317-6.

[107] V.R. Voller, C.R. Swaminathan, General source-based method for solidification phase change, Numer. Heat Transf. Part B. 19 (1991) 175–189. https://doi.org/https://doi.org/10.1080/10407799108944962.

[108] S.S. Mostafavi Tehrani, Y. Shoraka, K. Nithyanandam, R.A. Taylor, Shell-and-tube or packed bed thermal energy storage systems integrated with a concentrated solar power: A techno-economic comparison of sensible and latent heat systems, Appl. Energy. 238 (2019) 887–910. https://doi.org/10.1016/j.apenergy.2019.01.119.

[109] G.E.P. Box, J.S. Hunter, W.G. Hunter, Statistics for Experimenters, Second edi, Wiley, 2005. https://doi.org/10.1080/00401706.1979.10489788.

[110] R.H. Myers, D.C. Montgomery, C.M. Anderson-Cook, Response Surface Methodology: Process and Product Optimization Using Designed Experiments, Fourth edi, Wiley, 2016. https://www.wiley.com/en-us/Response+Surface+Methodology:+Process+and+Product+Optimization+Using+Designed+Experiments,+4th+Edition-p-9781118916018.

[111] A.I. Khuri, J.A. Cornell, Response Surfaces: Designs and Analyses, Second edi, CRC Press, 2019. https://doi.org/https://doi.org/10.1201/9780203740774.

[112] S. Karimifard, M.R. Alavi Moghaddam, Application of response surface methodology in physicochemical removal of dyes from wastewater: A critical review, Sci. Total Environ. 640–641 (2018) 772–797. https://doi.org/10.1016/j.scitotenv.2018.05.355.

[113] F. Dominio, Techno-Economic Analysis of Hybrid PV-CSP Power Plants, KTH Royal Institute of Technology, 2014. https://upcommons.upc.edu/bitstream/handle/2117/82170/Federico Dominio - Final report.pdf.

[114] A. Green, C. Diep, R. Dunn, J. Dent, High Capacity Factor CSP-PV Hybrid Systems, Energy Procedia. 69 (2015) 2049–2059. https://doi.org/10.1016/j.egypro.2015.03.218.

[115] S. Pfenninger, P. Gauché, J. Lilliestam, K. Damerau, F. Wagner, A. Patt, Potential for concentrating solar power to provide baseload and dispatchable power, Nat. Clim. Chang. 4 (2014) 689–692. https://doi.org/10.1038/nclimate2276.

[116] S. Pfenninger, J. Keirstead, Comparing concentrating solar and nuclear power as baseload providers using the example of South Africa, Energy. 87 (2015) 303–314. https://doi.org/10.1016/j.energy.2015.04.077.

[117] A. Zurita, C. Mata-Torres, J.M. Cardemil, R. Guédez, R.A. Escobar, Multi-objective optimal design of solar power plants with storage systems according to dispatch strategy, Energy. 237 (2021). https://doi.org/10.1016/j.energy.2021.121627.

[118] D. Ziyati, A. Dollet, G. Flamant, Y. Volut, E. Guillot, A. Vossier, A multiphysics model of large-scale compact PV–CSP hybrid plants, Appl. Energy. 288 (2021) 116644. https://doi.org/10.1016/j.apenergy.2021.116644.

[119] B. Basu, Toughening of yttria-stabilised tetragonal zirconia ceramics, Int. Mater. Rev. 50 (2005) 239–256. https://doi.org/10.1179/174328005X41113.

[120] A.I. Khuri, A general overview of response surface methodology, Biometrics Biostat. Int. J. 5 (2017) 87–93. https://doi.org/10.15406/bbij.2017.05.00133.

[121] B.E. Ankenman, Identifying rising ridge behavior in quadratic response surfaces, IIE Trans. 35 (2003) 493–502. https://doi.org/10.1080/07408170304425.

[122] F. Bruno, M. Belusko, N.H.S. Tay, Design of PCM Thermal Storage System using the Effectiveness-NTU Method, in: EuroSun 2010, 2010.

[123] A. Castell, M. Belusko, F. Bruno, L.F. Cabeza, Maximisation of heat transfer in a coil in tank PCM cold storage system, Appl. Energy. 88 (2011) 4120–4127. https://doi.org/10.1016/j.apenergy.2011.03.046.

[124] N.H.S. Tay, M. Belusko, F. Bruno, An effectiveness-NTU technique for characterising tube-in-tank phase change thermal energy storage systems, Appl. Energy. 91 (2012) 309–319. https://doi.org/10.1016/j.apenergy.2011.09.039.

[125] N.H.S. Tay, M. Belusko, F. Bruno, Experimental investigation of tubes in a phase change thermal energy storage system, Appl. Energy. 90 (2012) 288–297. https://doi.org/10.1016/j.apenergy.2011.05.026.

[126] N.H.S. Tay, F. Bruno, M. Belusko, Experimental validation of a CFD and an ε-NTU model for a large tube-in-tank PCM system, Int. J. Heat Mass Transf. 55 (2012) 5931–5940. https://doi.org/10.1016/j.ijheatmasstransfer.2012.06.004.

[127] M. Liu, N.H.S. Tay, M. Belusko, F. Bruno, Investigation of cascaded shell and tube latent heat storage systems for solar tower power plants, Energy Procedia. 69 (2015) 913–924. https://doi.org/10.1016/j.egypro.2015.03.175.

[128] M.M. Kenisarin, High-temperature phase change materials for thermal energy storage, Renew. Sustain. Energy Rev. 14 (2010) 955–970. https://doi.org/10.1016/j.rser.2009.11.011.

List of publications and awards

International Journals (Published)

1. **Vivek Tiwari**, Aakash C. Rai, P. Srinivasan, Parametric analysis and optimization of a latent heat thermal energy storage system for concentrated solar power plants under realistic operating conditions, Renewable Energy, Volume 174, 2021, Pages 305-319, ISSN 0960-1481, https://doi.org/10.1016/j.renene.2021.04.073. **(SCI-E, Impact Factor: 8.634, H-index: 210)**
2. **Vivek Tiwari**, P. Srinivasan, SWOT analyses of high-temperature phase change materials for thermal energy storage, Materials Today: Proceedings, Volume 28, Part 2, 2020, Pages 949-954, ISSN 2214-7853, https://doi.org/10.1016/j.matpr.2019.12.331. **(SCOPUS, H-index: 56).**

Papers (Communicated/Accepted)

1. **Vivek Tiwari**, Aakash C. Rai, and Srinivasan Periaswamy. Multi-objective optimization of a latent heat thermal energy storage (TES) system for Concentrated solar power plants using response surface methodology (under preparation)
2. **Vivek Tiwari**, and Srinivasan Periaswamy. Corrosion control of Aluminum silicon eutectic alloy Thermal Energy Storage using the ceramic coating. UNDER REVIEW in Journal of Energy Storage (Submitted in November 2022)

Awards

1. **Infrastructure access travel grant** - Improved Design Methodology for High-Temperature Thermal Energy Storage Systems for Concentrated Solar Power Plants (proposal for infrastructure access under European Union's Horizon 2020 research and innovation programme under grant agreement No 823802)**.**
2. Attended the first Summer School and Doctoral Colloquium of Solar Facilities for the European Research Area-Third phase (SFERA-III). It was held in Odeillo (France) in September 2019 at the PROMES-CNRS laboratory.

List of conferences and courses attended

International Conferences

1. **Vivek Tiwari**, and P. Srinivasan (2022). Investigations to Identify Suitable Structural Material Compatible with AlSi12 for Phase Change Applications. Recent Advances in Materials, Manufacturing and Thermal Engineering (RAMMTE-2022), Delhi Technical University (DTU), Delhi, India. (Oral presentation)
2. **Vivek Tiwari**, and P. Srinivasan (2019). SWOT analyses of high-temperature phase change materials for thermal energy storage. *2nd International Conference on Recent Advances in Materials & Manufacturing Technologies*, BITS Pilani (Dubai campus), Dubai, UAE. (Oral presentation)
3. Karan Ghule, **Vivek Tiwari**, and P. Srinivasan (2019). Design and CFD Analysis of Al-Si12 Alloy Based Latent Heat Storage System for Direct Steam Generation Solar Power Plants. 3rd International ISHMT-ASTFE Heat and Mass Transfer Conference, IIT Roorkee, Roorkee, India. (Oral presentation)
4. **Vivek Tiwari**, Kedar H. Patil, and P. Srinivasan, Simulation and experimental investigation of melting process in spherical PCM capsules used for low-temperature thermal energy storage systems, 2nd International Conference on Sustainable Energy and Environmental Challenges (SEEC-2018) 31st December 2018.
5. Kedar H Patil, **Vivek Tiwari**, P. Srinivasan, Investigations on different types of fin profiles by simulation to improve the performance of PCM materials based thermal energy storage system, 2nd International Conference on Sustainable Energy and Environmental Challenges (SEEC-2018) 31st December 2018.

Courses

1. Summer school at CNRS-PROMES laboratory, Odeillo, France, 1st Summer School and Doctoral Colloquium of Solar Facilities for the European Research Area-III (under SFERA-III project) (Sept 2019)
2. Course on Recent advances in PCM-based cooling technology at Indian Institute of Technology, Bhubaneswar, India (Dec 2017)
3. Course on Second law analysis of thermal energy storage systems at Indian Institute of Technology, Indore, India (July 2017)

Brief biography of the supervisors and candidate

About the Supervisor (Prof. Srinivasan Periaswamy)

Prof. Srinivasan Periaswamy is B.E. in Mechanical Engineering from Regional Engineering College (NIT), Srinagar, M.E. (Industrial Metallurgy), and Ph.D. (Production Engineering) from Regional Engineering College (NIT), Tiruchirappalli. He has more than 30 years of teaching and research experience. He joined BITS Pilani as a faculty in 2006. Before joining BITS Pilani, he served as faculty at SASTRA Deemed University, Thanjavur, and AA College of Engineering & Technology, Tiruchirappalli.

His research interest includes solar thermal, thermal energy storage, thermal engineering, renewable energy, energy economics, and energy efficiency. He has more than 30 publications in international journals and international conferences. He is guiding four Ph.D. students and has guided one Ph.D., over 50 PG, and UG thesis.

His web page is *https://www.bits-pilani.ac.in/pilani/psrinivasan/profile*

About the Co-supervisor (Dr. Aakash Chand Rai)

Dr. Aakash Chand Rai is B.Tech. in Mechanical Engineering from the Indian Institute of Technology (IIT) Kharagpur, India, and Mechanical Engineering from Purdue University, USA. He has more than 14 years of teaching and research experience. He joined IIT Kanpur (IITK) as a faculty in 2022. Before joining IITK, he served as faculty in BITS Pilani and research staff at the University of Surrey in UK, General Electric (GE), and DRDO in India.

His research interest includes energy-efficient buildings, the impact of climate change on the heating and cooling of buildings, indoor air quality, airborne infection transmission, and air pollution. He has more than 19 publications in international journals and international conferences. He is guiding four Ph.D. students, over 4 PG, and UG theses.

His web page is *https://home.iitk.ac.in/~aakashrai/*

About the candidate (Vivek Tiwari)

Vivek Tiwari graduated with Bachelor of Engineering (B.E.) in Mechanical Engineering from Nagpur University, Nagpur, in 2013 and post-graduated with Masters in Technology (M.Tech.) in Energy Systems and Technology (Focused on Solar Energy) from Pandit Deendayal Petroleum University, Gandhinagar, in 2015. He joined the Department of Mechanical Engineering at BITS Pilani, Pilani campus, as a Ph.D. research scholar in January 2017. During his doctoral research, he has various research papers in international journals of repute and many technical papers at international conferences.

His research includes concentrated solar power, long-duration energy storage, thermal energy storage, phase change material, and district heating. During his Ph.D., he received an institute doctoral research fellowship (2017-2022) from BITS Pilani and an infrastructure access travel grant under the European Union's Horizon 2020 research and innovation program to visit the National Laboratory of Energy and Geology (LNEG), Lisbon, Portugal from Oct-Nov 2022.

His web page is *https://www.bits-pilani.ac.in/pilani/p2016414/profile*